Un amplificateur basé sur le tunneling inélastique de paires de Cooper

Salha Jebari

Communauté
UNIVERSITÉ Grenoble Alpes

THÈSE

Pour obtenir le grade de

DOCTEUR DE la Communauté UNIVERSITÉ GRENOBLE ALPES

Spécialité : **Physique de la Matière Condensée et du Rayonnement**

Arrêté ministériel : 7 Août 2006

Présentée par

Salha JEBARI

Thèse dirigée par **Marc SANQUER**
et codirigée par **Max HOFHEINZ**

préparée au sein **du laboratoire de transport électronique quantique et supraconductivité,**
du service de photonique electronique et ingénierie quantiques,
de l'institut nanosciences et cryogénie,
du CEA Grenoble
et de **l'école doctorale de physique de Grenoble**

The Inelastic Cooper pair Tunneling Amplifier (ICTA)

Thèse soutenue publiquement le **26 juin 2017**,
devant le jury composé de :

Pr. Michel DEVORET
Yale University, Rapporteur
Pr. Benjamin HUARD
ENS Lyon, Rapporteur
Dr. Fabien PORTIER
CEA Saclay, Examinateur
Pr. Wiebke GUICHARD
Institut Néel/CNRS, Président

Abstract

The Inelastic Cooper pair Tunneling Amplifier (ICTA)

Josephson parametric amplifiers (JPAs) have proven to be an indispensable tool for a wide range of experiments on quantum devices in the microwave frequency regime, because they provide the lowest possible noise. However, JPAs remain much more difficult to use and optimize than conventional microwave amplifiers. Recent experiments with superconducting circuits consisting of a DC voltage-biased Josephson junction in series with a resonator, have shown that a tunneling Cooper pair can emit one or several photons with a total energy of 2e times the applied voltage. In this thesis we show that such circuits can be used to implement a new type of phase preserving microwave amplifier, which we call Inelastic Cooper pair Tunneling Amplifier (**ICTA**). It is powered by a simple DC bias and offers near quantum-limited noise performance.

First of all we present a brief and simple picture of the basic ICTA physics. In analogy with the quantum theory of JPAs, we derive the performances of this amplifier such as gain, bandwidth and noise. Then, we present the first experimental proof of the ICTA, showing that amplification close to the quantum limit is possible without microwave drive in an extremely simple setup. These measurements were made on a first generation of samples based on aluminium junctions. According to our theoretical and experimental results, we designed microwave circuits presenting specific frequency-dependent impedances to the junction in order to optimize the performances of our amplifier. This second generation of ICTA samples was fabricated from niobium nitride and provide a significantly lower noise and a higher gain.

We expect that once fully optimized, such an amplifier, powered by simple DC voltages could then make measuring microwave signals at the single photon level much easier and allow deploying many amplifiers on a chip. It could therefore be an important ingredient for qubit readout in large-scale quantum processors.

Résumé

Un amplificateur basé sur le tunneling inélastique de paires de Cooper

Les amplificateurs paramétriques Josephson (JPAs) se sont révélés être un outil indispensable pour l'étude expérimentale de dispositifs quantiques dans le régime micro-onde car ils rajoutent uniquement le minimum de bruit imposé par la mécanique quantique. Cependant, ces amplificateurs sont beaucoup plus difficiles à utiliser et optimiser que leurs homologues classiques. Récemment, plusieurs expériences réalisées avec des circuits supraconducteurs, composés d'une jonction Josephson polarisée en tension en série avec un résonateur micro-onde, ont montré qu'une paire de Cooper peut traverser la barrière de la jonction par effet tunnel en émettant un ou plusieurs photons avec une énergie totale de 2e fois la tension appliquée. Dans cette thèse, nous montrerons qu'un tel circuit permet de réaliser un amplificateur micro-onde préservant la phase que nous appelons « Amplificateur basé sur le tunneling inélastique de paires de Cooper » (ICTA pour "Inelastic Cooper pair Tunneling Amplifier" en anglais). Il est alimenté par une tension continue et peut fonctionner avec un bruit très proche de la limite quantique.

Nous commencerons par présenter le principe du fonctionnement de l'ICTA. Par analogie avec la théorie quantique des JPAs, nous dérivons les performances de cet amplificateur comme le gain, la bande passante et le bruit. Ensuite, nous présenterons la première preuve expérimentale d'une amplification proche de la limite quantique sans utilisation d'une pompe micro-onde externe, mais simplement d'une tension continue dans une configuration extrêmement simple. Ces mesures ont été faites sur des échantillons avec des jonctions en aluminium, dénommés ICTA de première génération. Selon nos résultats théoriques et expérimentaux, nous avons conçu des circuits micro-ondes présentant des impédances en fonction de la fréquence spécifiques à la jonction afin d'optimiser les performances de notre amplificateur. Ces échantillons, dénommés ICTA de seconde génération, ont été fabriqués avec du nitrure de niobium. Nous avons observé une amélioration significative du gain et du bruit.

Un tel amplificateur, alimenté par une simple tension continue, pourrait rendre la mesure de signaux micro-ondes au niveau du photon unique beaucoup plus faciles et permettre d'intégrer plusieurs amplificateurs sur une seule puce. Il pourrait donc être un élément important pour la lecture de qubit dans les processeurs quantiques à grande échelle.

Introduction

In this thesis, I present the first results of a low noise, phase preserving microwave amplifier based on a voltage-biased Josephson junction which we call the ***Inelastic Cooper pair Tunneling Amplifier (ICTA)***. The goal of this work is to prove that amplification close to the quantum limit is also possible in such an extremely simple DC-powered setup.

Scientific context and motivation

In the concept of the rapid development of superconducting qubits [1–6] have been developed for their readout near quantum limited microwave amplifiers. They are useful for many other application such as the low-noise readout of other solid state qubits [7] and nanoelectromechanical systems [8]. The quantum limit on the noise [9] of a linear phase preserving amplifier can be derived straightforwardly from first principles [10]. This derivation shows that the incoming signal necessarily has to be coupled to at least one complementary mode, called *idler*, and that the photon noise of this mode is added to the amplified signal. In the ideal case, where the idler mode is in its quantum ground state, the added input noise power spectral density is half a photon. This limit is only reached by parametric amplifiers, which exploit the nonlinearities provided by the inductance of the Josephson junction, acting as a non-dissipative element at low temperature below the critical current I_c. The Josephson junction in this case is used to couple a microwave pump tone to the signal mode, giving rise to a perfectly well defined idler mode at the frequency f_i, the difference of (a multiple of) the pump frequency and the signal frequency. These Josephson parametric amplifiers approach quantum-limited noise performance [11–15] but require strong external microwave pump tones which make them more difficult to use than DC powered amplifiers. Moreover, the pump tone can affect the device under test and requires extensive and expensive room-temperature equipment. In DC powered amplifiers, on the other hand, this idler mode is usually not well identified and difficult to engineer properly. For example, in HEMT amplifiers, it corresponds to electronic degrees of freedom inside the transistor which are kept out-of-equilibrium by the DC bias. In DC-powered superconductor-based amplifiers such as the Superconducting Low-indUctance Galvanometer (*SLUG*) [16, 17] or Single Junction Amplifier (*SJA*) [18], the idler can be seen as one of the modes of the dissipative shunt of the junction which also dissipates most of the DC power and gets hot.

In this thesis I address this problem: ***How can we create a simple DC-powered amplifier working at the quantum limit?***

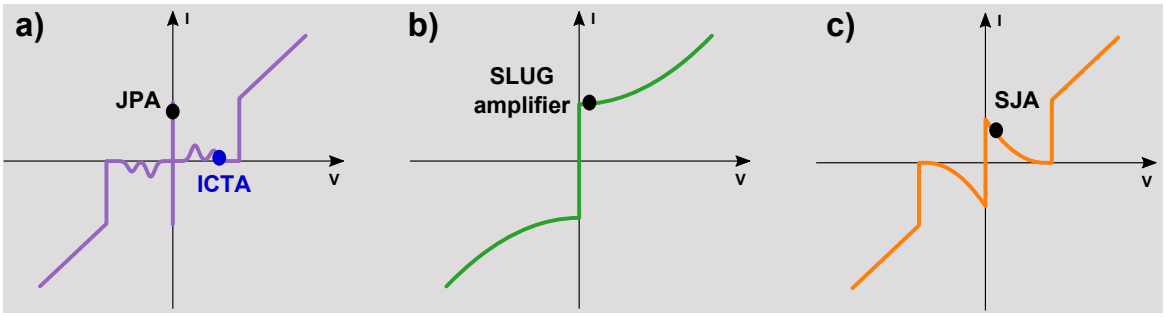

Figure 1 **Operation modes of recent DC Josephson amplifiers and JPAs: a)** I-V characteristics of an unshunted Josephson junction. **b, c)** I-V characteristics of shunted Josephson junction. The black dots indicate the working regime of the SLUG amplifier, SJA and JPAs. The blue dots indicates the working regime of the ICTA.

DC biased Josephson junction amplifier

With the rapid progress of superconducting quantum computers [19–21], ever more, complex quantum circuits with a large number of superconducting qubits are built. Low noise amplifiers could be useful for high-fidelity quantum-state qubit readout and a DC-powered amplifier could significantly simplify the architecture and operations. Here, we discuss the performances of two recent DC biased Josephson junction amplifiers, the *SLUG* amplifier [16, 17] and the *SJA* [18]. Then, we compare them with our approach.

The *SLUG* amplifier [16, 17], developed in R.McDermott's group at Madison, is a phase-insensitive linear amplifier based on a Superconducting Low-inductance Undulatory galvanometer. It consists of a shunted DC Superconducting QUantum Interference Device (SQUID) and relies on a separate inductor to transform the input signal to a magnetic flux. The highest measured gain is around 25 dB for several MHz of bandwidth. The *SJA*, realized in Pertti Hakonen's group at Aalto, is based on the negative differential resistance of a selectively damped Josephson junction. This amplifier consists of a Josephson junction shunted by a resistor in series with a bandstop filter whose centre frequency is at the signal frequency [22, 23]. The maximum measured gain of the *SJA* is approximately 28.3 dB over few MHz. The -1 dB compression point is -134 dBm. Figure 1 illustrates the I-V curve of the shunted and unshunted junctions and we indicate the working regime of both SLUG amplifier, SJA and JPAs

For the ICTA, we use an unshunted Josephson junction; below the superconducting gap, such junction itself is non dissipative. In *SLUG* amplifier and *SJA* cases, the notion of idler

mode is absent. In our work, we define the complementary signal mode by exploiting the dynamic Coulomb blockade physics.

Dynamic Coulomb Blockade (DCB)

Repulsion of charges in a small island contacted by two tunnel junctions leads to a phenomena called *static Coulomb blockade*. This effect is used to control precisely the number of electrons stored in the island. In fact, the static Coulomb blockade takes place when the charging energy of the island is non-negligible compared to the thermal energy and the energy qV of a particle with a charge q where V is the voltage difference between the island and the neighbouring electrode. Coulomb blockade (CB) has been first observed in 1962s by C. A. Neugebauer and M. B. Webb [24] on a planar array of many small discrete islands made from a thin metallic film. Research in CB progressed in the 1980s by K. Likharev using small tunnel junctions[25]. A charge carrier, traversing a voltage biased tunnel junction, dissipates its energy qV_n by exciting n modes of the electromagnetic environment seen by the junction. However, this excitation of the mode with a resonance frequency ω_0 takes place only if $qV_n \geq \hbar\omega_0$ because of the quantization of the electromagnetic environment. If the voltage bias is reduced to validate this condition, we observe an effective drop in the differential conductance dI/dV of the junction, called *Dynamic Coulomb Blockade* (DCB). The theoretical framework of this phenomenon is well understood by the P(E) theory [26–29]. The so-called P(E) theory has been developed to describe the behaviour of a tunnel junction coupled to a linear electromagnetic environment. It is only valid in a regime where the electrons tunnel independently and the electromagnetic environment is in thermal equilibrium.

Inelastic Cooper pair tunneling

So far, we have considered CB in normal tunnel junctions. Here we deal with the case of a superconducting tunnel junction where the dynamic Coulomb blockade effects are quite different[30]: for $V < 2\Delta/e$, the quasi-particles can't tunnel from one side to the other at the junction because there are no free states. So below the gap,the only charge carriers that have to be considered are Cooper Pairs (CP). For a voltage bias below the gap, a CP can tunnel by dissipating its surplus energy $2eV$ by exciting the modes of the electromagnetic environment (see figure (3)). In general, this environment can be modelled by a complex impedance $Z(\omega)$, which takes into account all linear electrical components of the circuit in which the junction is embedded. It describes the linear voltage response in the circuit to a current fluctuation at the junction as a function of the frequency ω [31]. In 1996, T.Holst et al [30] chose a

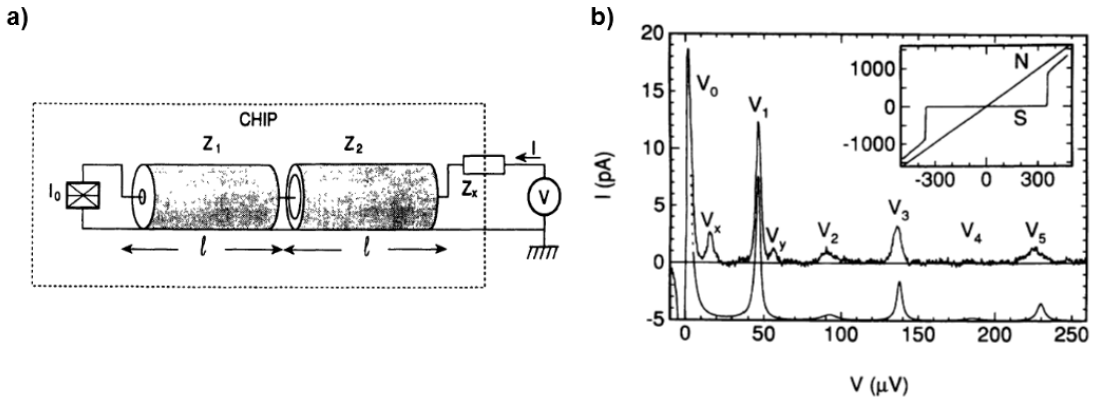

Figure 2 **The effect of Coulomb blockade in a Josephson junction :** The data are taken from [30]. I(V) curve of a Josephson junction coupled to a microwave resonator. The smooth continuous line is a theoretical curve which is obtained using the P(E) theory.

particular form of environment made from microwave resonators as shown in figure (2.a). The measurement result is presented in figure (2.b) where they observed a series of peaks in the I(V) curve under the superconducting gap. These peaks correspond to the conversion of the energy of the tunneling Cooper pair to a photon emitted in the resonator. A simple environment can be modelled by a LC resonator with a resonance frequency ω_0, as seen in figure (3). In this case the Hamiltonian of the system can be written as:

$$H = \hbar\omega_0(a^\dagger a + \frac{1}{2}) - \frac{E_J}{2}(e^{i\phi} + e^{-i\phi}) \tag{1}$$

Where ϕ is the phase. It can be written as function of the voltage V and time t as $\phi = 2eV/t$. The first term (blue) corresponds to the LC resonator Hamiltonian. a and $a^\dagger$ are respectively the annihilation and the creation quantum operators. The second term corresponds to the Josephson Hamiltonian. E_J is the Josephson energy. $e^{-i\phi}$ describes the phase acquired by tunnelling of the a Cooper pair from the right side of the junction to the left one. $e^{i\phi}$ describes the opposite case. The first two emission peaks occur at the voltage fulfilling the following conditions: when $\mathbf{2}eV = \hbar\omega_0$, the energy of tunneling CP is converted to one photon at ω_0, giving the one-photon process at ω_0. When $\mathbf{2}eV = \mathbf{2}\hbar\omega_0$, the energy of tunneling CP is converted to two photons at ω_0, giving the two-photon process at ω_0.

Higher photon numbers and combined processes between the resonances of the environment are also possible but are exponentially suppressed according to their order.

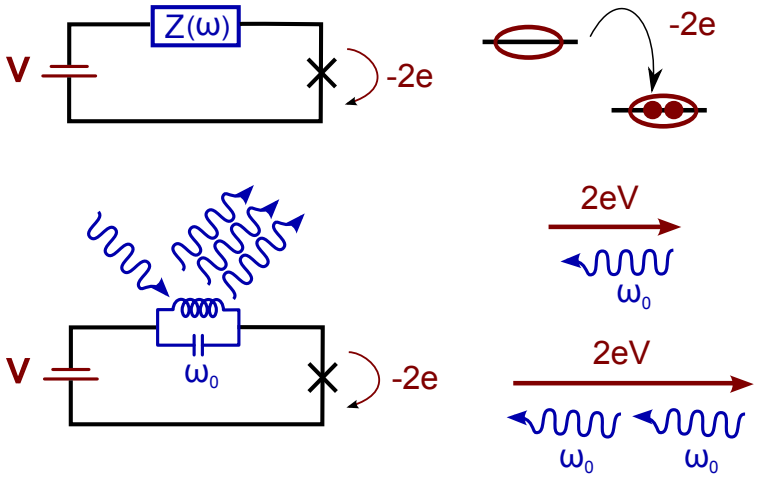

Figure 3 **Modelling of a linear electromagnetic environment:** A linear electromagnetic environment is characterised by its frequency-dependent impedance. A simple example of this environment consists of a single LC resonator with resonance frequency ω_0. $2\text{eV} = \hbar\omega_0$ results to emission of one photon at ω_0 per tunneling Cooper pair. $2\text{eV} = 2\hbar\omega_0$ results to simultaneous emission of two photons at ω_0 per tunneling Cooper pair.

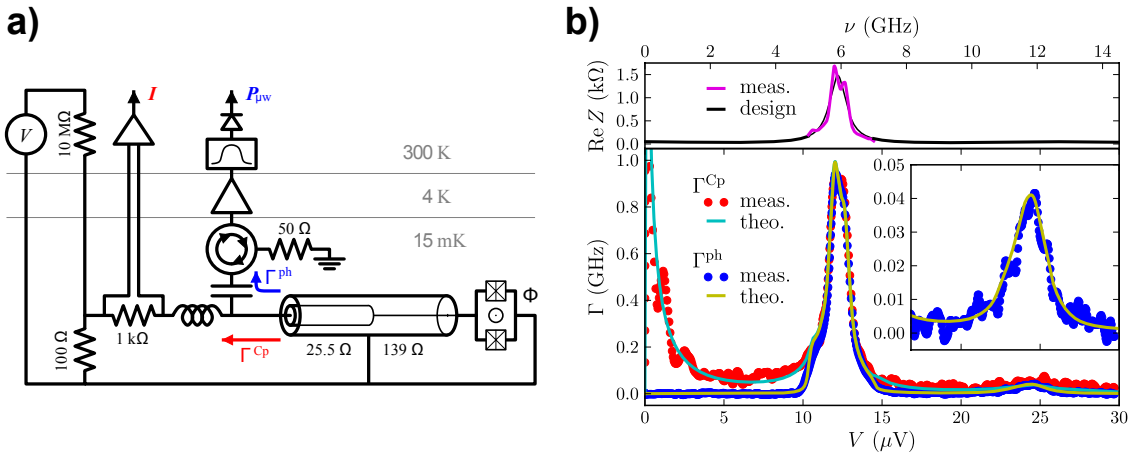

Figure 4 **Dynamic Coulomb blockade for a Josephson junction coupled to a resonator:** (figures from [31]). **a)** Experimental setup of Hofheinz et al. to measure simultaneously the mean Cooper pair rate $I = 2e\Gamma_{cp}$, I is the current, and the mean photon rate $P = hf\Gamma_{ph}$, P is the microwave power. **b)** Results from [31], the impedance seen by the Josephson junction presented in the top panel. In the bottom panel, Γ_{cp} and Γ_{ph} are plotted. There are current peaks and microwaves peaks for voltages such that V is a multiple of $\hbar\omega_0/2e = 12\,\mu\text{V}$ corresponding to one photon process and $2\hbar\omega_0/2e = 24\,\mu\text{V}$ corresponding to the two photon emission process.

The photonic side of inelastic Cooper pair tunnelling

A new study of this phenomenon has been made by Hofheinz *et al* in 2011, with a focus on the photonic side of inelastic Cooper pair tunnelling [31]. We consider a DC voltage biased Josephson junction in series with an electromagnetic environment. As explained previously, below the superconducting gap, the energy of a tunnelling Cooper pair $2eV$ can be transformed into n photons with frequencies corresponding to the resonance frequency ω_0 of the impedance seen by the Josephson junction such as $2eV{=}n\hbar\omega$. The strength of the coupling to mode at ω_0 increases with its characteristic impedance [29]. The observation of the photons emitted into these resonators requires cryogenic microwave equipment which was not available at the time of Holst experiment and it was performed only recently [31]. The sample used in this work consists of a small superconducting quantum interference device (SQUID) acting as a magnetic flux-tunable Josephson junction with a maximum critical current I_c = 17.5 nA. It is connected to a 50 Ω port via a quarter-wave transformer yielding peaks in the impedance seen by the junction at f_n = (2n+1).6 GHz with widths of approximately 500 MHz. The experimental setup is shown in figure (4.a). The device is cooled down to 12 mK. A bias-Tee is used to separate the high-frequency and low-frequency components of the current. The DC current path is indicated by red arrows while the microwave photons measurement path is indicated by blue arrows. The measurement results are shown in figure (4.b): the measured rate of the Cooper pair transfer rate across the SQUID $\Gamma_{cp} = \dfrac{I}{2e}$ and the measured rate of the photon emission into the fundamental mode of the resonator $\Gamma_{ph} = \dfrac{P}{\hbar\omega_0}$ as a function of the bias voltage. Both rates display a peak at the voltage $V = \dfrac{\hbar\omega}{2e} = 12\ \mu$V, where the energy of a tunnelling Cooper pair corresponds to the energy of one photon at frequency $\omega_0 = 6$ GHz. If the voltage is increased to have 24 μV i.e. when the energy of a tunnelling Cooper pair corresponds to the energy of two photons at frequency $\omega_0 = 6$ GHz, we observe a second peak corresponding to two-photon process.

Challenges and goal

In this work we investigate whether the physics of DCB is interesting for quantum optics with microwave photons. In particular, we focus on the last case where the energy of a tunnelling Cooper pair corresponds to the energy of two photons: $2eV = 2\hbar\omega_0$. This condition looks like the resonance condition of a degenerate parametric amplifier; when the energy of the pump is converted to the energy of two signal photons $\hbar\omega_p = 2\hbar\omega_s$. Here, we investigate what happenes when we send an RF signal to a similar circuit at ω_0. Is it possible

to see amplification?

As we will see, this is the case and the main goal of this thesis is to investigate if amplification at the quantum limit can be achieved by this DC powered Josephson amplifier. Consequently, we develop a theory explain the working principle of this amplifier and its performance. Then, by designing an appropriate linear matching circuit, characterized by its impedance Z(f) as seen by the Josephson junction we want to optimize it. Such an amplifier, powered by simple DC voltages could make measuring microwave signals at the single photon level much easier. Given its simplicity, many amplifiers ca be deployed on the same chip. It could therefore be an important ingredient for qubit readout in large-scale quantum processors. These samples are fabricated with niobium nitride (NbN) superconductor, which could allow operation at higher temperatures and frequencies.
This thesis is organised as follows:

Thesis overview

The thesis begins with theoretical introduction of the ICTA in chapter (1), giving some basic ideas on parametric amplification and noise. Then we study the ICTA Hamiltonian and its performance. In the second chapter, we present the experimental setup used in this work to examine ICTA samples. The rest of the thesis can be organised in two part: in the first part (chapter (3)), we present microwave reflection measurements on the device on aluminium Josephson junctions already used for the measurement in figure (4) [31]. In the second part (chapter (4), (5) and (6)) we present the design, fabrication and experimental results of samples based on niobium nitride Josephson junctions.

Chapter 1: Amplification based on inelastic Cooper pair tunneling

In this chapter, we present the physics of the Josephson parametric amplifier (JPA) and we discuss the origin of the quantum limit given by Caves's theorem [10] for both phase preserving and phase sensitive amplifiers. We also give some examples of recent works regarding the use of Josephson junctions and superconducting films with high kinetic inductance for parametric amplification. By making the link between the physics of JPAs and the DCB physics presented in this introduction, we introduce the operating principles of the ICTA. We describe quantum and semi-classic theoretical models of our amplifier. We finish this chapter by discussing the ICTA implementation in relation to the gain, bandwidth, noise properties, dynamic range and saturation.

Chapter 2: Experimental setup

In the second chapter, we discuss the wiring diagram of the setup in our dilution refrigerator used to measure the power spectral density and the microwave response of our samples. We finish by giving details on the different calibration methods used in this work with a special focus on noise calibration.

Chapter 3: First generation of the ICTA

In this first experimental chapter, we present the first generation of the ICTA, based on aluminium junctions [32]. We start by describing the measured sample. Then we discuss its performances such as the gain, noise and dynamic range. Thereafter, a comparison between experimental and theoretical results is shown. We finish by giving a summary of the shortcoming of this sample and then the aspect that we try to optimize for the new samples based on niobium nitride.

Chapter 4: Design

In this part, according to both theoretical and experimental results, we propose a new design and implementation of amplifiers based on niobium nitride. These devices are designed to optimize different proprieties of our amplifier. For that, we start by focusing on the two main elements of our circuit: the superconducting quantum interface device (SQUID) and the coplanar wave-guides (CPW). We will show how the SQUID is used as a flux tunable Josephson junction and we also treat very general aspects of the quarter wave and the half wave resonators. In the last part of this chapter, we present the designs of two main kinds of samples: the reflection amplifier and the transmission amplifier [33].

Chapter 5: Fabrication

In this chapter, we explain the fabrication process of the SQUID and the CPWs. We give details on the characterization of the obtained Josephson junctions and resonators. We finish by describing experiments performed at 300K and 4K in order to characterize these samples and to select the best candidate for measurements at very low temperature.

Chapter 6: Second generation of the ICTA

In this chapter, we focus on two samples and discuss how we can increase the gain and reduce the noise of our amplifier. Complete treatment is shown for both samples: the power spectral density measurement, flux modulation measurement, ICTA gain, noise and -1dB

compression point measurement. We also discuss briefly the results obtained from the other samples presented in chapter (4).

Conclusion and outlooks

Here, we recall the results obtained in this work. We discuss how the ICTA can be useful in our group or other projects. Finally, we conclude this thesis by giving some suggestions for new samples and for the direction of future works.

Summary of key results

Here, we summarize the main results obtained during this work:

- **Theoretical results:**
  - First demonstration of parametric amplification and conversion by exploiting the inelastic Cooper pair tunneling processes through a small DC voltage-biased Josephson junction.
  - Development of the ICTA Hamiltonian
  - Derivation the ICTA gain and bandwidth as a function of the Josephson junction energy.
  - Calculation of the DC current through the Josephson junction as a function of Bessel functions.
  - Calculation of the admittance from the P(E) theory.
- **Experimental results:**
  - Measurement of amplification as well as the first down-conversion terms.
  - Measurement of the non-linearities terms at high signal power.
  - Clear observation of parametric oscillation.
  - Measurement of the quartet, sextet and octet processes.
  - Optimization of the ICTA gain to more than 20 dB by increasing the Josephson junction energy.
  - Optimization of the ICTA noise to less than 0.4 photon by suppressing the down conversion terms @ 10 dB of gain.
  - Measurement of -1 dB compression point of -118 dBm for 21 dB of gain.
  - First proof of directionality of a transmission-ICTA.

Contents

Chapter 1

Amplification based on inelastic Cooper pair tunneling

The success of solid state quantum architectures such as circuit QED[34–36, 6] is based on the possibility to amplify microwave signals at the single photon level with minimal noise. This minimal noise is set by quantum mechanics and amounts to half a photon if the signal is amplified irrespective of its phase [10]. To date, this limit has been reached only by parametric amplifiers (PA) based on non-linearities in superconductors such as Josephson junctions [37, 12] or kinetic inductances [38] which are driven by a strong microwave pump tone. However, these amplifiers remain difficult to use because of the external microwave pump tone, a low bandwidth or a high complexity due to a large number of Josephson junctions. Simple-DC powered microwave amplifiers have failed so far to approach the quantum limit. Here, we describe a novel scheme for low-noise phase preserving parametric amplification at microwave frequencies based on a DC voltage biased Josephson junction which we call Inelastic Cooper pair Tunneling Amplifier (ICTA) [32].

The aim of this chapter is to present a brief and simple picture of the basic ICTA operating principles required to understand the results of this thesis. First, we want to address the question of what the ICTA is and how it works. Secondly, in analogy with the quantum theory of PAs [12], we calculate the full scattering matrix of this amplifier. Then, the ICTA performances such as the gain, bandwidth, noise and dynamic range are discussed. By commenting on the validity of this theory, we then introduce a semi-classical theory based on the P(E) theory. With a complementary range of validity we show that the gain of our amplifier scales, simply, with the Josephson energy. This can offer a high dynamic range as well as a large bandwidth.

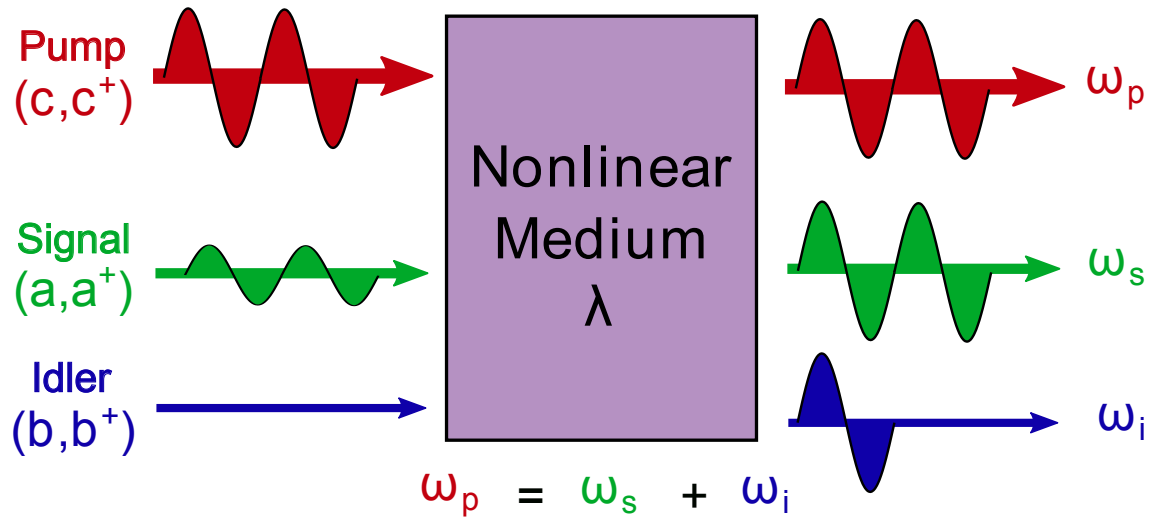

Figure 1.1 **Parametric amplification:** An input microwave wave, called pump, with frequency ω_p is converted into two output microwave signals at lower frequencies respectively ω_s and ω_i, called signal and idler, by means of non-linear interactions such as $\omega_p = \omega_s + \omega_i$. For optimal noise, the input idler mode must be in its quantum ground state.

1.1 Josephson parametric amplifiers (JPA)

This section introduces the basic operating principle of Josephson parametric amplifiers. Here, we delve into the theory of parametric amplification and noise. We show that the ultimate noise performance of an amplifier is limited by quantum mechanics. We deal this limitation for both, phase preserving and phase sensitive amplifiers. These topics are covered in great depth in a number of theses [39–41] and extended papers[11–15]. We use these references to give a brief overview of previous works on parametric amplification.

1.1.1 Parametric amplification

The working principle of parametric amplifiers, or paramps for short, is that by modulating, periodically, one parameter of the system it is possible to convert the energy of the modulation tone to a signal at a different frequency by generating another complementary signal called idler [39] (see figure (1.1)). In fact, the word parametric is used in quantum optics for phenomenon in which the reactive index of a non-linear medium is modulated by applying a pump tone. This modulation is employed for mixing different frequency components of light in form of photons detuned from the frequency of the pump [42–44]. An equivalent device can be realized in an electrical circuit at microwave frequencies by modulating an effective impedance. This is achieved by varying the parameters of either, a

capacitive or an inductive element in time.

In a general parametric process, an input wave, called pump, with frequency ω_p is converted into two output signals at lower frequencies respectively ω_s and ω_i called *signal* and *idler* by means of non-linear interaction (see figure (1.1)). This multiple-wave mixing effect can be classified depending on the type of amplifiers according to the relationship given by:

- **Non degenerate amplifier:** $\omega_p = \omega_s + \omega_i$, $\omega_s \neq \omega_i$
- **Degenerate amplifier:** $\omega_p = 2\omega_s$
- **Doubly degenerate amplifier:** $\omega_p = \omega_s$

Parametric amplifiers are usually not only classified into non-degenerate and degenerate types following their physical implementation, but also into phase-preserving and phase-sensitive behaviours; as we will see these classifications correspond to other.

1.1.2 Phase preserving and phase sensitive amplifiers

Quantum mechanically the population of each mode (pump, signal and idler) is conveniently specified using its creation and annihilation operators. We consider the signal mode, centred at the frequency ω_a, described by an operator a; the idler mode, centred at the frequency ω_b, described by an operator b; as well as the pump mode, centred at the frequency ω_c, described by an operator c. The purpose of an amplifier is to increase the amplitude of the input signal by a factor for $\sqrt{G}$ as :

$$a_{out} = \sqrt{G} a_{in} \tag{1.1}$$

where G is the power gain of the amplifier. a_{in} corresponds to the incoming microwave signal in the transmission line. a_{out} corresponds to the outgoing amplified microwave signal in the transmission line. We can also define the two mode quadratures: the in-phase quadrature $X_{a_{in}}$ and the out-of phase quadrature $Y_{a_{in}}$ as:

$$X_{a_{in}} = \frac{a_{in} + a_{in}^{\dagger}}{2} \tag{1.2}$$

$$Y_{a_{in}} = \frac{a_{in} - a_{in}^{\dagger}}{2i} \tag{1.3}$$

Equation (1.1) can hold only for G = 1 because the canonical commutation relation $[a_{in}, a_{in}^{\dagger}] = [a_{out}, a_{out}^{\dagger}] = 1$ [10, 45]. Here, we can understand the role of the idler mode. In fact, the

equation (1.1) can be satisfied $G > 1$, only, if we add a second term such as:

$$a_{out} = \sqrt{G}a_{in} + \sqrt{G-1}b_{in}^{\dagger} \tag{1.4}$$

This amplification process can be established when a strong pump tone at the sum frequency of signal and idler ($\omega_p = \omega_s + \omega_i$) provides the necessary energy.
In addition, the idler mode has also a second import role in terms of noise. Depending on b_{in}, the linear amplifier can be classified into two categories based of how they treat these two quadratures:

1. Phase-preserving amplifier ($b \neq$a*and*<b>$= 0$) : $The two quadratures are amplified by the same gain \sqrt{G}$ at the same time (see figure (1.2.a). As a consequence, the relationship (1.4) becomes much clearer : $< a_{out} >= \sqrt{G} < a_{in} >$. In this case, one can not distinguish between the signal and the idler [b_{in}, a_{in}^{+}], as the signal information is distributed over and mixed into both [45]. The minimum noise energy added to the input signal by a phase preserving amplifier is one-half a photon at the signal frequency $\hbar\omega/2$, where $\hbar$ is reduced Planck constant or Dirac constant [12].

2. Phase-sensitive amplifier ($b = a$): One quadrature is amplified by $\sqrt{G}$ and the second one is attenuated by $1/\sqrt{G}$ (see figure 1.2.b). The phase-sensitive amplifier depends only on the signal input field and its conjugate, and no mixing with an idler field occurs: $b_{in} = a_{in}$. This amplifier is subject only to a lower limit on the product of the noise added to the two quadratures, and can thus squeezes the quantum noise in one quadrature at the expense of an extra noise in the other [12].

We will now discuss the performances of the different kinds of amplifiers.

1.1.3 The standard quantum limit

The noise properties of PAs are related to the type of amplifier, phase-preserving or phase sensitive amplifier and more precisely to their ability to generate squeezed electromagnetic radiations [46–48]. In fact, the standard quantum limit (SQL) refers to the minimum level of quantum noise which can be obtained without the use of squeezed states of light. In the case of parametric amplifiers, the quantum limit exists for the amount of noise added by a linear phase-preserving amplifier while a linear phase-sensitive amplifier can add no noise at all. This quantum limit is best discussed in the paper of Caves [10], in 1982 but has been discovered before in 1962 by Haus and Mullen. We can summarize the fundamental theorem of Caves for both phase-preserving and phase sensitive amplifiers in these two inequalities:

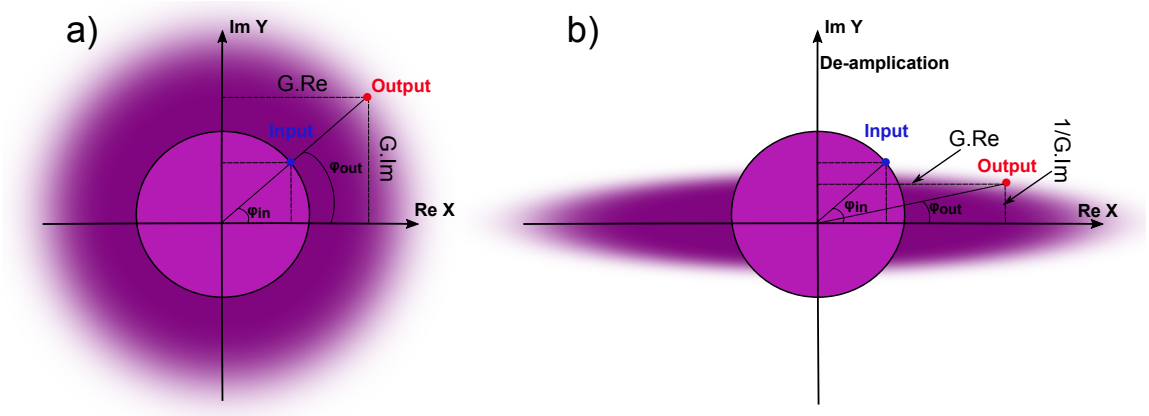

Figure 1.2 **Phase preserving and phase sensitive parametric amplifiers a)** With a phase preserving amplifier both quadratures are amplified by the same gain $\sqrt{G}$. With this kind of amplifier, the minimum of added noise is one half of photon. **b)** Under phase sensitive amplifier one of two quadrature is amplified by $\sqrt{G}$ while the second one is reduced by $1/\sqrt{G}$. This type of amplifiers can amplify the signal without added noise.

Phase-preserving amplifier:

$$A \geq \frac{1}{2}|1 \pm G^{-1}| \tag{1.5}$$

G and A are respectively the gain and the added noise number. The upper sign holds for phase-preserving amplifiers where the phase shift of the input signal produces the same phase shift of the output signal. The lower sign holds for phase-conjugating amplifiers where the phase shift on the input signal produces the opposite phase shift on the output signal [10].

Phase-sensitive amplifier:

$$(A_1 A_2)^{\frac{1}{2}} \geq \frac{1}{4}|1 \pm (G_1 G_2)^{-\frac{1}{2}}| \tag{1.6}$$

G_1, A_1 are respectively the gain and the added noise for the in phase quadrature. G_2, A_2 are respectively the gain and the added noise for the out-of-phase quadrature. When $G_1 = \frac{1}{G_2}$, the input added noise of such amplifier is zero. And so the concept of quantum limit exists only for phase preserving amplifiers not for phase sensitive ones[10].

This theorem is quoted many times because of the motivation of researchers to implement amplifiers that can be used with the lowest possible noise. In the next section we give some examples of both kinds of amplifiers based on superconducting circuits.

1.1.4 Quantum limited amplifiers based on superconducting circuits

Superconducting circuits are the only platform so far to implement quantum limited amplifiers on microwave fields. Here, we briefly describe previous and present works on several kinds of such amplifiers. We choose to classify this works in two groups: parametric amplifiers based on Josephson junctions and parametric amplifiers based on non-linearities in superconducting thin films:

Amplifiers based on Josephson junctions Josephson junctions play a key role in building low-noise microwave amplifiers, being the only strongly non-linear dissipation-less element available at microwave frequencies.

One of the implementations of parametric amplifiers based on Josephson junctions is the amplifier studied by Yurke et al, in 1986 [49]. The sample consists of a DC-SQUID coupled to a magnetic flux through a current bias line in order to adjust the critical current of the SQUID. Two transmission lines are used for the pump and the signal. This amplifier acts as a phase sensitive amplifier in order to generate squeezed states of microwave fields. The measured gain is around 37 dB and the noise temperature is around 4 photons.

There is also the Josephson parametric converter (JPC) developed in Yale and ENS Paris [37, 13], in 2010. It implements a non-degenerate phase-preserving parametric amplifier, with three separated modes (pump, signal and idler) associated to three different resonators. A Josephson ring modulator (JRM) is used to do this separation. The JRM is composed of four nominally identical Josephson junctions threaded by a magnetic flux Φ. When $\Phi = \Phi_0/2$, the amplifier suppresses the higher order terms of the non-linear coupling of the JRM useless for amplification. The JPC is the first parametric amplifier released operating virtually at the quantum limit. The measured gain is 20 dB over 5 MHz. JPC acts as a reflection amplifier but can also be used as a directional amplifier by cascading two amplifiers giving a transmission gain around 12dB [50, 51].

Parametric amplifiers with Josephson junction arrays have been realized by many groups [11, 52]. The array of junctions is here treated as a lumped element. The Quantronic group release one of such amplifiers. It is based on a superconducting lumped LC resonator with the inductor L including an array of 8 SQUIDs [52]. This amplifier is parametrically pumped by modulating the flux threading the SQUIDs at twice the resonator frequency. The obtained gain is 31 dB over 60 MHz.

Recently, in the group of I.Siddiqi, Quantum Nanoelectronics Laboratory (QNL), developed a travelling wave parametric amplifier (TWPA) based on a Josephson junction transmission line, it got a lot of success [53, 15]. The transmission line is composed of 2024 Josephson junctions coupled to LC resonators. This non-linear transmission line is used to parametrically amplify weak propagating microwave signals. The same idea is used to implement travelling wave parametric amplifiers based on the kinetic inductance of superconducting films [38] (see below). In contrast to other JPA's, the TWPA acts as a transmission amplifier. This is a large advantage because we do not need to integrate a microwave circulator in the circuit which introduces losses. This amplifier operates with 20 dB of gain over a 3-GHz bandwidth. The measured system noise is 602 ± 15 mK. This result seems good comparing with the performance of another existing amplifiers. However, TWPAs are complex to fabricate.

Amplifiers based on superconducting films Like the Josephson junction, a thin superconducting wire has also nonlinear effects arising from a current induced magnetic field penetrating into the superconducting thin film. It behaves as a non-dissipative inductor for currents below a critical current I_c. This current dependent kinetic inductance can be modelled as an effective kerr nonlinearity [54]. J.Zmuidzinas et al use this effect in a NbTiN coplanar wave guide. This amplifier acts as a transmission amplifier thanks to four-wave mixing (FWM). The parametric gain is around 10 dB over 3 GHz. However, the measured noise is 3.4 photons which is far from the quantum limit. This amplifier is also called traveling wave parametric amplifier (TWPA) and its working principle is also very close to the travelling wave amplifier based on Josephson junction arrays developed by I.Sidiqqi et al [15]. In fact, both of these amplifiers are based on superconducting transmission lines with non-linear inductances.

In the previous sections, we have introduced what the parametric amplifier is and we gave a few examples of such amplifiers, based on superconducting circuits. The JPAs use non-linear superconducting reactive elements to reach low noise amplification. This parametric aspect through a non linear medium gives the conversion of the microwave pump at frequency ω_p to the microwave signal at frequency ω_s and the idler at frequency ω_i with $\omega_p = \omega_s + \omega_i$, allowing to well control the idler mode. If this complementary mode is in its quantum ground state, the added noise is minimal. In DC amplifier, however, it is very difficult to control the idler mode because the fluctuation of the pump (classical source: DC-voltage or DC-current sources) but it is usually simpler to operate. The question that we

can ask is: Is it possible to implement a DC Josephson amplifier able to amplify close to the quantum limit? This is the question we want to answer in this thesis.

1.2 Inelastic Cooper pair Tunnelling Amplifier (ICTA)

As we explained above when the idler mode is in its quantum ground state (phase-preserving amplifier), the added input noise is one half of a photon (see section (1.1.3)). Josephson parametric amplifiers, where the nonlinear inductance of Josephson junctions is used to couple a microwave pump tone to the signal mode, have a perfectly well defined idler mode at the frequency ω_i, the difference of (a multiple of) the pump frequency and the signal frequency. This frequency can be matched to a dedicated mode in the circuit which can then be put in its ground state by strongly coupling it to a dedicated cold dissipator with temperature $T \ll \hbar\omega_i/k_B$. k_B is the Boltzmann constant. In DC powered amplifiers, on the other hand, the idler mode is usually not well identified. For example, in HEMT amplifiers it corresponds to electronic degrees of freedom inside the transistor. In addition, the transistor dissipates a large power, making it difficult to cool the electronic degrees of freedom efficiently. In DC-powered superconductor-based amplifiers such as the superconducting low-inductance galvanometer (SLUG) [16, 17] or single junction amplifier (SJA) [55] the idler frequency is not well defined and can be seen as one of the modes of the dissipative shunt of the junction. Moreover this shunt also dissipates most of the DC power and gets hot, as explained in the introduction. Here we propose and implement a new amplification scheme, which we call Inelastic Cooper pair Tunnelling Amplifier (ICTA), based on a Josephson junction biased at a DC voltage V.

1.2.1 Working principle of the ICTA

In a DC voltage biased Josephson junction and below the superconducting gap, a Cooper pair can tunnel only by dissipating its energy 2eV in the form of one or several photons as we describe in the introduction. One-photon processes are what leads to the AC Josephson effect at high power [6]. For amplification, we focus on two-photon processes instead (see figure (1.3)), which are reminiscent of the parametric down-conversion processes used in parametric amplifiers. In our scheme, the tunneling of a Cooper pair of an energy $2eV$ plays the same role as the absorption of a pump photon at the Josephson frequency $\omega_J = 2eV/\hbar$[56]. In fact, when a signal is applied at one of the two frequencies involved, this process is accelerated due to stimulated emission and the microwave power emitted by the circuit is increased.

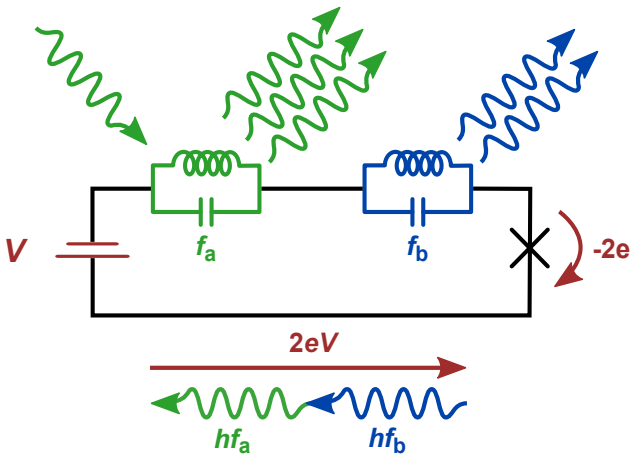

Figure 1.3 **ICTA scheme:** A Josephson junction in series with two resonators at frequencies f_a and f_b is biased at a DC voltage V . The energy $2eV$ of a tunneling Cooper pair can be converted into two photons, one in each resonator. When a microwave signal is applied at $f_s \approx f_a$, the process is accelerated due to stimulated emission in phase with the incoming signal, i.e. it gives rise to gain. Photons emitted without incoming signal is the unavoidable quantum noise of the amplifier.

Moreover, this stimulated response is in phase with the input signal. Therefore, the device acts as a phase preserving amplifier operating in reflection.

1.2.2 Theoretical Model

An excellent explanation of JPA theory is given by M.Devoret in "Collège de France" lectures, in 2010-2011. We used these lectures notes with a few references [12, 13, 57–59, 45] to build an analogue theory for ICTA.
We consider a Josephson junction with a Josephson energy E_J embedded in a circuit with two superconducting LC resonators, A and B, with resonant frequencies, respectively, ω_a and ω_b (see figure (1.3)). The junction is DC biased at voltage V_{dc}.

The system's Hamiltonian, in Schrödinger picture, is:

$$H_{sys} = \hbar\omega_a a^\dagger a + \hbar\omega_b b^\dagger b - E_J cos(\varphi) \tag{1.7}$$

This Hamiltonian represents two independent harmonic oscillators (two first terms) written in terms of quantized field amplitudes a, $a^\dagger$, b and $b^\dagger$ associated with each degree of freedom. We define the resonance frequencies of each of them $\omega_{a,b} = \dfrac{1}{\sqrt{L_{a,b}C_{a,b}}}$ and corresponding

characteristic impedances $Z_{a,b} = \sqrt{\frac{L_{a,b}}{C_{a,b}}}$. The third term corresponds to the Josephson junction Hamiltonian.

Using Kirchhoff's laws, we express the phase of the Josephson junction, φ, as a linear combination of three terms depending of the properties on the two modes, A and B, and the voltage V_{dc}:

$$\varphi = \omega_J t + \rho_a(a^\dagger + a) + \rho_b(b^\dagger + b) \tag{1.8}$$

with $\omega_J = \frac{2eV_{dc}}{\hbar}$ and $\rho_{a,b} = \sqrt{\frac{\pi Z_{a,b}}{R_Q}}$. $R_Q = h/4e^2$ is the superconducting resistance quantum. To switch to the Dirac picture, we write the Hamiltonian of the system (Equation 1.7) as sum of two terms, $H_{sys} = H_0 + H_I$, with $H_0 = \hbar\omega_a a^\dagger a + \hbar\omega_b b^\dagger b$ a time-independent Hamiltonian and $H_I = -E_J cos(\varphi)$ a time-dependent Hamiltonian describing the perturbation due to the interaction on this system.

Using the evolution operator $U_0(t) = e^{\frac{-iH_0 t}{\hbar}}$ and the identities for bosonic operators $e^{-\alpha a^\dagger a} f(a, a^\dagger) e^{\alpha a^\dagger a} = f(ae^\alpha, a^\dagger e^{-\alpha})$ we can write the system Hamiltonian H_{sys}, developed up to second order in ρ_a and ρ_b, as $H_{sys} = \sum_\pm (H_{\pm s} + H_{\pm a} + H_{\pm c})$. Where:

$$H_{\pm s} = -i\frac{E_J}{2}\left(\rho_a a^\dagger e^{-i(\pm\omega_J - \omega_a)t} + \rho_b b^\dagger e^{-i(\omega_J - \omega_b)t}\right) + h.c. \tag{1.9}$$

$$H_{\pm a} = \frac{E_J}{2}\rho_a\rho_b a^\dagger b^\dagger e^{-i(\pm\omega_J - \omega_a - \omega_b)t} + h.c. \tag{1.10}$$

$$H_{\pm c} = \frac{E_J}{2}\rho_a\rho_b a b^\dagger e^{-i(\pm\omega_J + \omega_a - \omega_b)t} + h.c. \tag{1.11}$$

We can perform this development when

$$\rho_a\langle a\rangle, \rho_b\langle b\rangle \ll 1. \tag{1.12}$$

ρ_a, ρ_b are fine structure constants, slightly renormalized by geometry and materials. Unless resonators are specifically designed for high impedance, which is not in our interest, they are typically of the order of 0.01. However, inequalities (1.12) also require the photon numbers to be sufficiently low. As explained in the next chapter this limits the maximum input power.

We now suppose that

$$\frac{E_J}{2\hbar}\rho_a,\ \frac{E_J}{2\hbar}\rho_b,\ \frac{E_J}{2\hbar}\rho_a\rho_b \ll \omega_a,\ \omega_b,\ |\omega_a - \omega_b|. \tag{1.13}$$

This allows to neglect terms rotating at frequencies ω_a, ω_b, $|\omega_a - \omega_b|$ or faster. This is always the case for H_{-s} and H_{-a}, but depending on the bias voltage, i.e. the value of ω_J, we can neglect other terms as well and in the end choose specific terms to rotate slowly and become dominant.

Amplification process

The Hamiltonian H_{+a} rotates slowly and becomes dominant when we choose $\omega_J = \omega_a + \omega_b$. According to the assumption (1.13) all other terms then rotate fast enough to be neglected. Back to the Schrödinger picture, the rotating wave approximation (RWA) therefore allows us to simplify the Josephson Hamiltonian (1.7):

$$H_a^{RWA} = \hbar\omega_a a^\dagger a + \hbar\omega_b b^\dagger b + \hbar\lambda(a^\dagger b^\dagger e^{-\omega_j t} + abe^{+\omega_j t}). \tag{1.14}$$

Where λ is the coupling constant which governs the non linearity of the system

$$\lambda = E_j \frac{\rho_a \rho_b}{2\hbar}. \tag{1.15}$$

The Hamiltonian (1.14) is analogous to the JPA Hamiltonian [12]: The two terms $\hbar\omega_a a^+ a$ and $\hbar\omega_b b^+ b$ describe the isolated resonators and the term $a^+ b^+ e^{-\omega_j t}$ describes the transformation of the pump energy (modelled by a classical operator) to a pair of signal and idler photons, respectively, at ω_a and ω_b. In other words, the energy of a tunnelling Cooper pair is converted into signal and idler photons at ω_a and ω_b . This third term gives the conversion process with power gain: **amplification**.

Noiseless frequency conversion process

If instead we choose $\omega_J = |\omega_a - \omega_b|$ either H_{+c} (for $\omega_a < \omega_b$) or H_{-c} (for $\omega_a > \omega_b$) become slow and dominant; while all other terms rotate quickly and can be neglected. Back to the Schrödinger picture we obtain:

$$H_{\pm c}^{RWA} = \hbar\omega_a a^\dagger a + \hbar\omega_b b^\dagger b + \hbar\lambda(ab^\dagger e^{\mp\omega_j t} + a^\dagger b e^{\pm\omega_j t}) \tag{1.16}$$

In the Hamiltonian (1.16), we also have the two first terms corresponding to the resonators and the term $a^+ b e^{\mp\omega_j t}$ describes the transformation of a photon at the frequency ω_b to another photon at the frequency ω_a using the energy of a Cooper pair tunneling in the sense / against the bias voltage. In other words, one photon at frequency ω_b is absorbed and one

photon at frequency ω_a is emitted while the energy conservation balance is satisfied thanks to Cooper-pair tunnelling. This third term gives the conversion process without photon gain: Noiseless frequency conversion.

Drive terms

The terms in H_{+s} are coherent drive terms which we do not consider here. They are of lower order as the terms we have discussed, but they can still be neglected if they are off-resonant.

1.2.3 Input-Output theory

The input-output theory **IOT** is a method allowing to calculate the quantum statistical properties of both, the field inside our system and the field exiting our system given the input field (circuit shown in figure (1.4)). To extract the information from the circuit, we couple each oscillator, A and B, with two semi-infinite transmission lines (TL): first transmission line, driven at the frequency ω_s feeds the resonator A, and the second transmission line, driven at the frequency ω_i, feeds the resonator B. These transmission lines, coupled to the resonators A and B, imposed boundary conditions [17, 60]:

$$a_{in} + a_{out} = \sqrt{\gamma_a} a \tag{1.17}$$

$$b_{in} + b_{out} = \sqrt{\gamma_b} b \tag{1.18}$$

With $\gamma_{a,b}$ the energy relaxation rates of resonators A and B.
Following the usual treatment of parametric amplifiers, we add the dissipation term to the Hamiltonian (Equation 1.7) and by using input-output theory, we arrive at quantum Langevin equations [17] and then to the amplifier equations:

$$\frac{da}{dt} = -i\omega_a a - \lambda b^\dagger e^{-i\omega_J t} - \gamma_a a + \sqrt{2\gamma_a} a_{in} \tag{1.19}$$

$$\frac{db}{dt} = -i\omega_b b - \lambda a^\dagger e^{-i\omega_J t} - \gamma_b b + \sqrt{2\gamma_b} b_{in} \tag{1.20}$$

To understand these two equalities, we associate each column to a physical phenomenon: The first column (green) describes the resonators, the second column (blue) the coupling term producing photon conversion, the third column (violet) the dissipation term and the last column (cyan) the coupling of the input field to the resonators. Note that in our case, we don't have another third equation for the pump wave because we assume it is a classical operator and not quantum operator.

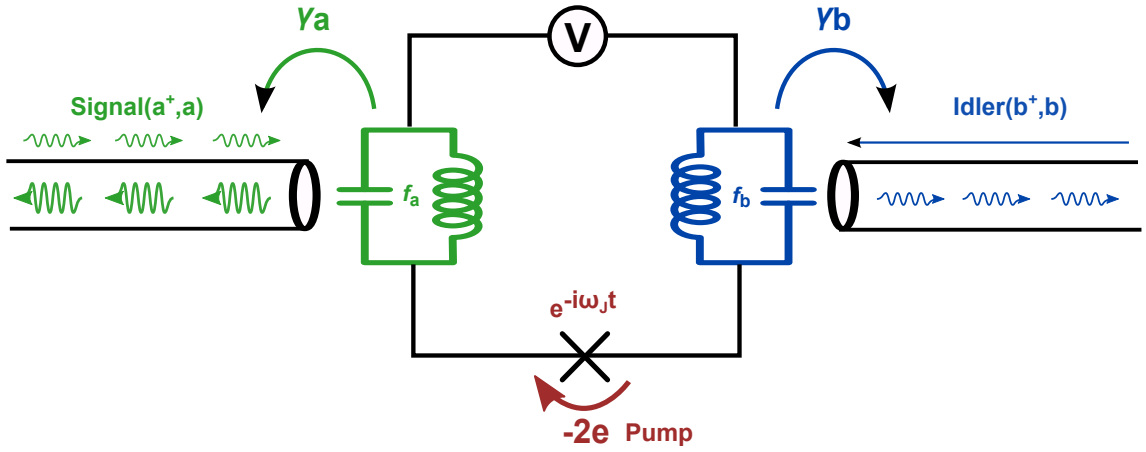

Figure 1.4 **Input-output theory representation:** transmission lines connected to two microwave resonators, with resonance frequencies f_a and f_b, and a Josephson junction with coupling energy E_J. When impedance matched, an incoming photon of frequency $f_s \approx f_a$, introduced in one resonator leave with a rate γ_a, amplified by stimulate emission. The signal is reflected and then leaved through the same transmission line.

Scattering matrix

Substituting the expressions (Equations 1.18) in the parametric amplifier equations (1.20,1.20), we obtain the relationships :

$$(1.19) \Longrightarrow \left(\frac{d}{dt} + i\omega_a + \gamma_a\right) a_{out} + i\lambda\sqrt{\frac{\gamma_a}{\gamma_b}} b^{\dagger}_{out} e^{-i\omega_J t} \tag{1.21}$$

$$= \left(-\frac{d}{dt} - i\omega_a + \gamma_a\right) a_{in} - i\lambda\sqrt{\frac{\gamma_a}{\gamma_b}} b^{\dagger}_{in} e^{-i\omega_J t} \tag{1.22}$$

$$(1.20) \Longrightarrow \left(\frac{d}{dt} + i\omega_b + \gamma_b\right) b_{out} + i\lambda\sqrt{\frac{\gamma_b}{\gamma_a}} a^{\dagger}_{out} e^{-i\omega_J t} \tag{1.23}$$

$$= \left(-\frac{d}{dt} - i\omega_b + \gamma_b\right) b_{in} - i\lambda\sqrt{\frac{\gamma_b}{\gamma_a}} a^{\dagger}_{in} e^{-i\omega_J t} \tag{1.24}$$

Using the following definition for the Fourier transform, we can write the input field at ω_s as:

$$\hat{a}(\omega_s) = \frac{1}{\sqrt{2\pi}} \int a(t) e^{-i\omega_s t} dt \tag{1.25}$$

Then, we drive from (1.24) and (1.18) and by using (1.25), the scattering matrix of the signal and idler amplitudes though RWA in the frequency domain after Fourier transform.

$$\begin{pmatrix} a_{out} \\ b_{out} \end{pmatrix} = S \begin{pmatrix} a_{in} \\ b_{in} \end{pmatrix}$$

With,

$$S = \begin{pmatrix} r_{aa} & t_{ab} \\ t_{ba} & r_{bb} \end{pmatrix} = \begin{pmatrix} \frac{\eta_a^* \eta_b^* + \xi^2}{\eta_a \eta_b^* - \xi^2} & \frac{-2i\xi}{\eta_a \eta_b^* - \xi^2} \\ \\ \frac{2i\xi}{\eta_a \eta_b^* - \xi^2} & \frac{\eta\eta + \xi^2}{\eta_a \eta_b^* - \xi^2} \end{pmatrix} \tag{1.26}$$

Where,

$$\eta_a = 1 - i\frac{(\omega_s - \omega_a)}{\Gamma_a} \tag{1.27}$$

$$\eta_b = 1 - i\frac{(\omega_i - \omega_b)}{\Gamma_b} \tag{1.28}$$

$$\xi = \frac{\lambda}{\sqrt{\Gamma_a \Gamma_b}} \tag{1.29}$$

$$\tag{1.30}$$

We can understand the scattering matrix as follows: incoming photons from the left-hand (right-hand) side transmission line interact with the Josephson junction, which creates a reflected field to the left (right) given r_{aa} (r_{bb}) and a converted field to the right (left) of the Josephson junction t_{ab} (t_{ba}).

1.2.4 Characterisation of the ICTA

Four factors govern the performance of any amplifier:
Power Gain: It is defined as the mean ratio of the output power P_{out} to the input power P_{in}: $G = \frac{P_{out}}{P_{in}}$.
Typically expressed in decibels (dB): $10\log_{10}(G)$.
Bandwidth: Any amplifier should have a bandwidth suited to the range of frequencies it is intended to amplify. Here, we use the concept of - 3 dB bandwidth: It is the frequency range considered useful where the gain decreases less than factor 2 (3 dB) from its maximum value.
Dynamic range: It is the input power up to which the amplifier gain is almost constant. In this work, we use mostly the concept of -1 dB compression point which corresponds to the value of the signal power P_{in} at which the ICTA gain decreases by 1 dB.
Noise: Signal of the system which is unwanted and which degrades the signal.

An ideal amplifier should work with a high gain, operate over a broad frequency range, have a large dynamic range and of course very low noise, close to the quantum limit.

ICTA Gain:

The scattering matrix (1.26) allows to find the power gain G of the circuit:

$$\sqrt{G} = |r_{aa}| = |r_{bb}| \tag{1.31}$$

$$\sqrt{G} = \frac{\eta_a^* \eta_b^* + \xi^2}{\eta_a \eta_b^* - \xi^2} \tag{1.32}$$

On the resonance $\omega_s = \omega_a$ and $\omega_i = \omega_b$, we rewrite G as a function of the Josephson energy, and the characteristic impedances of resonators A and B:

$$G_0 = \left(\frac{1+\xi^2}{1-\xi^2}\right)^2 \tag{1.33}$$

With ξ given by

$$\xi = E_j \frac{\pi\sqrt{Z_a Z_b}}{R_Q \hbar \sqrt{\gamma_a \gamma_b}} \tag{1.34}$$

The ICTA gain is defined by ξ, the damping terms $\gamma_{a,b}$ and the characteristic impedance of the resonators associated to the signal and idler modes $Z_{a,b}$. ξ is tunable via the Josephson energy if a SQUID is used. Moreover for large gain, ξ must be slightly small than 1.

ICTA bandwidth:

The -3 dB bandwidth of Inelastic Cooper pair Tunneling Amplifier is then:

$$B_0 = 4\frac{\gamma_a \gamma_b}{\gamma_a + \gamma_b} G_0^{-\frac{1}{2}} \tag{1.35}$$

This expression shows that the bandwidth of the amplifier is inversely proportional to the amplitude gain $\sqrt{G_0}$. This gain-bandwidth compromise is a common property of many amplifiers, including parametric amplifiers both degenerate and non degenerate. Then the bandwidth of our amplifier gets smaller as we increase its gain. As we will see, this is not a fundamental limit, but rather due to the Lorentzian shape of our modes.

ICTA noise:

In order to calculate the ICTA added noise, we have to define first the output photons generated per mode:

$$n_{a,b}^{out} = |r|^2 n_{a,b}^{in} + |t|^2 n_{b,a}^{in} \tag{1.36}$$

Table 1.1 Analogies with existing JPA.

JPA	ICTA
Pump amplitude	Josephson energy
Pump frequency	Voltage bias
Josephson energy	Admittance

This equation is taken from [12]. n^{in} is the input photon spectral density calculated from $\langle a_{in}[\omega]a_{in}[\omega]'\rangle$. In thermal equilibrium, the dominant noise at each port is determined by the zero-point fluctuations. Then, for high gain $|r|^2 \gg 1$, the number of noise equivalent photons is effectively:

$$n_{eq}^{in} = \frac{n_{out}}{|r|^2} \tag{1.37}$$

Similar to JPAs, the input added noise expressed in the photon spectral power density [12], is defined by:

$$n_{add} = n_{eq}^{in} - n_{in} \tag{1.38}$$

For $G \gg 1$ and if $n_{b,a}^{in} = \frac{1}{2}$,

$$n_{add} = \frac{1}{2} \tag{1.39}$$

ICTA dynamic range:

We have neglected the higher order terms in order to arrive to equation () tend to reduce the gain of the amplifier. These terms start to play a role when $\rho_a^2 \langle a^\dagger a\rangle \approx 1$ or $\rho_b^2 \langle b^\dagger b\rangle \approx 1$. This correspond to:

$$\left\langle a_{in}^\dagger a_{in}\right\rangle = \frac{\gamma\langle a^\dagger a\rangle}{G+1}$$

Analogies with existing Josephson amplifiers

In the derivation made in the previous sections we shown that the theory developed to calculate the performance of the ICTA is very similar to the one for the JPA.

Here, we discuss the results shown in previous paragraph and we compare them with their equivalents for the JPA case. This comparison is summarized in the table (1.1).
Let's start first with the ICTA gain. The equation (1.33) shows that we have maximal gain $G_0 \to \infty$ only when $\xi \to 1$. This constant is proportional to the Josephson energy as shown in equation (1.34). In fact, in the case of Josephson parametric amplifier ξ scales with A_{pump}/E_J, where A_{pump} is the microwave pump amplitude. In the case of the ICTA, it will be

sufficient to increase the Josephson energy. We can do that by using a SQUID for example. In the section (3.2), we discuss this point in detail. So it is quite clear that the Josephson energy in our case plays the role of the microwave pump amplitude in the JPA case, the voltage bias plays the role of the pump frequency according to the resonance condition $2eV = \hbar\omega_s + \hbar\omega_i$ and finally the inverse of the characteristic impedance $Z_a Z_b$ to E_J in JPA case.

Comments: Validity of the quantum theory

It is important to clarify that we treat the coupling of the resonators to the transmission lines as a perturbation ($\gamma_{a,b} \ll \omega_{a,b}$). These damping terms $\gamma_{a,b}$ are related to the quality factors and imply Lorentzian shaped modes (see section 1.2). This condition imposes a strict limitation on the choice of the form of impedance seen by the junction. So what about an arbitrary electromagnetic environment? To answer to this question, we use a semi classical model based on the P(E) theory:

1.3 Semi-classical theory

In the previous section, we treated the case of a special electromagnetic environment: two LC resonators in series. As explained before, this quantum theory is not valid for all forms of impedances seen by the Josephson junction. In this section, we discuss the case of an arbitrary electromagnetic environment which can be taken into account within the P(E) framework of inelastic charge tunneling [27, 30, 31, 61–63]. However, P(E) theory is a perturbative treatment of E_J, so this theory is valid only for low Josephson energy and weak gain. In fact, P(E) is the probability for a Cooper pair to tunnel through the junction, while dissipating energy E into the environment [26–29] such that:

$$\int P(E)dE = 1 \tag{1.40}$$

$P(E)$ is related to the Cooper pair tunneling rate by:

$$\Gamma = \frac{\pi}{2\hbar} E_J^2 P(2eV) \tag{1.41}$$

The photon emission density γ at frequency f can be written as function of the tunneling rate Γ at a frequency $\nu = 2eV/h$ [31, 61, 62]:

$$\gamma(\nu, f) = \frac{2}{f}\frac{ReZ(f)}{R_Q}(\Gamma(\nu - f) + \Gamma(-\nu - f)) \tag{1.42}$$

$$= \frac{\pi}{\hbar f}\frac{ReZ(f)}{R_Q}E_J^2(P(h(\nu - f)) - P(-h(\nu + f))) \tag{1.43}$$

The first term in equation (1.43) corresponds to tunneling in the sense of the bias voltage, the second term to tunneling against the bias voltage. Within the standard theory of inelastic charge tunneling, the amplification processes is explained by deriving the effective admittance of the junction at the frequency f. Probabilities for a photon impinging on the junction to be absorbed γ^- or to be reflected while stimulating the emission with an additional photon γ^+ are related to the spontaneous emission rate density (equation (1.44)) by the Einstein relations:

$$\gamma^{\pm}(\nu, f) = \gamma(\nu, \pm f) \tag{1.44}$$

These rates result in an effective junction admittance Y defined by:

$$\mathrm{ReY}(\nu, f) = \frac{1}{4\mathrm{Re}Z(f)}(\gamma^-(\nu, f) - \gamma^+(\nu, f)) \tag{1.45}$$

$$= \frac{e}{hf}(I(\nu + f) - I(\nu - f)) \tag{1.46}$$

$I = 2e\Gamma$ is the DC current through the junction. When the second term dominates, the junction admittance becomes negative, leading to a reflection coefficient of magnitude > 1.

In order to calculate the response at high input power, we consider a sine wave at frequency $f_0 = \omega_0/2\pi$ applied to the junction on top of the DC bias: $V_s = V_{0s}cos(\omega_0 t)$. We then get the phase φ_{ac}

$$\varphi_{ac} = \frac{2e}{\hbar}\int V dt = \frac{2e}{\hbar}\frac{V_{0s}}{\omega_0}sin(\omega_0 t) \tag{1.47}$$

According to equation (8) in reference [61] and by using equation (1.47), the DC current with applied V_s is:

$$I(2eV) = \delta_0 \sum_n |J_n(\frac{2eV_{0s}}{\hbar\omega_0})|^2 I(2eV - n\hbar\omega_0) \tag{1.48}$$

The equation (1.48) means that the tunneling of a Cooper pair can exchange n photons of frequency ω_0 for all integer n with a probability given by a Bessel function squared. I is translated by the different harmonics of $f_J = \omega_J/2\pi$ and weighted by Bessel functions, following photo-assisted tunneling relations [64, 65]

Note that relation (1.43) and (1.48), based on the standard P(E) theory, are strictly valid only at very small critical current and for $\gamma \ll 1$, where tunneling events are so rare that the photon modes in the circuit relax to their ground state between tunneling events. In order to extend the range of validity of these equations to higher photon numbers, we can approximately take into account the non-equilibrium state of the environment by including the effective admittance of the junction itself in its electromagnetic environment [62, 61]. To do so we solve equation (1.48) self-consistently with an impedance,

$$Z_{SC}(f) = Z(f)Y^{-1}(Jf, f) \tag{1.49}$$

$$= \frac{Z(f)}{1+Y(\nu, f)Z(f)} \tag{1.50}$$

Conclusion

In this chapter, we have introduced what the ICTA is and we have shown that its working principle is very close to one of the JPAs. The main difference between these two amplifiers is the way of pumping: Usually, Josephson parametric amplifiers are driven by an external microwave pump tone. In the case of the ICTA, the energy of a tunneling Cooper pair plays the role of the pump (internal pump). This could make our amplifier easier to operate and use. We have also discussed also the ICTA performances: Gain, bandwidth, noise and dynamic range. We have calculated these characteristics in analogy to the general quantum theory developed for JPAs [12] and have shown that the ICTA gain scales with the Josephson junction energy which gives another advantage to our amplifier. However, this quantum theory is valid only for a particular electromagnetic environment, two LC oscillators. In order to cross this limit, we have developped also a semi-classical theory based on P(E) theory. From this treatment, we calculated the admittance given by the circuit. We also treat higher orders of the down-conversion terms(1.7). Before confronting this theory with experimental results, we introduce in the next chapter our experimental setup used in this work.

Chapter 2

Experimental setup

This chapter is intended to give details on the experimental methods used in this work. It describes the experimental measurements used to interrogate the samples. First, we give an overview of the used equipments employed in this thesis. Secondly, we present a series of tests and calibrations used to determine important properties of our experiments such as the gain and the noise temperature of the entire measurement chain.

2.1 The sample holder

Performing measurements of on-chip devices requires use of good sample holders able to match well the coax lines in the dilution refrigerator to the CPW lines on-chip and shield the sample from residual electromagnetic noiseS in the fridge without adding on the of extra cavity modes like the electromagnetic modes of the sample box. In this work, we use cooper sample holders fitted with eight SMA connectors positioned to the corresponding pads of our chips. Figure (2.1) shows a photograph of a sample holder used in this work. Our chips of 10x10 mm are placed in a rectangular hole in the center of the sample box and clamped down. Then Al bonds are made from the CPW's pads on the chips to their counterparts on the gold plated Printed Circuit Board (PCB). Additional bonding wires are made between the ground planes of the chip and the PCB to reduce as possible the influence of parasitic resonances on the device. The top and bottom covers are covered with microwave absorbent.

2.2 Experimental setup

Superconducting quantum circuit (SQC) at GHz frequencies require careful filtering and attenuation of microwave signals generated at room temperature and also at low temperature.

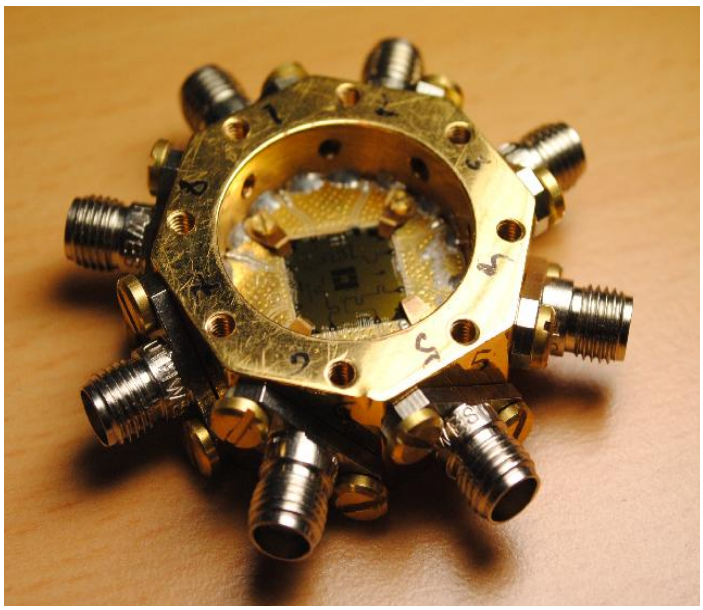

Figure 2.1 **Sample holder:** Photograph of sample holder.

Precise filtering is also requested also for the DC-branch, specially for the ICTA project, because any fluctuation on the voltage bias may increase the amplifier noise. The experiments in this work also demand also careful electrical wiring inside the dilution refrigerator. A schematic view of the fridge wiring can be found in figure (2.3). Now, we give more details on our experimental setup with its two parts : The DC branch used to apply the voltage bias to the Josephson junction and the RF branch used to measure the gain and the dynamic range of ICTA.

2.2.1 Fridge wiring

In order to clearly observe quantum phenomena in microwave circuits, the samples must be cooled down to a temperature $T \ll \hbar\omega/k_B$ to reduce the thermal noise. This means that T must be less than 50 mK for $\omega/2\pi$ = 6 GHz. All the samples presented in chapter (3) and chapter (6) are measured in a cryogen free dilution refrigerator, use a pulse-tube cooler instead of a ^{4}He bath, at temperature around 12 mK. The fridge has six input RF lines used to set the a DC magnetic flux bias in the SQUID loop or send the RF signal that we want to amplify, two output RF lines including amplifiers at 4 K to measure the reflection or the transmission coefficient of S-parameters or to measure the power spectral density, and finally two DC lines filtered at 4.2 K to voltage bias the junction. Figure (2.3) shows a photograph of our dilution refrigerator. As it can be seen in the same figure (on the right), the experimental setup is made of two identical chains (chain 1 and chain 2). We adopted this approach for two

reasons: first, in order to measure the response of a transmission amplifier, second, because correlation functions have to be measured for other projects in our group. Many cryogenic circulators, amplifiers and filters are used in our experimental setup. In the following sections, we will discuss the role of low temperature electronics included in our experimental circuit.

In order, to better understand the setup, we have indicated by arrows the propagation of the signals on the figure (2.3):

- Black arrows: to track the propagation of the amplified signal (reflection amplification) in the RF-block.
- Red arrows: to track the propagation of the flux voltage to bias the SQUID in the DC-block.
- Green arrows: to track the propagation of the flux bias to adjust the magnetic flux applied to the SQUID loop in the DC-block.

2.2.2 DC circuit

The ICTA sample box is put on the base-stage of the fridge. We try to keep the sample holders close to the switch to reduce, as possible, the losses and ground loops. In this section, we describe the propagation of the voltage bias and the flux bias through the DC branch.

In order to apply the voltage bias to the SQUID (follows the red arrows): First, the signal is well filtered via two RC-filters at 4.2 K then it gees to a bias box used to apply the voltage to the sample. This bias box consists of three identical cavities, each of them including an RLC filter that can be described as an RL parallel circuit such as R = 50 Ω and L = 270 μH, in series with two parallel capacitors C_1 = 100 nF and C_2 = 1 pF feed through between the cavities; all made in a cooper box for thermalization and also in order to reduce the noise coming from the other stages. The figure (2.2) shows the circuit of the bias box used in this work. Finally, the signal goes to a bias tee with a crossover frequency of 50 MHz (Marki DPXN-M50) used to separate the low-frequency elements (its purpose is to set the bias) and the high-frequency elements; and so the microwave signals and the voltage bias are separated.

In order to apply the flux bias to the SQUID loop (follows the green arrows): Firstly, the signal is attenuated by 20 dB at 4 K then goes through a two-port microwave switch (green square with orange star) to an Eccosorb filter. This filter at in the input of the sample in order to prevent high frequency radiation coming from high temperature components. The

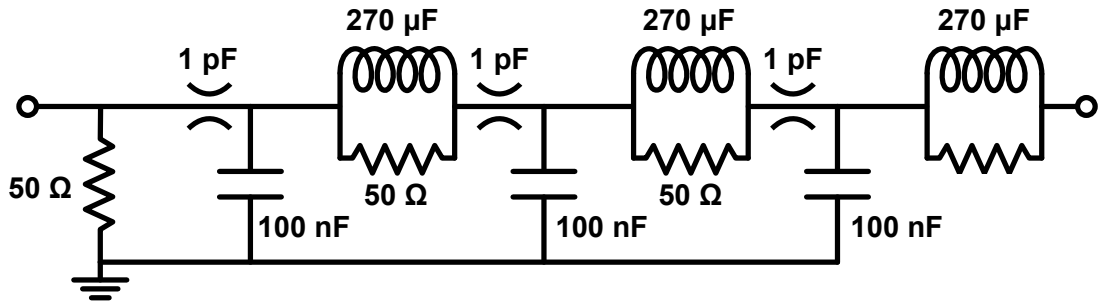

Figure 2.2 **Voltage bias box:** Circuit representation of the bias box. All the values given in the figure have been measured at 4.2 K.

operating principle of this kind of filters is to force the radiation to travel through a lossy material in a small section of the transmission line. The geometry is chosen to match the 50 Ω characteristic impedance of the microwave line. These filters have an approximately Gaussian cut-off at $\approx$ 300 MHz.

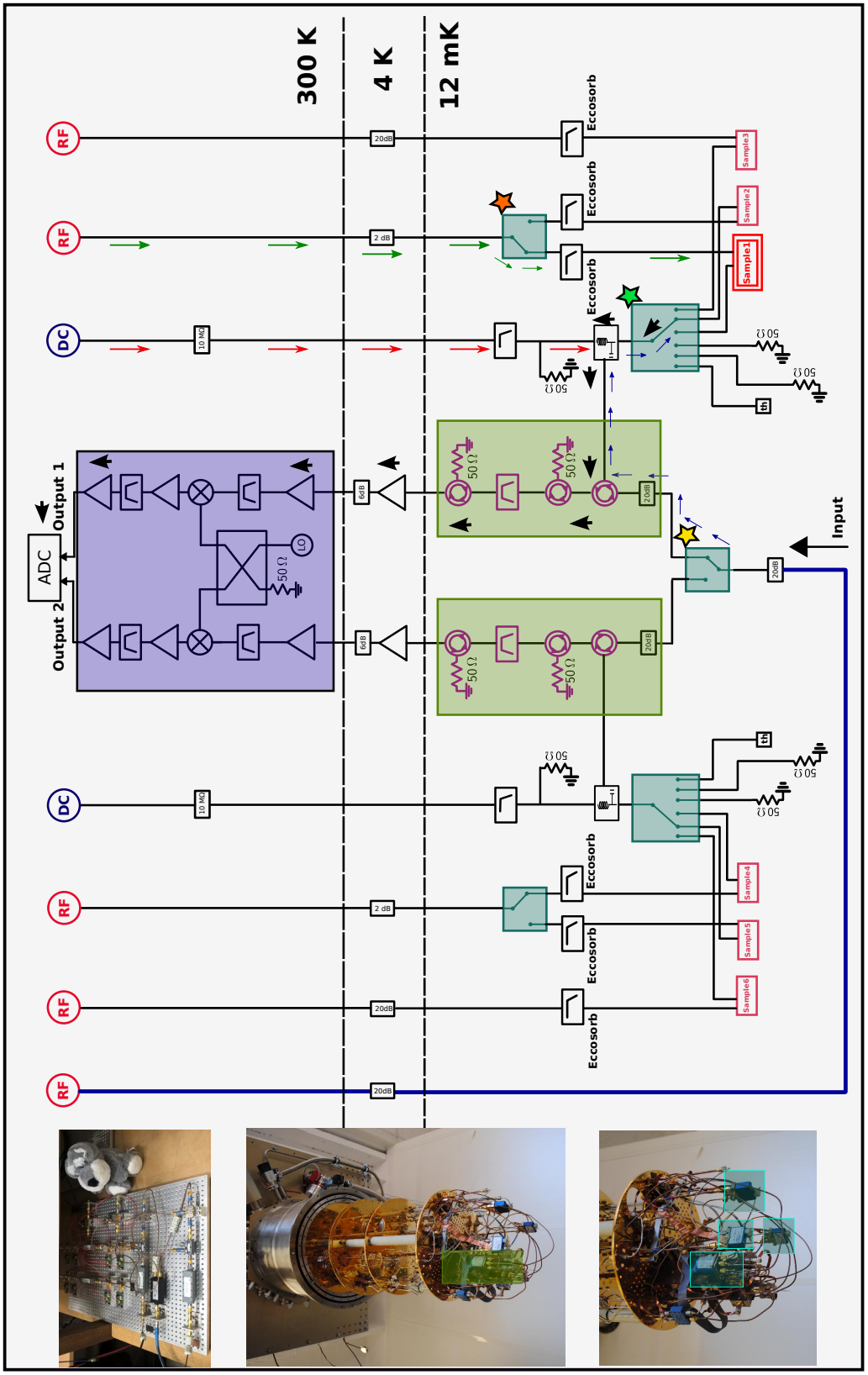

Figure 2.3 **Detailed schematics of the experimental setup:** photographs of the fridge and room temperature setup on the left. Simplified schematic of the setup on the right.

2.2.3 RF circuit

In this project, the most sensitive part of our experiment is the RF branch which is used to control the propagation of the input signal and the amplified output signal. Here, we explain how the sample (sample(1), indicated by double red squares in figure (2.3) is measured.

The input lines (wide blue line) are attenuated by 20 dB NiCr attenuators (XMA 2082-8418-20-CRYO) at 4 K and at base temperature before and after the two-port microwave switch (green square with yellow star). We choose the values of attenuation in such way that the black body radiation coming from the hotter stages is reduced, well below one photon. Then the input signal goes through a first circulator whose role is to split the input and output signals from the reflection measurement. The incoming signal continues to a bias tee and then to the sample through 6-pole single-throw switch (Radial R591763600) (green square with green star) allowing to measure several samples in a single cooldown with a single amplification chain. More importantly, we use them because the measured ICTA noise needs a precise calibration [66]. For that purpose, the six-port switch is connected to three calibration references: a 50 Ω load at 12 mK (Cold), 50 Ω load at 800 mK (Hot) and a short are used in our experimental setup (see below). To operate the switch, we send a current pulse of order of 50 mA during 6 ms to one of the six coils using a custom circuit. This operation is completely automated through python scripts.

The signal reflected from the sample passes again through the bias tee and the first circulator to a second circulator terminated on one port with a matched 50 Ω load. It is intended to isolate our system from the incoming noise. In order to fully isolate the sample from amplifier noise we must use three circulators in series. In our experiments, the circulators work between 4 and 8 GHz and each circulator has an insertion loss of about 1 dB. In addition, we also use cavity bandpass filters (Microtronics BP50403) to prevent unwanted out-of-band noise to reach our devices.

At the 4 K stage, the output reflected signal is amplified by using two Cryogenic Low Noise (LNF-LNC4-8 A). They work between 4 GHz and 8 GHz. At the optimum low noise bias (V_{ds} = 0.7 V, I_{ds} = 12 mA), a lowest noise temperature T of 1.9 K was measured between 4 GHz and 8 GHz band with gain around 44 dB. These HEMT amplifiers are the dominant source of noise in our setup.

At room temperature, the outgoing signal is amplified again in the second amplification stage by using other low noise amplifiers Miteq (AMF-5F-04000800-07-10p). In the next section, we discuss the total gain of channels, including an overview of the amplification determined by the calibration. In addition of amplifiers, we include bandpass filters between 4 GHz and 8 GHz . At this point, the signal is down converted using a mixer Marki (M1-0408LA) and filtered by a 1.1-1.9 bandpass filter (Microtronics BPI 17597) in order to avoid aliasing of our digital converter. Finally, the signal is amplified again by using Minicircuits ZX60 (four times) with a noise temperature of 627 K and 15 dB as gain before being digitized on an AlazarTech ATS9373 (2GS. s^{-1}) digitizer, using the 2nd Nyquist band.

2.3 Calibration

In order to define the average photon number emitted by samples from power spectral density measurements and to determine their gain, we perform a number of calibrations on our system. Two levels of calibrations are made in this work to extract the relevant experimental parameters:

1. **First level: Standard calibration** to determine the gains and the noise temperatures of amplification chains.

2. **Second level: ICTA calibration** to determine the gain, the noise added by the sample and the input signal power.

This section gives a brief overview of our calibration methods, performed independently (standard calibration) and dependently (ICTA calibration) on the response of the sample .

2.3.1 General calibration methods

First of all we note that, at room temperature, the signal is down converted using a mixer and a local oscillator signal allowing to measure the signal between 1-2 GHz. The signal is also amplified several times in order to match the input range of the mixer and the ADC, as explained in the previous section. This frequency down-conversion method gives the opportunity to convert the measurement frequency range, corresponding to amplifier bandwidth 4-8 GHz to a slower frequency range (1-2 GHz). In the next paragraph, we give details on the calibration in order to extract the gain and also the temperature noise of the amplification chains.

Chain gain (G_{ch}): To calibrate the gain of our amplification chain G_{ch}, we use a 6-port Radiall switch connected to two 50 Ω microwave loads at two different known temperatures 800 mK and 12 mK. We refer to this as "Hot/Cold load" setup. The noise power spectral density coming from a matched microwave load can be determined using the fluctuation-dissipation theorem as:

$$S^{calc}(\omega) = \frac{\hbar\omega}{2} coth\{\frac{\hbar\omega}{2k_BT}\} \tag{2.1}$$

Then we can calculate the difference between the noise power spectral density coming from a 50 Ω load Hot and it equivalent quantities from a 50 Ω load Cold by :

$$G_{ch}\left(S^{calc}_{Hot}(\omega) - S^{calc}_{Cold}(\omega)\right) = S^{out}_{Hot}(\omega) - S^{out}_{Cold}(\omega) \tag{2.2}$$

$S^{out}_{Hot}(\omega)$ and $S^{out}_{Cold}(\omega)$ are measured quantities, ω is known quantity, so we can extract the gain of our amplification channel G_{ch}. Figure (2.4.a) and figure (2.4.b) shows the calibrated gain, respectively, for chain 1 and chain 2 performed during the measurements that gave the results •discussed in the next chapter and chapter (6). In this two figures, we present the calibrated gain for all different local oscillators with different colors and a combined curve (black line) between 4-8 GHz. We can also define an equivalent noise temperature $\mathrm{T_{ch}}$ that we discuss below.

Chain noise (N): By measuring the total output noise of the amplification chains with each of the two loads, we can extract the noise added by the amplifiers and we can calculate an effective system noise number N. At low temperature, formula 2.1 tends towards and then,

$$S^{out}_{Cold} = \hbar\omega N G_{ch} \tag{2.3}$$

This definition includes vacuum fluctuations (and any residual thermal noise) from the cold load in the noise number. As I alluded in the previous paragraph, we need to know first the gain $\mathrm{G_{ch}}$ in order to determine N accurately. We will see in the next paragraph that these two parameters help to extract the added noise of ICTA. Figure (2.4.c) and figure (2.4.d) show the noise of amplification chains for each local oscillator (LO) used to cover the measurement frequency range as well as the combined curve (black line).

2.3.2 ICTA calibration methods

In addition to the noise of the measurement chain, the notion of noise has also another origin in our experiments which is the added noise of our amplifier. In the first chapter, we showed that an ICTA should be able to amplify with low noise, close to the quantum limit.

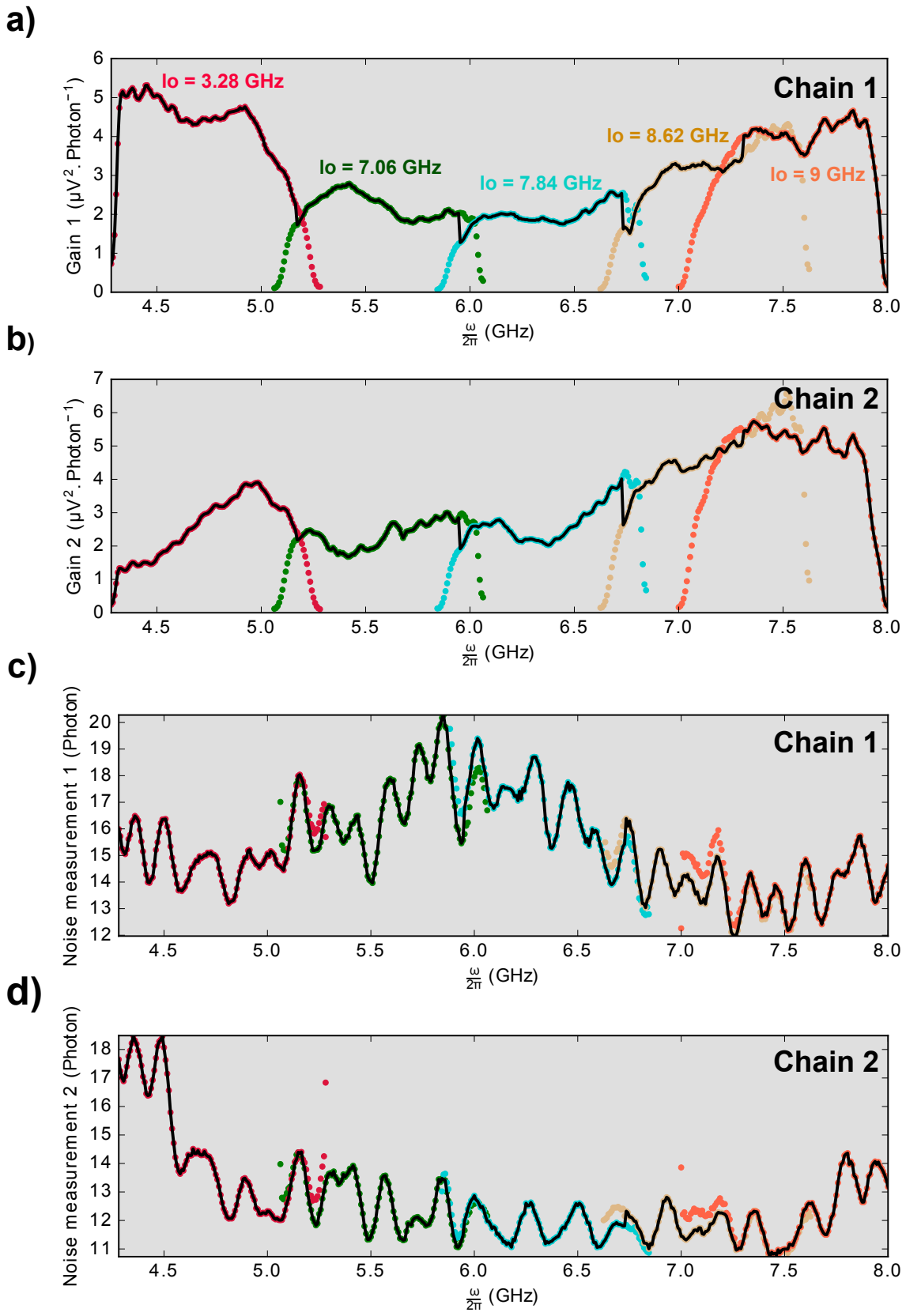

Figure 2.4 **Gains of amplification channels:** The gain of **a)** the first amplification channel **b)** and the second amplification channel for all local oscillators. The noise number of **c)** the first amplification channel **d)** and the second amplification chain for all local oscillators and their combined curves (black line) between 4-8 GHz.

In this paragraph, we describe a set of measurements that help estimate the ICTA added noise N^{add} as well as the ICTA gain and the microwave loss of the components (attenuation) A between the different location in the circuit shown in figure (2.3) to the input of the sample. As noted in the previous paragraph, we use a cryogenic switch to toggle between two terminations held at two different temperatures in order to extract the gain and also the chain noise. In addition, we can also determine the N^{add} by switching on and off the pump.

ICTA gain (G_{ICTA}): We have two possibilities to normalize the VNA measurements. They can be normalized with respect to the reflection of the short circuit or with respect to the reflection of the sample in an area without gain (where the gain is close to 1) and a fully frustrated SQUID. We observe very similar attenuation, indicating that loss between the microwave switch and the junction is negligible. However, the exact frequency dependence is not the same due to parasitic reflections in the cable connecting the switch to the sample. We, therefore, use the latter calibration which cancels these modulations which is used also to calibrate the gain of the measured samples.

ICTA noise (N^{add}): The variation of the power spectral density is measured when switching on (equation (2.4)) and off (equation (2.5)) the pump:

$$S_{on} = ((\frac{1}{2} + N^{add})G_{ICTA} + N)G_{ch} \tag{2.4}$$

$$S_{off} = \hbar\omega(\frac{1}{2} + N)G_{ch} \tag{2.5}$$

From $S_{on} - S_{off}$ and the chain gain G_{ch}, we can extract the input added noise N^{add} knowing the ICTA gain G_{ICTA}.

ICTA input power (A): We use a cryogenic switch to toggle between 50 Ω load at two different temperatures to estimate the added noises of the commercial amplifiers and the ICTA. In order to determine the dynamic range of the ICTA, we must also measure the microwave losses of the components from the microwave source to the input of the samples. In order to ensure this, we connect to the same switch another calibration reference and we refer to this as "short" setup. We apply an RF signal with frequency ν_{in} and power P_{in} by using a microwave source to the short and we measure the power spectral density PSD for different frequencies ν between 4 GHz and 8 GHz.

$$PSD(\nu) = \left\{ \left(\frac{P_{in}}{h\nu_{in}} \right) .\delta(\nu - \nu_{in}) + N \right\} G_{ch} \tag{2.6}$$

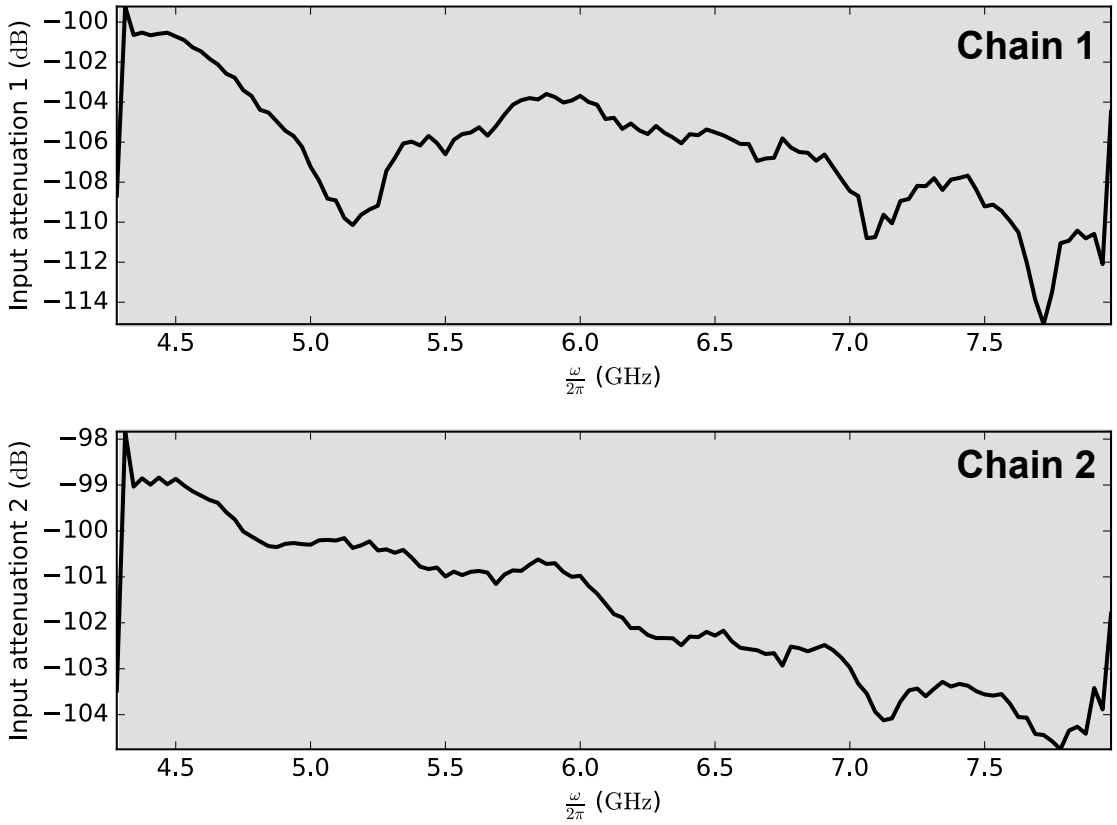

Figure 2.5 **Input attenuation:** The input attenuation of **a)** first amplification chain **b)** and second amplification chain as a function of the frequency between 4-8 GHz with additional 30 dB attenuation at room temperature.

By simple calculation, we can then determine the A_{in} as:

$$A(\nu_{in}) = \frac{\int \left(PSD(\nu) - PSD^{nosignal}\right) d\nu}{G_{ch}(\nu) P^{appl}} \tag{2.7}$$

Where P^{appl} is the signal applied on the top of the fridge. Figure (2.5.a) and figure (2.5.b) show the input attenuation respectively for the first and the second chain over the measurement frequency range 4-8 GHz.

Conclusion

The experiments described in this work have been performed in a Cryoconcept dry dilution refrigerator with a base temperature of 12 mK. We have presented the microwave equipement

used to measure our amplifiers and how we calibrate it. In the next chapter, we show how this experimental setup is used to measure the ICTA samples.

.

Chapter 3

First generation of the ICTA Samples based on Al superconductor

In this chapter, we present the first experimental proof that amplification close to the quantum limit is possible without microwave drive in an extremely simple setup [32]. As explained in the first chapter, our amplification scheme is based on inelastic Cooper pair tunneling where energy is provided by a DC voltage biased Josephson junction. In contrast to other microwave amplification schemes based on DC biased Josephson junctions [17, 16, 67] or conventional transistor or diode-based amplifiers, our scheme provides a well-defined idler mode which allows to reach near quantum limited noise performances in analogy to parametric amplifiers [37, 38, 15, 68].

We start this chapter by introducing the sample. Here, the measured device, fabricated in the Quantronics group in 2009, is based on an Aluminium (Al) Josephson junctions. We used this sample because its impedance is very close to the theoretical model presented in chapter (1). It is the first step to validate the principle of the ICTA. The measured PSD and reflection response as well as the input added noise are presented in the second section of this chapter. We also compare these quantities to the theory shown before.

In the last chapter, we present another experimental results based on NbN samples in which we try to optimize the performances of the ICTA according to the theoretical results shown in chapter (1) and the experimental results discussed here. Therefore, we call the sample based on Al junctions, presented in this chapter, the first generation of the ICTA and the samples based on NbN junctions, presented in chapter (6), the second generation of the ICTA.

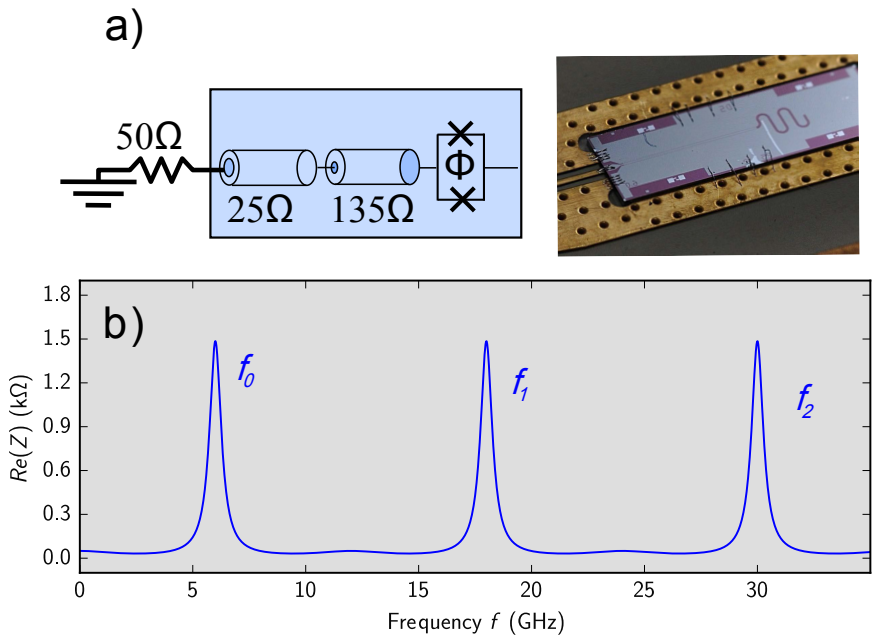

Figure 3.1 **Re Z(f): a)** Representation of the device: Two quarter wave resonators in series with characteristics impedance 25 Ω and 135 Ω, are coupled to an Al/AlO_x//Al SQUID with a maximum critical current I_c = 17.5 nA. These two transmission lines are designed for a resonance frequency of 6 GHz. **b)** The real part of the impedance Re Z(f) seen by the junction, calculated from the resonator geometry. Re Z(f) shows peaks at f_n = (2n+1)6 GHz; n= 0,1,2..

3.1 Sample parameters

The device is the same as in reference [31]. An Al/AlO_x/Al SQUID acts as a flux-tunable Josephson junction with a maximum critical current I_c = 17.5 nA. It is connected to a 50 Ω transmission line via a quarter-wave transformer with characteristic impedances respectively, 25 Ω and 135 Ω. These transmission lines are fabricated from niobium (Nb). The schematic of the sample is presented in figure (3.1). Figure (3.1) also displays the impedance $Z(f)$ seen by the SQUID as a function of the frequency. Z(f) presents peaks at $f_n = (2n+1)$ 6 GHz with widths of approximately 514 MHz.

We cool down the device to 12 mK in a dilution refrigerator and we measure its microwave noise emission as well as its microwave reflection. A DC voltage is applied through a 50 Ω bias circuit and a resonance-free bias-tee. Microwave reflection and noise are measured via cold circulators and amplifiers using a commercial vector network analyzer

(VNA) and a custom spectrum analyzer (SA) setup. The full setup is described in the previous chapter and the detailed schematic is presented in figure (2.3).

3.2 Experimental results

3.2.1 Power spectral density of the emitted radiation

In figure (3.2.a) we show the power spectral density emitted by the sample as a function of the frequency f and the applied voltage bias V, expressed in terms of the Josephson frequency $\nu_J = 2eV/h = \nu_J$. This PSD is qualitatively explained within the $P(E)$ framework as explained in the first chapter. All features in figure (3.2.a) appear around $f = 6$ GHz where $ReZ(f)$, the pre-factor in equation (1.43), is the largest. Their position in bias ν_J correspond to areas where the first term in equation (1.43) becomes large. Along the most prominent line, $\nu_J = f$, the argument of the first term is close to zero, i.e. the emitted photon absorbs all the energy of the tunneling Cooper pair and the Cooper pair can then tunnel easily, so that γ (equation (1.43)) becomes large. The lines at $\nu_J = f + f_{0,1}$ correspond to two photon processes where the detected photon is emitted at frequency f and another one is emitted in the mode $f_0 = 6$ GHz or $f_1 = 18$ GHz where emission is easiest and leads to the largest Cooper pair tunneling rate. Figure (3.2.b) shows the simulation of the same quantity by using the $P(E)$ theory (see section (1.3)).

3.2.2 Reflection coefficient measurement

In figure (3.3.a) we show the microwave reflection response as a function of the signal frequency f and the Josephson frequency ν_J. This figure indeed reveals strong gain, up to a factor 10 in power, in the areas where we have observed photon emission due to two-photon processes, meaning that the device can indeed provide amplification as expected. Figure (3.3.a) also shows lines of opposite slope where the device absorbs photons at the signal frequency even though we expect our device to be essentially dissipationless. These lines can be attributed to conversion processes where an incoming photon at frequency f is converted into a photon at frequency $f + \nu_J$ or $f - \nu_J$ which is not detected by our VNA. These two-photon processes have the same matrix element as the down-conversion processes but require an incoming photon at frequency f to be present. The absence of these lines shows that the electromagnetic environment of the device is indeed sufficiently cold to not send any thermal photons at f onto the device.

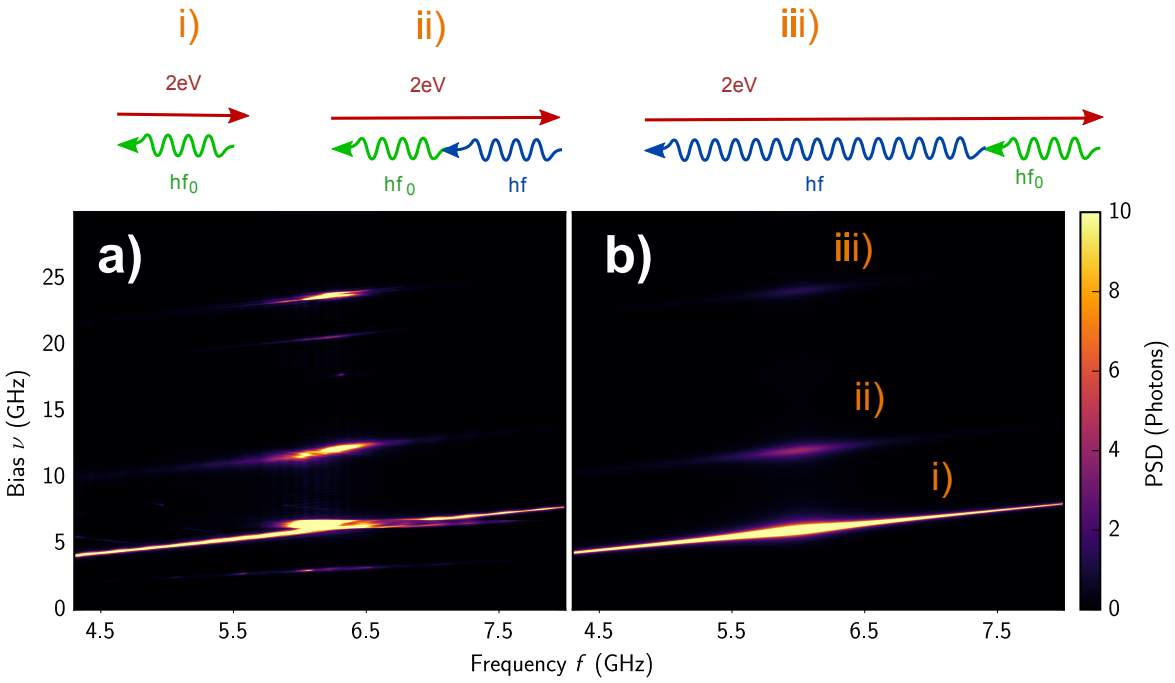

Figure 3.2 **Noise PSD: a)** The power spectral density as function of Josephson frequency ν_J and frequency f. The line at $\nu_J = f$ corresponds to emission of one photon per Cooper pair. Lines at $\nu_J = f + 6$ GHz and $\nu_J = f + 18$ GHz correspond to two photons emission processes with one photon emitted at frequency f and the other in the resonator modes at 6 and 18 GHz. **b)** The same quantity calculated from P(E) theory with the designed resonator impedance an effective temperature of 54.7 mK and $I_c = 20.2$ nA

We also explain these two phenomena by the equations (1.14) and (1.16) presented in the chapter (1). In fact, the conversion process with power gain -the amplification- (orange lines) corresponds to the first term $a^\dagger b^\dagger e^{-i\omega_J t}$ in the Hamiltonian (1.14), where $\omega_J = 2\pi\nu_J$. $a^\dagger$ is the creation quantum operator of a first photon at frequency f (signal mode). $b^\dagger$ is the creation quantum operator of a second photon at frequency $\nu_J - f$ (idler mode). By the same way, the conversion process without power gain -noiseless frequency conversion-(blue lines) corresponds to the term $ab^\dagger e^{-i\omega_J t}$ in the Hamiltonian (1.16). a is the annihilation quantum operator of one photon at frequency f. $b^\dagger$, is the creation quantum operator of a second photon at frequency $f + \nu_J$.

Along the line $\nu_J = f$ both gain, at $\nu_J \gtrapprox f$, and absorption, at $\nu_J \lessapprox f$, are visible. The gain is explained by parametric down-conversion with one photon at f and photons at very low frequency. The absorption process transforms a photon at f into a low frequency photon by tunneling a Cooper pair against the bias-voltage. Because of the reverse tunneling, this absorption line, unlike the others, has a positive slope.
Within standard theory of inelastic charge tunneling, a.k.a. the P(E) theory, these amplification processes explained by the effective admittance of the junction at frequency f (equation (1.46)). Probabilities for a photon inpinging on the junction to be absorbed are described by γ^-. Probabilities for a photon being reflected while emitted an additional photon, by stimulated emission, are described by γ^+ (see section (1.3)).

3.2.3 Comparison between measurements and simulations

In figure (3.2.b) and (3.3.b), we plot the theoretical predictions for the photon spectral density and the gain based on equation (1.43) and (1.46). They qualitatively describe our experimental findings and correctly describe the areas where we observe gain and loss. The only fiting parameter is the Josephson energy E_J. Note however, that equation (1.43) and (1.46), based on the standard P(E) theory, are strictly valid only at a very low critical current and for $\gamma \ll 1$, where tunneling events are so rare that the electromagnetic modes in the circuit relax to their ground states between each tunneling event. This regime has been explored in the same sample by tuning the SQUID to a low effective critical current [31]. Here, on the contrary, we use the SQUID at its maximum critical current, where the Cooper pair current is large enough to drive the electromagnetic modes at f_0 and f_1 significantly out of equilibrium, as can be seen in figure (3.2.a) where we observe photon numbers well beyond 1. This is indeed necessary: in order to reach $|G| \ll 1$ we require Z(f)Y(ν_J,f)$\rightarrow -1_+$, i.e. we need to violate the condition $\gamma \ll 1$ in order to obtain useful gain.

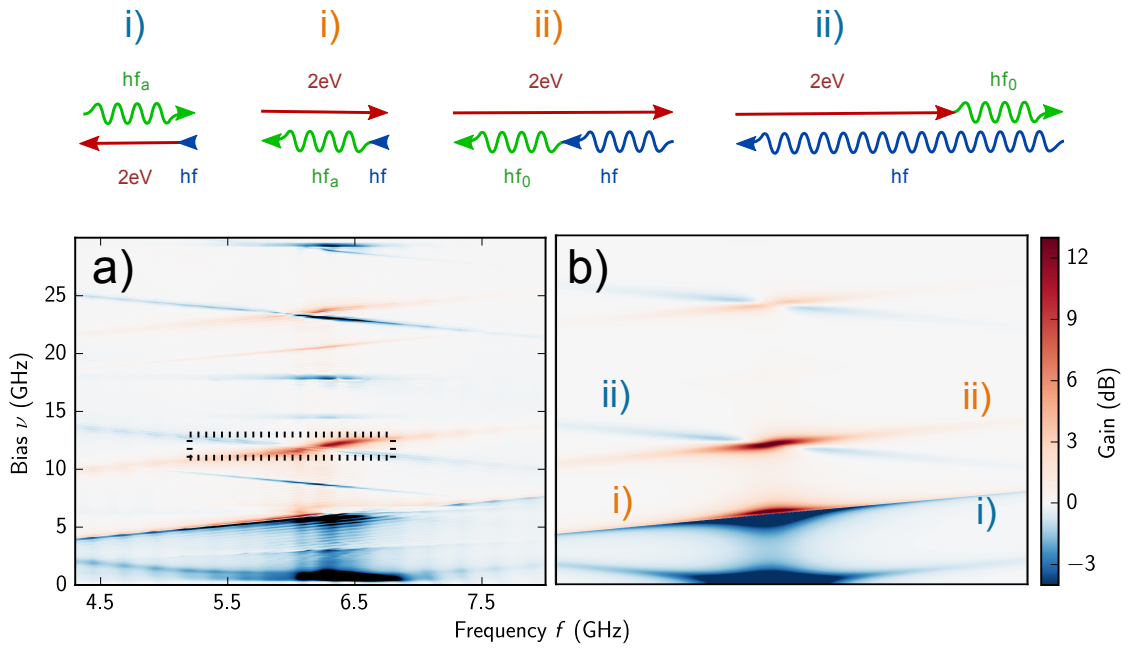

Figure 3.3 **Gain of the ICTA: a)** The gain of the ICTA measured with an input power of P_{in} = -117 dBm as a function of ν_J and f. Red areas correspond to down-conversion processes with gain (amplification) and blue lines to frequency conversion processes observed as loss. **b)** The same quantity calculated from the P(E) theory with the designed resonator impedance, an effective temperature of 54.7 mK and I_c = 20.2 nA

In fact, the nominal critical current is evaluated to 17.5 nA from prior measurements of the normal state resistance at 4K and an estimated gap of 2Δ= 0.2 meV of our aluminium junction using the Ambegaokar-Baratoff formula. The agreement with the critical current 20.2 nA obtained from fitting the gain signature is remarkably good knowing that we operate in a regime where equation (1.43) is not strictly valid. Therefore, equations (1.43) and (1.46) only give a qualitative description of amplification and noise but not a fully quantitative one. A quantitative description calls for an extension of the P(E) framework.

The key question: do the ICTA work close to the quantum limit?

3.2.4 Noise measurement

To answer the last question, we calculate the ICTA input added noise by dividing the output noise by the gain, taking into account the zero-point fluctuations of the incoming line. This output noise is measured as the difference between the noise emitted at bias ν_J and at bias 0. It measures photon emission, i.e. it removes noise added by the amplification channel and the zero point fluctuations. We therefore calculate the noise added by the sample as:

$$n_{in} = \frac{n_{out} + \frac{1}{2}}{|G|} - \frac{1}{2} = \frac{n_{out}}{|G|} - \frac{1}{2}\left(1 - \frac{1}{|G|}\right) \tag{3.1}$$

In figure (3.4), we plot the gain and the input noise at ν_J = 12.44 GHz and 12.17 GHz where the down conversion process with two photons near f_0 and the up-conversion process from f_0 to f_1 play a role. We observe, respectively, gain of approximately 8.5 dB and 11.7 dB over a bandwidth of 297 MHz and 171 MHz and an input added noise of approximately 0.9 photon and 1.9 photon. At ν_J = 12.44 GHz, the input added noise indeed corresponds to less than twice the quantum limit. This value is lower than existing DC powered amplifiers mentioned in the introduction of this thesis, but higher than the best Josephson parametric amplifiers [37, 15]. The most obvious reasons for this slight excess noise are losses in the circuit and thermal photons in the signal and idler modes. However, losses in the circuit are calibrated out (see chapter (2)) and we expect the modes at f_0 and f_1 to be in their thermal ground states because if they were not, we expect noise signatures in figure (3.2) corresponding to de-amplification lines in figure (3.3).

We instead attribute the excess photon noise to low frequency voltage fluctuations. If the width of these low frequency fluctuations is much smaller than the bandwidth of the amplifier, the idler signal adiabatically follows the fluctuations in the pump frequency without

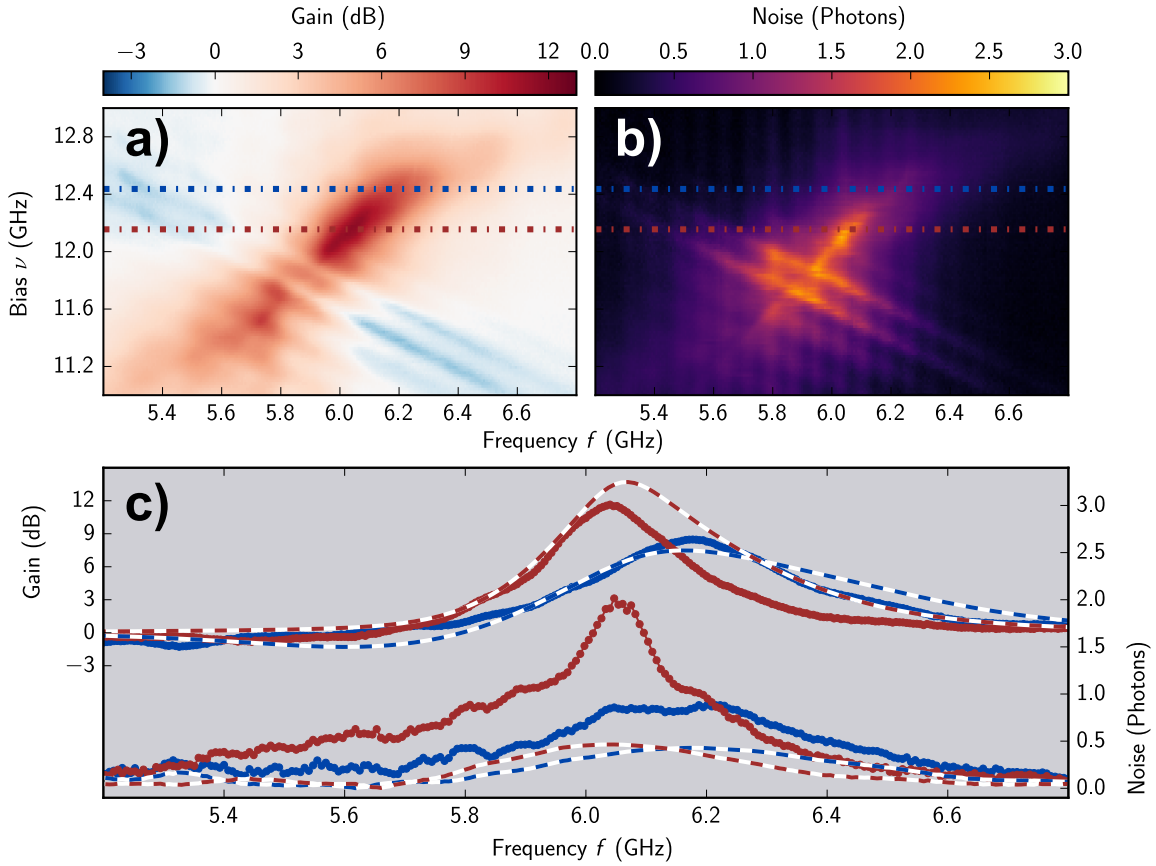

Figure 3.4 **Gain and noise performances: a)** Same data as in Figure (3a), focused on the two photons processes at ν_J=12 GHz. **a)** Added noise of the ICTA, i.e. the output noise power divided by the gain, taking into account zero-point fluctuations of the input mode. **c)** Cut at ν_J= 12.17 GHz (dark colors) and 12.44 GHz (light colors). The dashed blue lines are calculated from equation (3) using nominal sample parameters, an effective temperature 54.7 mK and I_c = 20.2 nA. Dashed red/orange lines represent the quantum limit on added noise for the measured gain.

affecting the gain or the phase in the signal mode. On the other hand if the fluctuations of the Josephson frequency excess the bandwidth of the amplifier, these fluctuations bring the amplifier out of its optimal working conditions, reducing its gain and altering its phase response. Therefore, such large voltage fluctuations, therefore, lead to phase noise of the amplified signal. In phase-sensitive VNA measurement (IF bandwidth 1 kHz), they lead to reduced gain. However, they do not reduce the photon noise measured by the PSD. And so, the input added noise, i.e. the ratio of the photon noise over the gain, is degraded. In our setup we achieve an effective temperature of the low frequency electromagnetic environment of approximately 55 mK corresponding to ν_J = 120 MHz. This width is only slightly smaller than the bandwidth at ν_J = 12.44 GHz and we, therefore, attribute the slight excess noise to fluctuations in the bias voltage. At ν_J = 12.17 GHz the voltage fluctuations and the bandwidth are approximately equal and we observe a much higher excess noise, in agreement with our explanation. This source of phase noise is essentially absent in JPAs where the role of the ICTA voltage bias is taken by the microwave pump tone, which has a negligible phase noise. Therefore JPAs perform better at narrow bandwidths but we expect ICTAs to become competitive at larger bandwidths where the voltage bias can be filtered sufficiently to not degrade performance. We discuss this optimization in the last chapter.

3.2.5 Behaviour at high input power

In figure (3.5), we show the microwave response of the device at high power. In addition to the lines at $\nu_J = f$, distinctive lines appear at $\nu_J = \mathrm{n}f$ with integers n > 1 and globally the gain is much lower. These lines correspond to processes that are nonlinear in the signal amplitude, i.e. involving more than one signal photon. These are the terms which we have neglected in order to derive equations (1.14) and (1.16). Treating the input signal classically, one easily see that these lines scale (white lines presented in figure (3.5)) with $J_n^2(2eV_{0s} = hf)$ as we explained before (section (1.3)). Where J_n is the n-th order Bessel function and V_{0s} the peak amplitude of the signal.
The amplifier is linear in the signal amplitude as long as the argument of the Bessel function is $\ll 1$. This corresponds to an output power:

$$P_{out} \ll \frac{R_Q}{ReZ(f)} hf^2 \tag{3.2}$$

Another constraint is that the signal current is limited by the critical current of the junction. When the critical current of the junction is adjusted to lead to a large gain, this constraint leads to a similar condition as (3.2) but on the idler frequency i.e. with f replaced by ν_J - f.

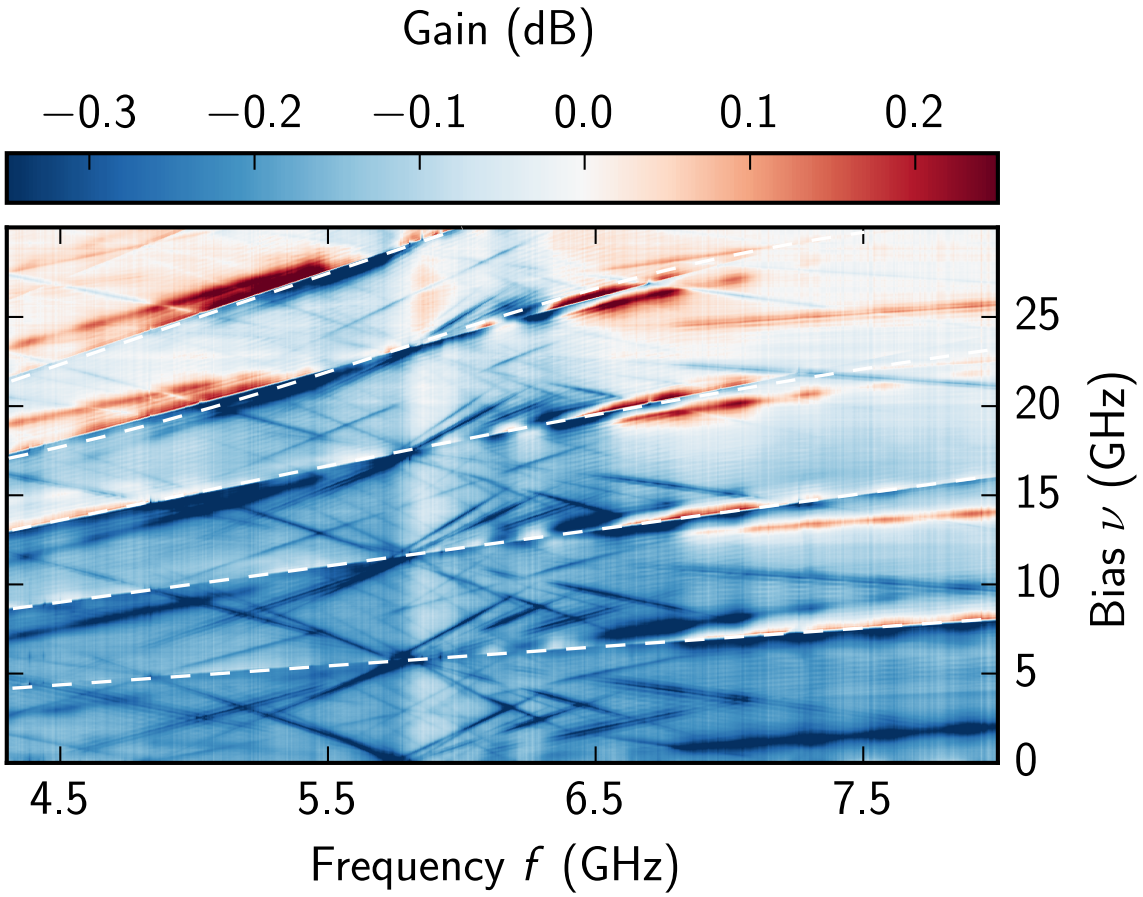

Figure 3.5 **Response at high power:** Gain measured at maximum Josephson energy as a function of the Josephson frequency and the signal frequency for an input power of P_{in} = -82 dBm. Overall gain is strongly compressed and new features appear at $\nu_J = kf + mf_i$ where f_n are the modes of the resonator and k, m integers, corresponding to nonlinear processes involving many signal and idler photons.

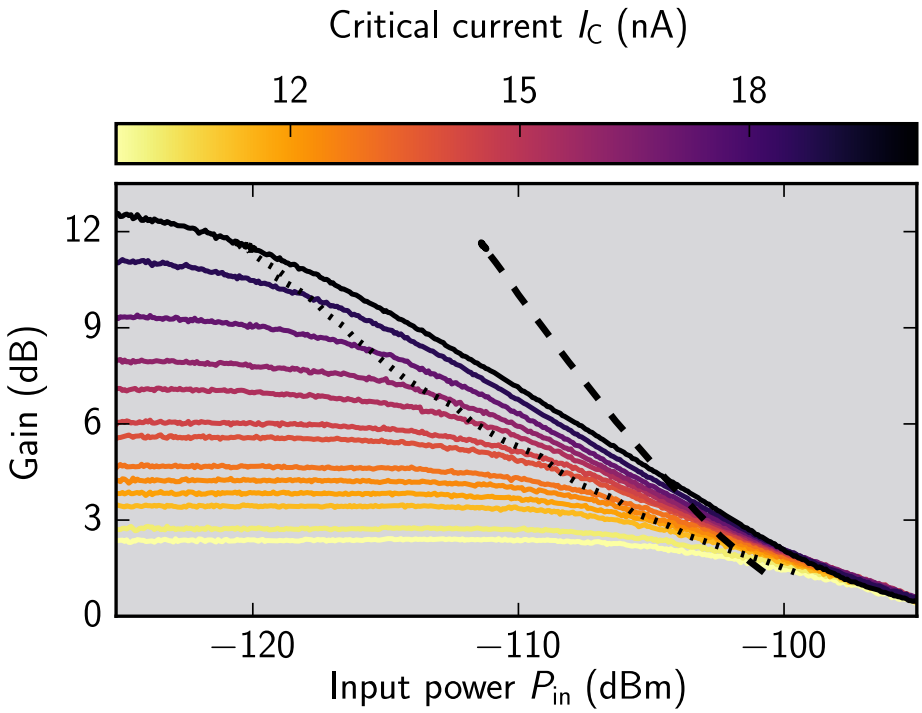

Figure 3.6 **Dynamic range:** Gain as a function of the input power P_{in} for different Josephson energies at ν_J = 12.15 GHz and f = 6.05 GHz. The dotted line represents the input 1 dB compression points.

These additional lines give the high order terms of the down-conversion process.

We now address the incidence of these higher order terms on the dynamic range.

3.2.6 Dynamic range measurement

In figure (3.7), we show gain compression as a function of the input power. At the maximum gain, when the voltage bias is ν_J = 12.15 GHz, the input power at 1 dB gain compression is approximately -117 dBm. In order to optimize the dynamic range of this kind of amplifiers it is therefore important to integrate the amplifier in a circuit of relatively low impedance (see the next chapter). However, the impedance at the signal frequency f and at the idler frequency ν_J - f have to remain high enough to avoid parasitic parametric oscillations at other frequency pairs before sufficient gain can be reached. An example of such parasitic parametric oscillation is presented below:

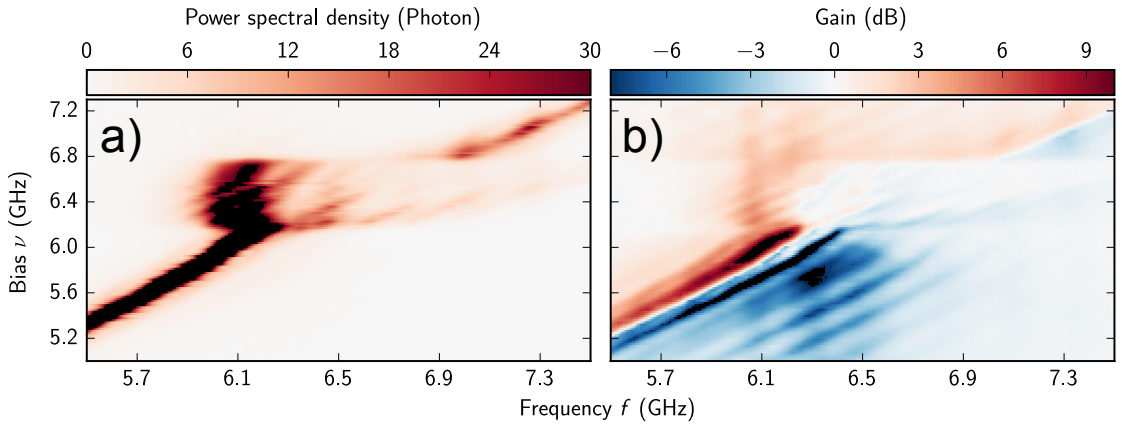

Figure 3.7 **Parametric oscillation: a),b)** Same data as shown respectively in figure (3.2) and figure (3.3), focused on the one photon processes at $\nu_J = 6$ GHz.

3.2.7 Parametric oscillation

Two kinds of saturation can be identified in parametric amplification physics: the dynamic range and the parasitic parametric oscillation. We discussed, in the previous paragraph, the ICTA dynamic range, now, we focus on the parametric oscillation phenomenon. In figure (3.7.a) and (3.7.b) we show, respectively, the power spectral density PSD and the ICTA gain focussed on the one photon process at $\nu_J \gtrapprox \mathrm{f} \approx 6$ GHz. We can identify on both of these figures some irregularities around 6 GHz due to parametric oscillation of ≈ 35 MHz. In fact, the impedance seen by the Josephson junction is not just the impedance given by the device but in reality the impedance given by all the electromagnetic environment. Then it is possible to have some parasitic peaks in $\mathrm{Z}(f)$ corresponding to frequencies resonance of the electronic devices (in this case the bias-tee). If this peak has very small width (easy at low frequency), the ICTA gain diverges, $\mathrm{G} \to \infty$ according to the equation (1.34) shown in the chapter (1). The parametric oscillation is a phenomenon identified in JPA physics, it come from the compromise between the Josephson energy E_J and the microwave pump power P_{pump}. An analogue physics takes place in ICTA case, we have a compromise between the Josephson energy E_J and $\mathrm{Z}/\gamma = f/Q$.

3.3 Summary and points to optimize

In conclusion, our results experimentally show that inelastic Cooper pair tunneling through a small Josephson junction can lead to near quantum limited amplification despite the fact that the applied bias voltage is always noisy. The measured performances of the first generation

Table 3.1 Performance of the first generation of the ICTA.

Gain (dB)	10
Bandwidth (MHz)	284
Noise (photon)	0.9
Dynamic range (dBm)	-114

of the ICTA is summarized in the table (3.1). By designing an appropriate linear matching circuit, characterized by its impedance Z(f) as seen by the Josephson junction we expect that practically useful ICTAs can be built. Therefore, we design new samples based on niobium nitride (NbN) junctions (the second generation of the ICTA), in which we try to optimize the following points:

- **Increase the E_J:** The ICTA gain scales with the Josephson energy E_J (equation (1.34)). One of many ways to control E_J is by using a SQUID (see the next chapter). We therefore design a new samples using a SQUID with large Josephson junctions.

- **Eliminate frequency conversion processes:** A near quantum limited parametric amplifier should work only with the amplification term ($a^\dagger b^\dagger c$) and avoid the down-conversion terms ($ab^\dagger c$, $a^\dagger bc$). As can be seen in figure (3.4.b), the added noise of ICTA is higher at the crossing of amplification and conversion lines. In order to reduce this effect, we design new samples with particular impedance shapes such that the term $ab^\dagger e^{-i\omega_J t}$ is suppressed (see next chapter).

- **Reduce sensitivity to voltage noise:** In order to increase the ICTA bandwidth and to reduce the noise, we propose to lower the resonator quality factor. Actually, any fluctuations coming from the voltage bias also results in fluctuations on the idler mode. This can increase the ICTA noise. To resolve this issue, we increase γ in order to be sure that the idler is always on resonance. Otherwise, the ICTA gain shifts and the added noise phase of the signal is important.

- **Reduce voltage noise:** In order to reduce the voltage noise, we integrate on chip filters to reduce impedance at low frequencies.

- **Fix the idler mode at high frequencies:** As seen before, the second generation samples of the ICTA are fabricated with niobium nitride (NbN) superconductor. One of many advantages of this superconductor is its large gap $\approx$ 1.2 THz. This gives the opportunity to fix the idler mode at high frequencies in order to reduce the thermal noise.

Here, we conclude measurements on the first generation of the ICTA samples based on Al junctions. In the remainder of this thesis (design, fabrication and experimental results), we will focus on the second generation of ICTA samples based on NbN circuits.

Chapter 4

Design of ICTAs

In the previous chapter, we have presented microwave reflection measurements on the device based on aluminium junctions indicating that amplification is possible with a simple DC voltage-biased Josephson junction. We have also shown that this amplification adds noise close to the limit set by quantum mechanics for phase preserving amplifiers [10]. Combined with the theoretical model presented in chapter (1), our results indicate that voltage-biased Josephson junctions might be useful for amplification near the quantum limit, being powered by a simple DC voltage and providing a different trade-off between the gain, bandwidth and the dynamic range, which could be advantageous in some situations.

In this chapter, we propose different designs in order to optimize the various performances of ICTAs: low noise, large bandwidth, high dynamic range and high gain. In this work, we choose niobium nitride as a superconductor. This is of particular interest for us, because with NbN based samples, where $2\Delta/h \cong 1.2$ THz, it is possible to fix the idler mode at a high frequency which help to reduce the thermal noise in this mode. We present the different steps of the sample fabrication in the next chapter. Here, we give a detailed overview of the ICTA sample design. Recently, we filed a patent application for some aspects of these designs [33]. First, we start this chapter by presenting various considerations that we have taken into account to design the SQUID and the CPW. Then, the two main sample-types, reflection and transmission amplifier, are discussed (see figure (4.1)). For reflection amplifier, we put forward a special circuit to enhance each characteristic of ICTA independently. We finish the chapter by giving some perspectives for a new design able to combine all these characteristics simultaneously.

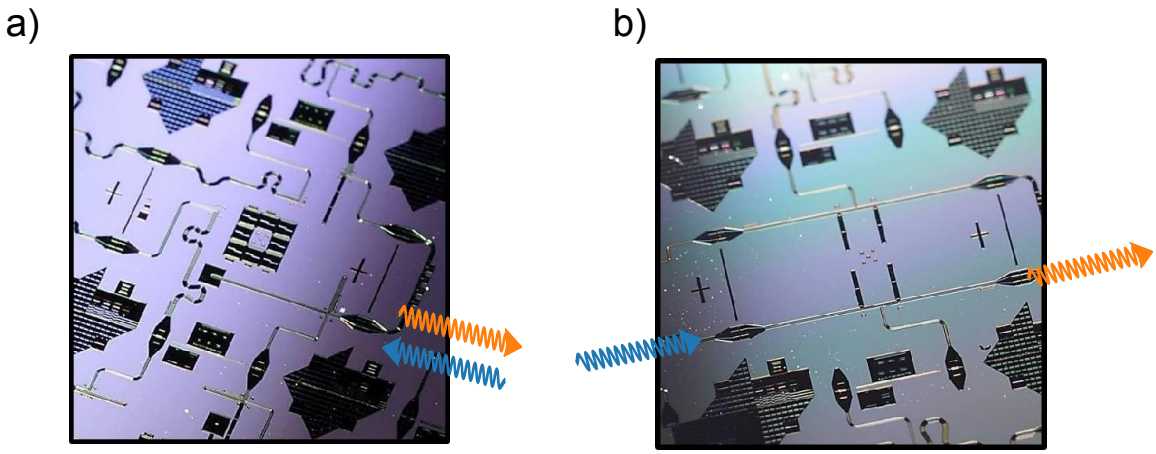

Figure 4.1 **Photograph of two entire chips: a)** includes four types of reflection amplifiers. **b)** includes the transmission amplifier.

4.1 Basic elements of the ICTA design

4.1.1 SQUID design

Josephson junctions are the most important building blocks for superconducting devices. Especially in parametric amplifier physics, they play a very important role because they act as non-dissipative elements able to couple the pump, signal and the idler. A Josephson junction consists of two superconducting contacts separated by a thin insulating layer. The current flowing through the junction by the Josephson relation is defined as:

$$I = I_c sin(\varphi) \tag{4.1}$$

$\varphi = \phi_2 - \phi_1$ is the phase difference of the wave functions (ϕ_1, ϕ_2) on each side of the junction. I_c is the critical current. The energy stored in the junction, called the Josephson energy, is describe through the Josephson Hamiltonian as:

$$H_J = E_{J_0} cos(\phi) \tag{4.2}$$

Where,

$$E_{J_0} = \frac{\hbar I_c}{2e} \tag{4.3}$$

In this work, we use a superconducting quantum interference device (SQUID) which consist of a superconducting loop interrupted by two Josephson junctions. The advantage of the SQUID geometry is that we control the effective Josephson energy E_J thanks to a

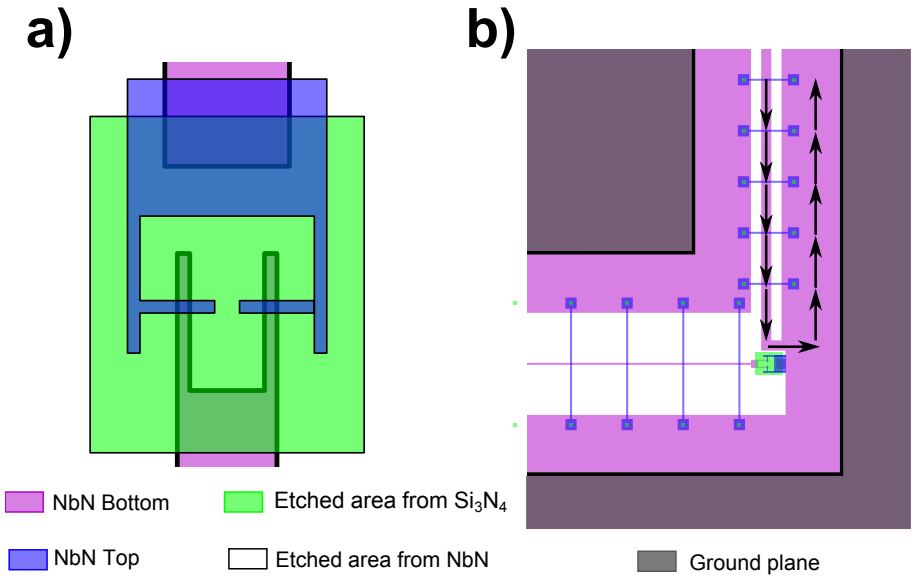

Figure 4.2 **Representation of SQUID : a)** The SQUID and the flux bias line. The black arrows indicate the circulation of the current in the bias line. **b)** Representation of SQUID. The violet structure indicates the trilayer. The green regions indicate where we etch the Si_3N_4. The blue structures indicate the top-wiring. More details on the fabrication of our samples follow in the next chapter.

magnetic flux Φ,

$$E_J = 2E_{J_0}|cos(\pi\frac{\Phi}{\Phi_0})| \tag{4.4}$$

E_{J_0} is the Josephson energy of a single junction. $\Phi_0 = h/2e = 2.10^{-5}$ Wb is the superconducting flux quantum. This is the key of our method to control the gain of ICTA. In fact, as explained in section (1.2), the gain of ICTA increases with the Josephson junction energy. Then, we can control the ICTA gain by modulation of the critical current. In this thesis, the SQUID is treated as a Josephson junction with flux-tunable critical current.

Figure (4.2) illustrates the layout of our SQUID on the left and shows the superconducting flux line surrounding the SQUID on the right. The flux line is connected, at one end to a 50 Ω matched transmission line acting as a current source, and at the other end to the ground plane of the chip. A current flowing through this line creates a magnetic field through the loop of the SQUID. The flux-bias line can be roughly approximate as a straight line. The calculated area of our SQUID is $208\mu m^2$. According to the Biot-Savart law, the magnetic field, in this case, is defined by $B = \frac{\mu_0 I}{2\pi d}$ with μ_0 is the permeability of free space and d is the length of

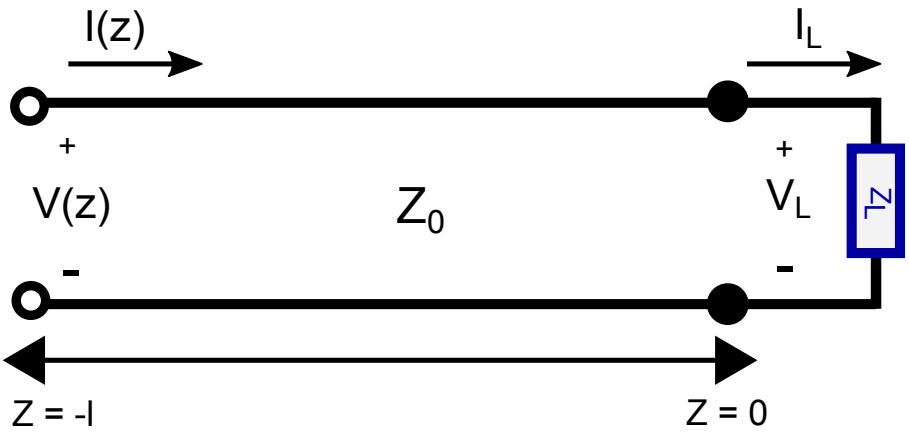

Figure 4.3 **Transmission lines:** Transmission line with a characteristic impedance Z_0 and length l terminated by a load impedance Z_L

the straight line from the flux line to the center of SQUID. Then, we can estimate that the current necessary to sweep one flux-quantum through the loop is $I_{\Phi_0} = \frac{2\pi d\Phi_0}{A\mu_0} \approx 1$ mA.

4.1.2 CPW resonator design

In this section, we review how the coplanar wave-guides are combined to give the needed impedance in order to realize a good amplifier. First, we summarize some import basic proprieties of terminated transmission lines. Then we introduce the specific case of a $\lambda/4$ microwave resonator and a $\lambda/2$ microwave resonator. The discussion of these cases is important in order to understand the design of our samples. We consider a lossless line, with length l, terminated with a load Z_L, as can be seen in figure (4.3) [69]. The input impedance seen at the beginning (z = -l) of the transmission line is defined by :

$$Z_{in} = Z(z = -l) = \frac{V(z = -l)}{I(z = -l)} \tag{4.5}$$

The total voltage can be decomposed in incident (V^+) and reflected (V^-) waves:

$$V(z = -l) = V^+(z = -l) + V^-(z = -l) \tag{4.6}$$

$V^+(z = -l) = V_0^+ e^{-j\beta l}$, $V^-(z = -l) = V_0^- e^{+j\beta l}$ and $\Gamma(z) = \frac{V_0^-}{V_0^+}$ which is the reflection coefficient. β is the propagation constant. We can determine now exactly the voltage and the

current at the beginning of the transmission line as a function of V_0^+ and Γ_L [70]

$$V(z=-l) = V_0^+ \left[e^{+j\beta l} + \Gamma_L e^{-j\beta l} \right] \tag{4.7}$$

$$I(z=-l) = \frac{V_0^+}{Z_0} \left[e^{+j\beta l} - \Gamma_L e^{-j\beta l} \right] \tag{4.8}$$

Therefore,

$$Z_{in} = \frac{V(z=-l)}{I(z=-l)} = Z_0 \left\{ \frac{e^{+j\beta l} + \Gamma_L e^{-j\beta l}}{e^{+j\beta l} - \Gamma_L e^{-j\beta l}} \right\} \tag{4.9}$$

We can also write the Z_{in} in terms of the load impedance Z_L by using the expression of the reflection coefficient Γ_L defined by,

$$\Gamma_L = \frac{Z_0 - Z_L}{Z_0 + Z_L} \tag{4.10}$$

Finally, we obtain a general formula of the input impedance of a transmission line as a function of the characteristic impedance Z_0, the load impedance Z_L, the propagation constant β and the length l [70]

$$Z_{in} = Z_0 \frac{Z_L + jZ_0 tan(\beta l)}{Z_0 + jZ_L tan(\beta l)} \tag{4.11}$$

Now, let's focus on some important special cases for different lengths of the transmission line [70]

Half wave resonator: If the length of the transmission line is exactly one-half wavelength $l = \frac{\lambda}{2}$, we find that the propagation constant $\beta l = \pi$. In this case, we can simplify the equation (4.11) to

$$Z_{in} = Z_L \tag{4.12}$$

That means that if the transmission line is precisely one-half wavelength long, the input impedance is equal to the load impedance, regardless of Z_0.

Quarter wave resonator: If the length of the transmission line is exactly one-quarter wavelength $l = \frac{\lambda}{4}$, we find that the propagation constant $\beta l = \frac{\pi}{4}$. In this case, we can simplify the equation (4.11) to

$$Z_{in} = \frac{Z_0^2}{Z_L} \tag{4.13}$$

That means that if the transmission line is precisely one-quarter wavelength long, the input impedance is inversely proportional to the load impedance. And here, we can distinguish between three important cases, when:

1. $Z_L = 0$**,** the quarter-wave transmission line transforms a short-circuit into an open-circuit.

2. $Z_L = \infty$**,** the quarter-wave transmission line transforms an open-circuit into a short-circuit.

3. $Z_L = Z_0$**,** the input impedance Z_{in} is equal to Z_0 regardless of transmission line length l and β.

Simulation used in this work: Simulating an entire ICTA circuit in a microwave simulator, such as Sonnet, is slow and therefore does not allow us to easily adjust design parameters. We rather use a simulator for linear circuits using idealized components which has been written in our group in python. It is based on the admittance matrix of the circuit and handles single or coupled transmission lines in addition to lumped elements. It allows us to calculate in less than $1\,s$ admittance, impedance and scattering matrices for our circuits. This decomposition in idealized components is valid because the lateral size of transmission lines and lumped elements used is much smaller than the wavelength and because we can neglect bends in transmission lines thanks to the ground-plane straps. Based on these simulations, we determine capacitance values, and the impedances and electrical lengths of transmission lines required for our circuits.

We then need to find how to implement such transmission lines using our fabrication process. To do so, we use a second simulation program developed in our group which calculates the properties of TEM modes in transmission lines with arbitrary number of conductors and dielectrics. Such a simulation is much faster than a full circuit simulation because, instead of a full 3D geometry, we perform the simulation along a 2D cut through the transmission line, which is invariant along the propagation direction. First, we calculate the capacitance per unit length C of the transmission line by calculating the charge distribution on metal surfaces and dielectric interfaces for a given voltage between conductors.

By calculating in addition the capacitance per unit length C_0 for the same geometry but with all relative dielectric constants set to 1 we can also calculate the effective dielectric constant $\varepsilon_{eff} = C/C_0$.

The geometric inductance is then

$$L_{geo} = \frac{\varepsilon_{eff}}{c^2 C} = \frac{1}{c^2 C_0}. \tag{4.14}$$

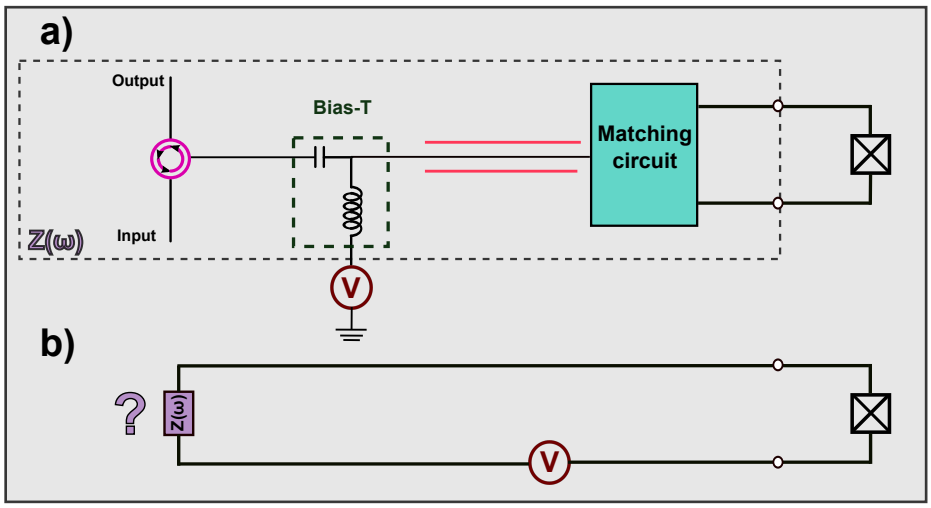

Figure 4.4 **A schematic circuit of an ICTA: a)** A Josephson junction is connected to a matching circuit. We use a Bias-T (green square) to apply the DC bias voltage. We need a circulator to separate the incoming and outgoing signals travelling on the same port (blue transmission line), in the case of reflection amplifier. **b)** The circuit presented in **a**) is seen by the Josephson junction as an impedance Z depending on the frequency ω.

In order to calculate the kinetic inductance we start from the surface charge density which we calculate at the same time as the capacitance matrix. We use the fact that for a TEM mode charge density is proportional to the surface current density J. The effective kinetic inductance per unit length L_{kin} can then be calculated as

$$L_{kin} = \frac{\oint L_{kin,\square} J^2 ds}{(\oint J ds)^2} = \frac{\oint L_{kin,\square} J^2 ds}{I^2}. \tag{4.15}$$

With the total inductance $L = L_{geo} + L_{kin}$ we can then calculate the propagation speed $v = \frac{1}{\sqrt{LC}}$ and the characteristic impedance $Z = \sqrt{\frac{L}{C}}$.

For multi-conductor transmission lines C and L are matrices and the propagation speeds and impedances have to be calculated for each eigenmode of the capacitance matrix.

We perform this simulation, which takes typically a few seconds, several times until we find the geometry required for the desired transmission line impedance.

We give here some general rules to respect in order to obtain a useful ICTA, they have given rise to a patent application [33].

4.2 General design considerations for ICTA

Figure (4.4) provides a simplified schematic of the ICTA: A Josephson junction is coupled to a matching circuit. We use a Bias-T to apply the voltage bias to the junction. For reflection amplifiers, we need a circulator to separate the ingoing signal and the outgoing amplified signal. This electromagnetic environment can be describe by an impedance Z(f), giving the linear voltage response in the circuit to current fluctuations at the junction as a function of the frequency f. The key of ICTA design is to design a matching circuit resulting in a special form of impedance seen by junction allowing, mainly, to reduce as much as possible the added noise by the ICTA and to increase the bandwidth. This is the case if the real part of the impedance Z(f) satisfies the following conditions:

- **Re** $Z(f_s) > \mathbf{0}$ and **Re** $Z(f_i) > \mathbf{0}$**:** In order to have the resonance condition $2e$V = f_s + f_i, the real part of the impedance should present two resonances at the frequencies f_s and f_i corresponding, respectively, to the signal and idler modes. In addition, as shown in the first chapter of this thesis, the ICTA gain is proportional to the characteristic impedances Z_a and Z_b of both modes. As this rule is necessary to amplify the signals.

- **Re** $Z(f=0) < \dfrac{h}{4e^2}\dfrac{\nu_J}{GxBW}$**:** G and BW are respectively the gain and the bandwidth of the ICTA. In the second chapter of this thesis, we have shown that the ICTA noise is sensitive to low frequency voltage fluctuations. We also know, thanks to the measurements presented in the same chapter, that if the width of these low frequency fluctuations is much smaller than the bandwidth of the amplifier, the idler signal follows the fluctuations of the pump frequency without affecting the ICTA gain. Otherwise, these fluctuations bring the amplifier out of its optimal working point. Therefore, the ICTA asks a good filtering at low frequencies. This inequality imposes that the real part of the impedance seen by the junction should be very small at low frequency in order to avoid strong parametric oscillation involving low frequency photons and photons close to ν_J, in other words they assert a stable working point.

- **Re**$(Z(\nu_J + f_s)) < \dfrac{\nu_J + f_s}{f_i}$ **Re**$(Z(f_i))$**:** As can be seen in chapter (1), the circuit studied in this work can operate with two modes: Amplification and frequency conversion. However, in the previous chapter, we have shown that the presence of these frequency-conversion process adds noise. In order to reduce this effect, we propose through this inequality to reduce the impedance seen by the junction at frequencies $\nu_J + f_s$ and $\nu_J + f_i$. More specifically, this condition allows to eliminate the conversion of the energy of a tunnelling Cooper pair plus the energy of a signal photon to the energy of a idler photon, or vice versa.

- $f_i > \frac{k_B T}{h}$**:** As explained before, we amplify the signal photons by generating idler photons according to the relation $2e\text{V} = hf_s + hf_i$. The roles of the signal and the idler are completely symmetric. Therefore, any thermal photons in the idler mode can be amplified and reflected to the signal mode. To resolve this matter, we designed one sample in which we fix the idler mode at high frequencies in order to be in its quantum ground state.

- $BW > \Delta\nu_J$**:** It means that the bandwidth of the amplifier should be larger than the low frequency voltage noise, so that the idler adiabatically follows voltage fluctuations. We then expect that the amplifier reaches the quantum limit.

In the remainder of this chapter, we present various circuits taking into account these conditions. We start by describing the standard model of non-degenerate reflection amplifiers in which the signal and the idler modes are separated. Then, we introduce three designs for reflection amplifiers in which the idler mode is not spatially separated from the signal mode: The first and the second samples are designed in order to optimize the ICTA bandwidth. The third sample is designed to reduced the ICTA noise. We propose also, a new design for transmission amplifiers, discussed subsequently.

4.3 Reflection amplifiers

In this section, we discuss the reflection-type amplifier in which the separation between the input signal and the output signal is accomplished by a circulator.
Reflection amplifiers in a microwave circuit yield a power gain $\text{G} = \frac{P_{out}}{P_{in}} = |S_{11}(\omega)|^2 = |\Gamma(\omega)|^2$. $\Gamma(\omega)$ is the reflection coefficient as a function of the frequency of a transmission line terminated by a load impedance Z_L defined by equation (4.10) (see figure 4.3.a). When $|\Gamma(\omega)| = 1$, no amplification is produced at the signal frequency f_s; only a de-phasing is established. However, when the load impedance Z_L is equal to Z_0 the power gain diverges. This negative load impedance Z_L can be presented by the Josephson junction, thanks to its dynamic negative resistance [71, 72].

4.3.1 Reflection amplifiers with two separate modes

In this work, we focus only on non-degenerate amplifiers. In fact, the degenerate amplifier requires of precise control of the phase of the pump (section (1.1.3). In our case, as explained before, the phase depends on the DC voltage according to equation (1.8). There-

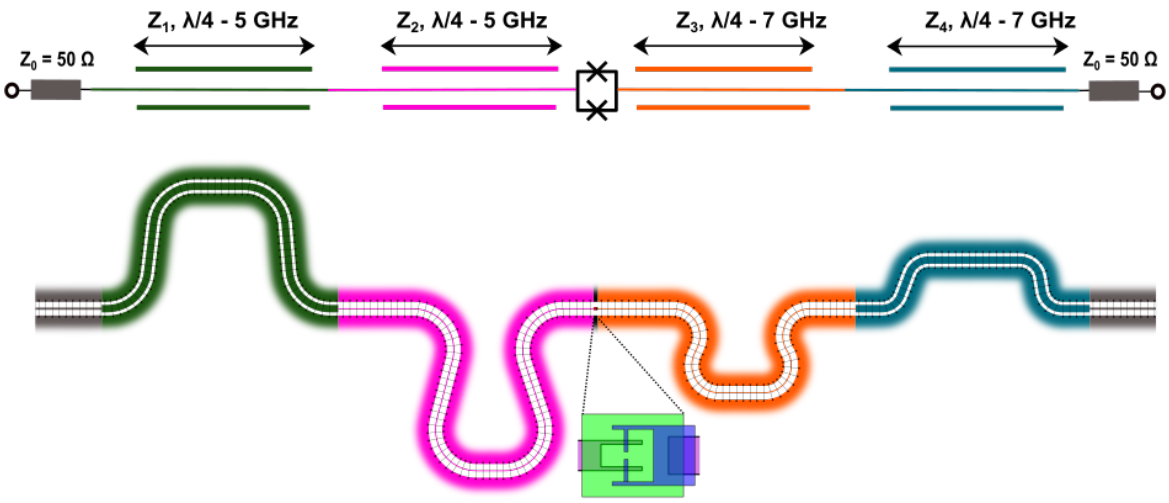

Figure 4.5 **"Canonical" non-degenerate amplifier with two separate modes** (S_1)**:** For better visibility the color scheme is chosen differently than in the rest of this work. we associate one color for each quarter-wave resonator to show the coupling between the resonators. The green and the fuchsia resonators, together, form the signal mode at 5 GHZ. The orange and the blue resonators, together, form the idler mode at 7 GHz. A zoom on the entire SQUID is located in the bottom of the image. For the SQUID, we kept the same color than the rest of this work. The violet color indicates the trilayer, the blue color indicates the NbN Top wiring and finally the green color indicates the area where we etch the Si_3N_4 dielectric. Table 4.1 indicates values of the four quarter-wave segments we have implemented.

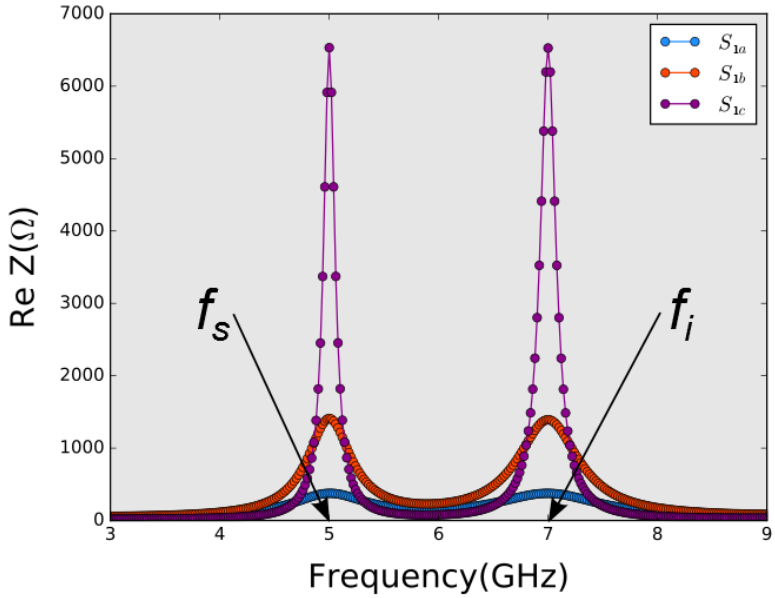

Figure 4.6 **Real part of the impedance seen by the SQUID as a function of the frequency f for "canonical" non-degenerate amplifiers:** Blue line: Re $Z(f)$ for S_{1a} implementation, where we have large resonances over 1 GHz frequency range. Red line: Re $Z(f)$ for S_{1b} implementation, where we have resonance over 500 MHz frequency range. Violet line: Re $Z(f)$ for S_{1c} implementation, where we have resonance over 100 MHz frequency range. The three curves show two peaks, the first one for the signal mode at 5 GHz and the second one for the idler mode at 7 GHz.

Table 4.1 Parameters of the sample S_1 for reflection amplifier with two separate modes model.

S_1	$Z(\Omega)$	f (GHz)
S_{1a}	$Z_1 = 23$	$f_1 = 5$
	$Z_2 = 60$	$f_2 = 5$
	$Z_3 = 60$	$f_3 = 7$
	$Z_4 = 23$	$f_4 = 7$
S_{1b}	$Z_1 = 23$	$f_1 = 5$
	$Z_2 = 120$	$f_2 = 5$
	$Z_3 = 120$	$f_3 = 7$
	$Z_4 = 23$	$f_4 = 7$
S_{1c}	$Z_1 = 12$	$f_1 = 5$
	$Z_2 = 137$	$f_2 = 5$
	$Z_3 = 137$	$f_3 = 7$
	$Z_4 = 12$	$f_4 = 7$

fore, any voltage fluctuation results also in phase fluctuation.

Here, we deal with the case of non-degenerate amplifiers with two separate modes. Figure (4.5) gives a schematic representation of the device as well as the layout of the sample. We choose two modes for the signal and the idler, respectively at two different frequencies $f_s \neq f_i$. Each of it consists of two quarter-wave resonators in series with characteristic impedances Z_1 and Z_2 and resonance frequencies $f_1 = f_2 = f_s$ for the signal mode, and with characteristic impedances Z_3 and Z_4 and resonance frequencies $f_2 = f_3 = f_i$ for the idler mode, connecting to the SQUID. The impedances Z_2 and Z_3 control the characteristic impedance of the modes and Z_1 and Z_4 their bandwidth.

In figure (4.6), we plot the real part of the impedance seen by the Josephson junction as a function of the frequency f for three variations of the device: S_{1a} (blue curve), S_{1b} (orange curve), S_{1c} (magenta curve). In table (4.1), we summarize the main parameters for these three variations. As can be seen in figure (4.6), the impedance presents two resonances, one corresponds to the signal mode at 5 GHz and the second one corresponds to the idler mode at 7 GHz. The bandwidth of the peaks at f_s over 1 GHz for the first variation (S_{1a}), 500 MHz for the second variation (S_{1b}) and 100 MHz for the third variation (S_c).

4.3.2 Large bandwidth ICTA implementation

Here, our goal is to implement a large bandwidth amplifier using a very simple circuit, again by shaping the impedance of the electromagnetic environment seen by the junction.

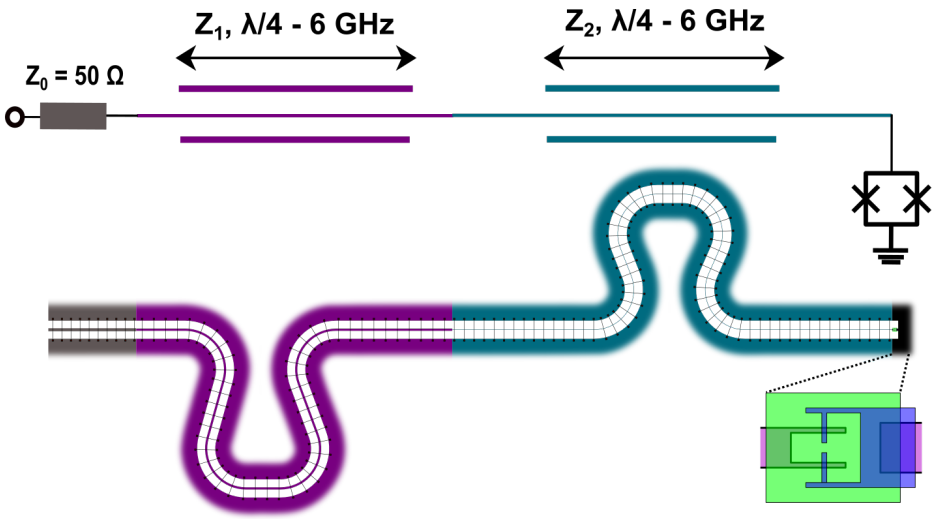

Figure 4.7 **Large bandwidth amplifier, first realisation:** Two quarter-wave resonators in series (magenta and blue resonators), both with resonance frequencies equal to 6 GHz, are connected, at one end to grounded SQUID and at the other end to 50 Ω port (grey transmission line). Table 4.2 indicates values of the four quarter-wave segments we have implemented.

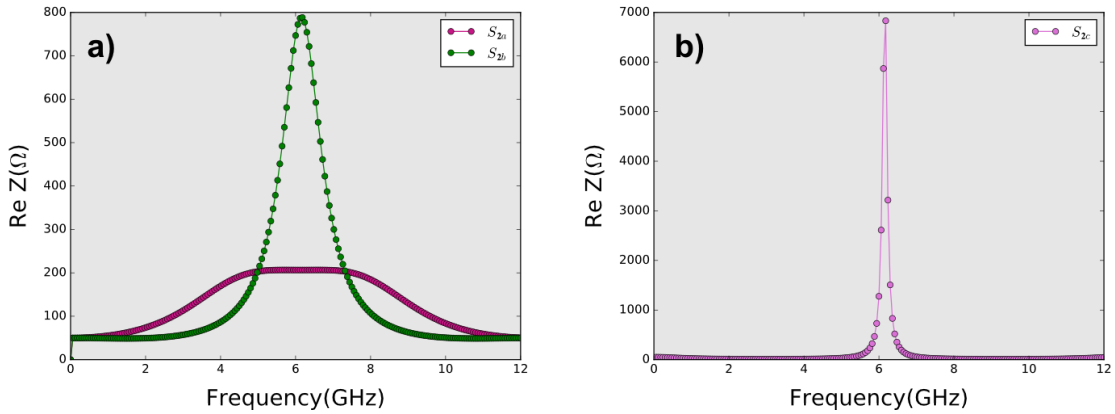

Figure 4.8 **Real part of the impedance seen by the SQUID as a function of the frequency f for large bandwidth amplifiers, first realisation : a)** Magenta line: Re $Z(f)$ for the first type S_{2a}, where we have large resonances at 6 GHz frequency range, flat impedance between 4 GHz and 8 GHz. Red line: Re $Z(f)$ for the second type S_{2a}, where we have resonance over 1 GHz frequency range. **b)** Pink line: Re $Z(f)$ shows a very high impedance at the signal frequency f_s The three curves show one pick at 6 GHz

We use here a single high-bandwidth mode to accommodate both the signal and the idler. We propose two different designs for large bandwidth ICTA:

The first circuit is realized by cascading different quarter-wave resonator sections with varying characteristic impedances Z_1 and Z_2. These two resonators have the same resonance frequency $f_1 = f_2$. This sequence of transmission lines is connected, at one end to 50 Ω port and at the other end to a SQUID connected to ground at the other end as shown in figure (4.7). As the previous sample, variations are made in order to optimize the bandwidth of our amplifier: S_{2a} (magenta curve), S_{2b} (green curve), S_{3c} (pink curve). We indicated the parameters used for the implementation of these devices in table (4.7).

The real part of the impedance seen by the SQUID as a function of the frequency f when looking into the circuit is shown in figure (4.8.a) and (4.8.b). It can be seen that we have a flat impedance between 4 GHz and 8 GHz which correspond to our measurement frequency range (figure (4.8.a), magenta line). Note that a flat $Re\ Z(f)$ implies $Im\ Z \approx 0$ due to Kramers Kronig relations, a flat $ReZ(f)$ is therefore similar to the BW optimizations proposed for JPAs by cancelling $Im\ Z$ [73]. We can reduce the bandwidth of the resonance to increase the impedance at the signal frequency f_s (figure (4.8.a), green line and figure (4.8.b), pink line) by adjusting the characteristic impedance Z_1 and Z_2, exactly like in the previous case.

Table 4.2 Parameters of the sample S_2 for reflection amplifier with large bandwidth by cascading different quarter wave resonators

S_2	$Z(\Omega)$	f (GHz)
S_{2a}	$Z_1 = 62$	$f_1 = 6$
	$Z_2 = 126$	$f_2 = 6$
S_{2b}	$Z_1 = 37$	$f_1 = 6$
	$Z_2 = 147$	$f_2 = 6$
S_{2c}	$Z_1 = 12$	$f_1 = 6$
	$Z_2 = 147$	$f_2 = 6$

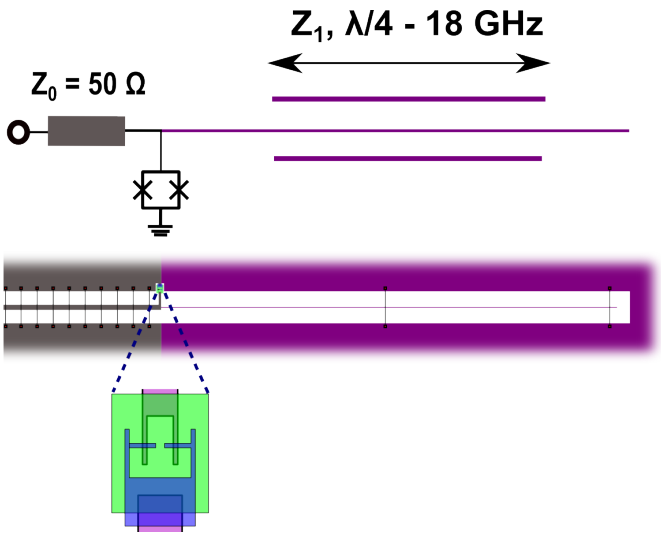

Figure 4.9 **Large bandwidth amplifier design, second realisation:** A grounded SQUID connected to ground on one end. The other end is coupled at one end to a 50 Ω (grey) transmission line as well as a quarter wave resonator (violet resonator) with a resonance frequency $f_1 = \nu_J$ which is open at its second terminal.

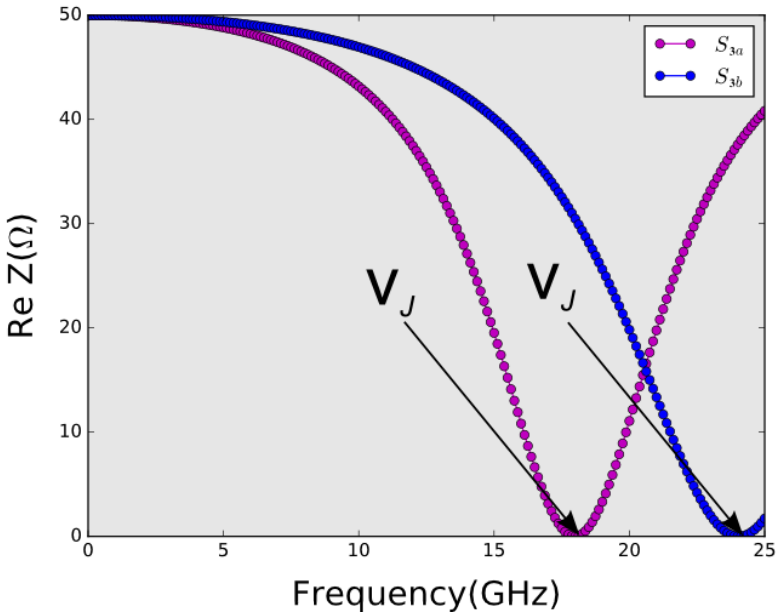

Figure 4.10 **Real part of the impedance seen by the SQUID as a function of the frequency f for large bandwidth amplifiers, second realisation:** Magenta line: Re $Z(f)$ for the first type (S_{3a}), where we have a large impedance up to 15 GHz. This curve shows zero impedance corresponding to the pump frequency ν_J= 18 GHz. Blue line: Re $Z(f)$ for the second type (S_{3b}), where we have large impedance up to 20 GHz. This curve shows zero impedance corresponding to the pump frequency ν_J= 24 GHz.

Figure (4.9) shows another implementation of large width amplifiers. The sample consists of SQUID connected to a 50 Ω port and one quarter-wave resonator with a characteristic impedance Z_1 = 150 Ω and a resonance frequency $f_1 = \nu_J$. This quarter wave resonator is open in its second end in order to have zero impedance at ν_J. We use this method to suppress the process where the energy of a tunnelling Cooper pair is converted to one photon at ν_J. We designed two samples: S_{3a} (magenta curve) and S_{3b} (blue curve) in which we fixed the pump respectively at 18 GHz and 24 GHz (see figure 4.10). We have a very large envelope from zero frequency to the pump frequency. However the impedance is very low.

4.3.3 Low noise ICTA implementation

As explained before in chapters (1) and (2), an ideal Josephson parametric amplifier operating close to the quantum limit should work only with amplification term a^+b^+c where a is the signal annihilation operator, b is the idler annihilation operator and c is the pump annihilation operator (in our case the Cooper pair tunneling operator). Any additional conversion term can add noise.

In this section, we propose one implementation of reflection microwave amplifiers where we try to suppress these conversion terms, as always via the impedance seen by the SQUID. As can be seen in figure (4.11), first the circuit includes one quarter-wave resonator with characteristic impedance Z_1 and resonance frequency $f_1 = f_s$, connected, at one end to 50 Ω port and at the other end via the SQUID to ground. One half-wave resonator with characteristic impedance Z_3 and resonance frequency $f_3 = \nu_J$ is connected to the same end of the SQUID. The other end is connected to ground via a large capacitor (C = 100 pF), acting as a short at the operation frequency. The half wave resonator allows to have an antiresonance at frequency $k * \nu_J$ and close to zero frequency but not to zero frequency which gives the opportunity to apply the DC voltage. A second quarter-wave resonator with characteristic impedance Z_2 and resonance frequency $f_2 = f_s + \nu_J$ is open on one end and connected to the Josephson junction on the same end as the others. This quarter-wave resonator allows to have antiresonances at $k' * (f_s + \nu_J)$, k' =1,3,5,7,... In fact, when the frequency is equal to $k' * (f_s + \nu_J)$, the impedance seen by the Josephson junction is $\frac{Z_2^2}{Z_L}$, as explained in equation (4.13). As, $Z_L = +\infty$, the Josephson junction sees zero impedance at $f_s + \nu_J$. By adjusting the impedances Z_1 and Z_2, we can increase the bandwidth of the resonances. Then, two samples are designed: S_{4a} and S_{4b}. Table (4.11) shows the main parameters for different devices.

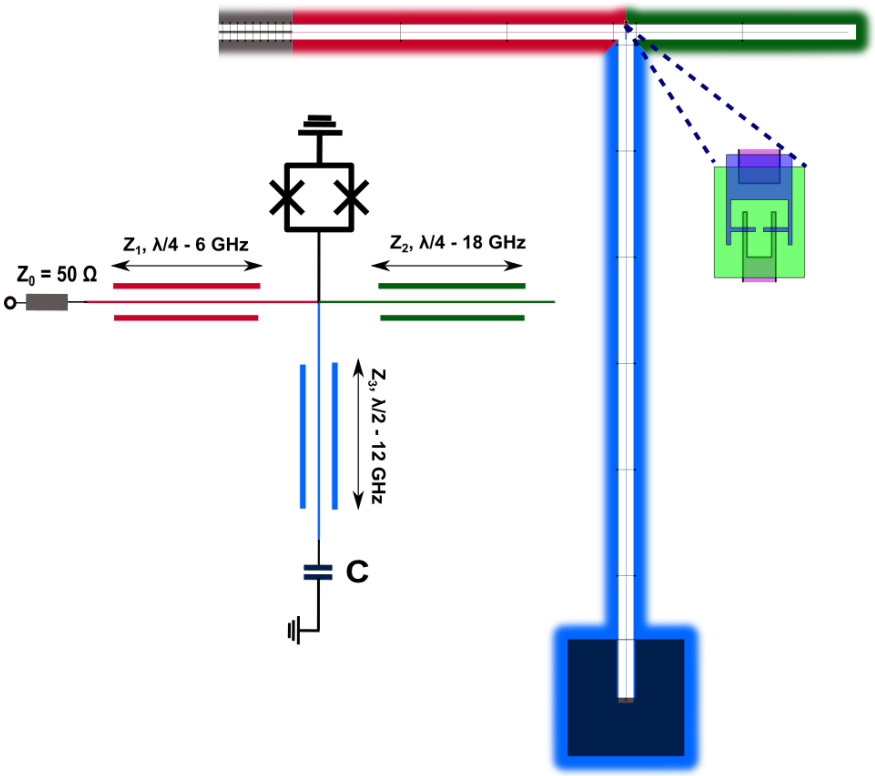

Figure 4.11 **Low noise amplifier implementation:** A SQUID is grounded on one end and coupled at the other end to a quarter wave resonator at f_s = 6 GHz (red transmission line) which is in turn, connected to a 50 Ω port (grey transmission line). The SQUID is also coupled at its second end to an open quarter wave resonator (green resonator) with a resonance frequency $f_s + \nu_J$ = 18 GHz, as well as to a half-wave resonator, and a capacitance C= 100pF to ground at its other end helping to suppress the impedance corresponding to pump frequency and near to zero frequency.

Table 4.3 Parameters of the sample S_4 for reflection amplifiers with low noise

S_4	$Z(\Omega)$	f (GHz)
S_{4a}	Z_1 = 150	f_1 = 6
	Z_2= 150	f_2 = 18
	Z_3= 150	f_2 = 12
S_{4b}	Z_1 = 50	f_1 = 6
	Z_2= 50	f_2 = 18
	Z_2= 150	f_2 = 12

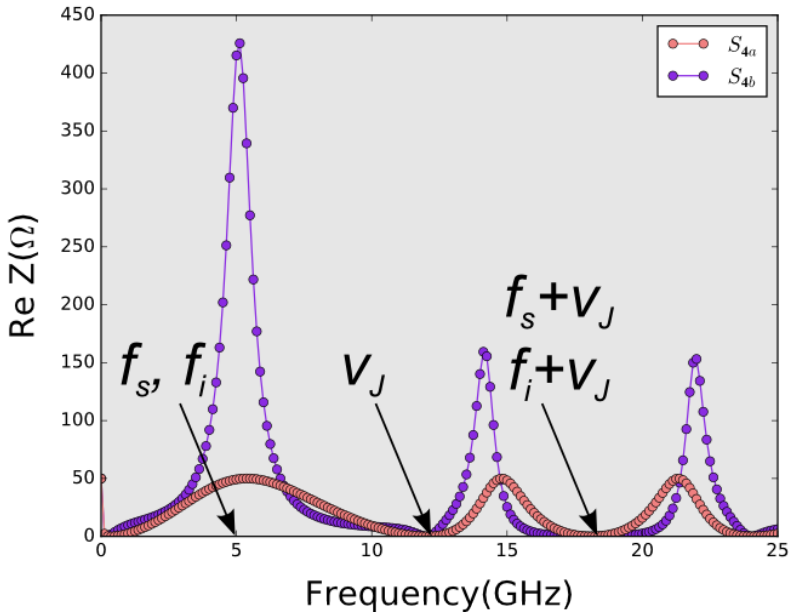

Figure 4.12 **Real part of the impedance seen by the SQUID as a function of sfrequency f for low noise amplifiers:** Pink line: Re $Z(f)$ for the first type (S_{4a}), where we have a large resonance over 5 GHz frequency range. Violet line: Re Z(f) for the second type (S_{4b}), where we have resonance over 1 GHz frequency range. The two curves show one peak at 5 GHz and zero impedance at ν_J = 12 GHz and $\nu_J + f_s$ = 18 GHz. For parameters, see table (table:S4).

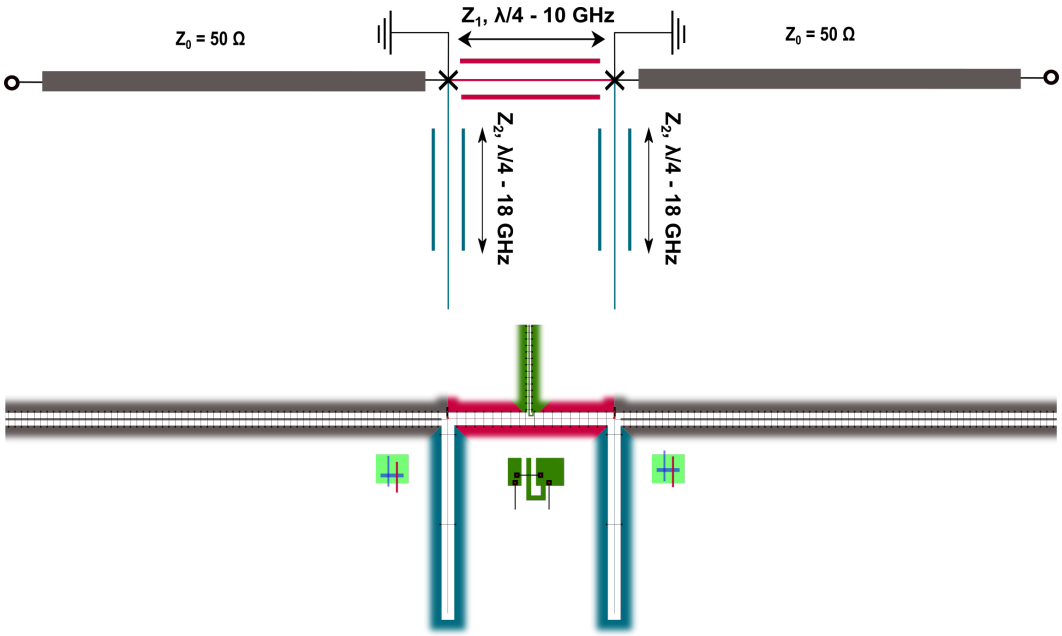

Figure 4.13 **Transmission amplifier implementation:** Two Josephson junctions are connected, at one end to open quarter wave resonators at the pump frequency ν_J = 18 GHz and at the other end linked via a second quarter wave resonator at the same frequency. The same end of each junction is coupled to a 50 Ω port. The sample is symmetric from the right to the left and vis versa.

The real part of the impedance seen by the Josephson junction as a function of the frequency f is shown in figure (4.12). We indeed observe zero impedance at the frequency of the pump ν_J, the signal plus the pump $f_s + \nu_J$, the idler plus the pump $f_i + \nu_J$ as well as the second harmonic of the pump $2\nu_J$. However, the impedance has resonances at frequency f_s and f_i. By adjusting the characteristic impedances Z_1, Z_2 and Z_3 as well as the length l_1 of the segment of impedance Z_1, we can tune the bandwidth of the resonance around the signal frequency.

4.4 Transmission amplifiers

All the amplifiers presented before are reflection amplifiers. With this kind of amplifiers, we use only one port, through which we send the input signal and we measure the amplified output signal. Thus, in order to separate incoming and outgoing signals travelling in the same port, we have to add circulators at the output of the amplifier. However, these circulators introduce losses of the order of 1 dB for each circulator which adds more noise at the output of the amplifier [51, 50]. Transmission amplifiers might solve this issue, in particular, if the

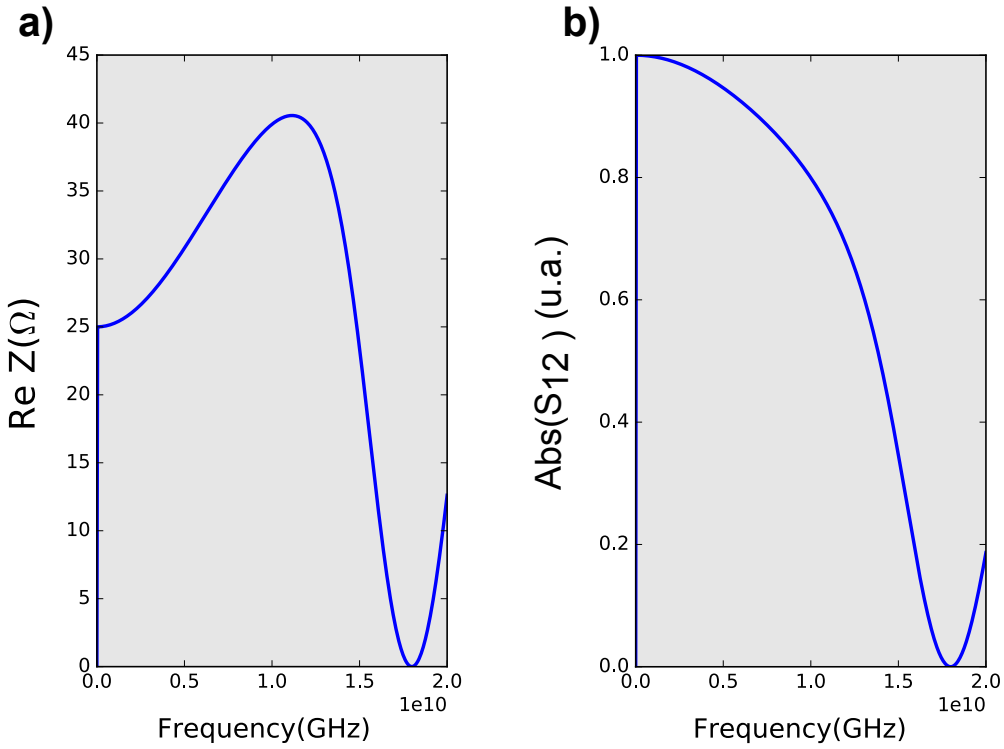

Figure 4.14 **a)Real part of the impedance seen by each junction as a function of the frequency f for transmission amplifiers :** Re $Z(f)$ shows a resonance mode at 11 GHz and zero impedance at ν_J= 18 GHz. **a) Transmission coefficient S_{12} of the scattering matrix S simulated from the circuit shown in figure(4.13) without junctions** We have perfect transmission at low frequency but it decreases with the frequency. In our measurement range, between 4 GHz and 8 GHz, the transmission S-parameters reduces by 10 % to 20 %

reflected signal is close to the ground state. A second issue is that circulators are bulky and require strong magnetic fields. We try to guide the input signal to have transmission with gain perfect in one way andreflection in the opposite way.

The key element of this design is an extended SQUID where the junctions are separated by $\lambda/4$ at ν_J. As can be seen in figure (4.13), it consists of two identical Josephson junctions separated by a quarter-wave resonator with a characteristic impedance Z_1 = 130 Ω and a resonance frequency f_1 = 18 GHz. Each junction is coupled to a 50 Ω port and a quarter-wave resonator with a characteristic impedance Z_2 = 150 Ω and a resonance frequency f_2 = 18 GHz. This resonator is opened at its second end in order to obtain zero-impedance at f_p. The design of this sample is symmetric from the two sides (see figure (4.13)). Directivity is introduced by applying a flux $\Phi_0/4$ to the SQUID. Then the phase delay acquired by propagation along the SQUID and the magnetic flux cancels in one direction causing constructive interferences, in the other direction they add causing destructive interferences.

The input impedance seen by each junction is shown in figure (4.14.a). We indeed observe zero impedance at the pump frequency to eliminate the emission of photons at the frequency ν_J as explained before. The Re $Z(f)$ shows one resonance around 11 GHz. In figure (4.14.), we plot the transmission coefficient of the S-matrix as a function of the signal frequency without the Josephson junctions. In our measurement range, between 4 and 8 GHz, the transmission coefficient is reduced by 10% to 20%.

4.5 Complete samples and perspectives

In the previous sections, we have discussed the designs of amplifiers optimizing on the one hand the ICTA bandwidth and on the other hand the ICTA noise. In this section we propose another design able to combine these characteristics simultaneously. The main idea here is to choose the idler mode at a high frequency which helps to reduce the thermal noise as well as to suppress the conversion terms and to keep a large resonance associated to the signal mode. This idea is not fully played out yet but it is described in our patent.

In this design, we choose the pump frequency ν_J = 300 GHz, the idler frequency f_i = 290 GHz and the signal frequency f_s = 10 GHz. As shown in figure (4.15), the SQUID is coupled to a high frequency branch on one side. It consist of a coupled-line quarter wave transformer with resonance frequency $f_1 = \nu_J + f_s$ = 310 GHz even mode impedance Z_{1e} = 25 Ω and add mode impedance Z_{1o} = 20 Ω it Dc couples the junction to ground and

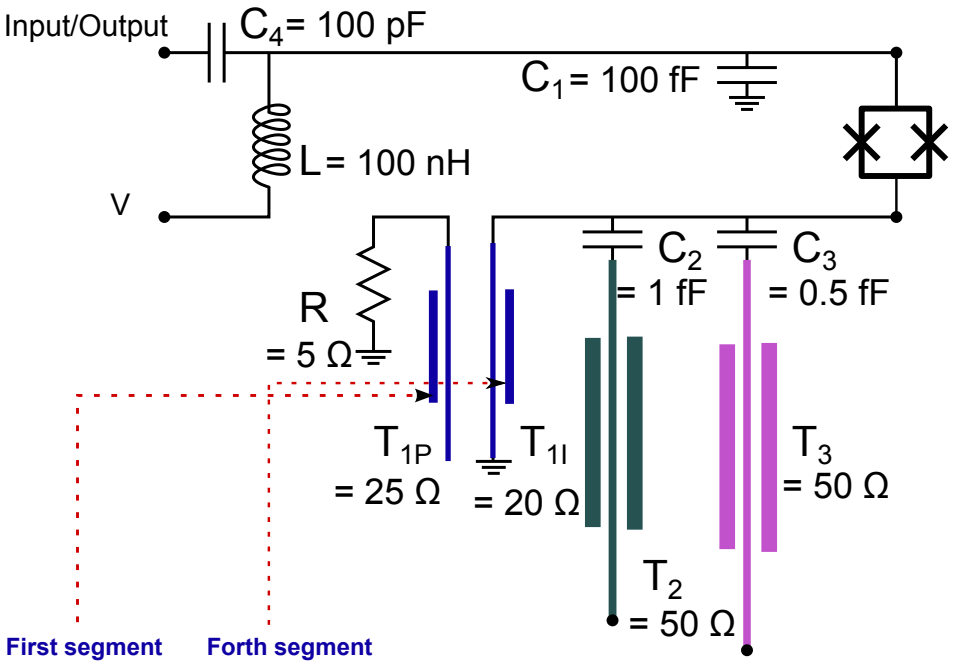

Figure 4.15 **High frequency amplifier**

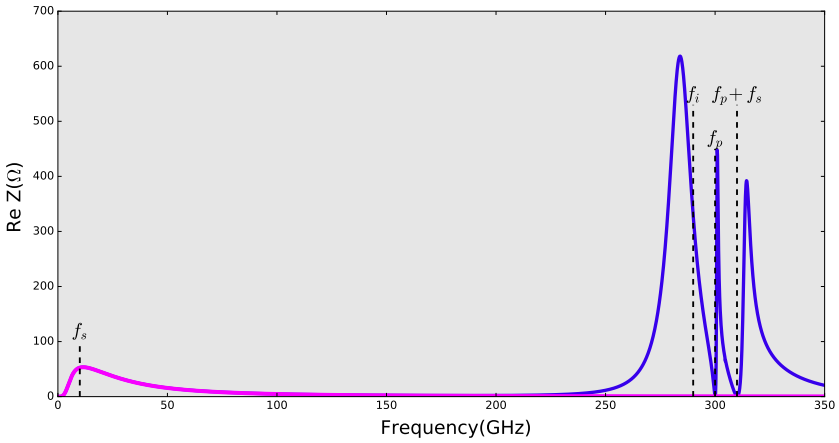

Figure 4.16 **The real part of the impedance seen by the SQUID as a function of the frequency for high frequency amplifiers:** The blue line corresponds to Re $Z(f)$, the purle line to the port of the impedance due to the RF port. We have two resonances, the first one at the signal frequency f_s = 10 GHz and the second one at f_i = 290 GHz. We have also two anti-resonances at the pump frequency ν_J = 300 GHz and at $\nu_J + f_s$ = 310 GHz.

resonantly couples it to a R = 5 Ω load resister. At half-wave resonator with a characteristic impedance Z_2 = 50 Ω and a resonance frequency f_2 = 320 GHz and a capacitance C_2 = 1fF are used to suppress the conversion term at frequency $\nu_J + f_s$. A second half wave resonator with a characteristic impedance Z_3= 50 Ω and a resonance frequency f_3 = 304.6 GHz and a capacitance C_3 = 0.5 fF help to suppress the pump mode. Finally, two capacitance C_1 = 100 fF and C_4 = 100 pF, and one inductance are used as bias T and to shape the signal mode.

The real part of the impedance seen by the SQUID as a function of the frequency is shown in figure(4.16) by the blue line. The part of the impedance due to the coupling to the input/output port is shown in the same figure (pink line) to prove that the circuit is not sensitive to high frequency modes off chip.

Conclusion

In this chapter, we have discussed a second generation of ICTA designs, intended for a fabrication process based on niobium nitride. Two types of amplifiers are discussed here: reflection and transmission amplifiers. For the reflection amplifier, we proposed several implementations to improve the ICTA bandwidth and noise. In the next chapter, we will explain the fabrication process of theses samples, elaborated in this work.

Chapter 5

Fabrication

This chapter is organized into two main sections:

1. **Fabrication process:** describes the fabrication techniques used to make vertical NbN/MgO/NbN Josephson junctions and coplanar waveguides. We also describe the characteristics of NbN thin films as well as the characteristics of Josephson junctions and resonators.

2. **Method of sample selection:** summarizes the different experimental methods used to probe the samples. It consists of two setups corresponding to two temperatures: 300 K measurement setup and 4.2 K measurement setup. We use an automated probe-station to measure the resistance of Josephson junctions at room temperature in order to select the working samples. Then, we measure our devices at 4.2 K in a helium bath cryostat for precharacterization of the samples: we measure the I-V characteristics of Josephson junctions in order to be sure that they're not shunted and the reflection S-parameters of our CPWs in order to be sure that the resonance frequency is included our measurement bandwidth (between 4-8 GHz). The best candidates are measured at low temperature, 12 mK, in the dilution refrigerator (see chapter (1)).

5.1 Fabrication

There are two reasons for which the implementation of Superconducting Quantum Circuits (SQC) has made remarkable progress in the last years and it is now more and more the subject of intense research: On the one hand because they have opened a new area of fundamental science and on the other hand because they are a promising implementation of quantum information technologies. Owing to their simple fabrication process, superconducting circuits based on Al/AlO_x/Al junctions coupled to niobium transmission lines are used

by many groups nowadays [74, 75]. NbN is an important superconducting material for the development of SQC thanks to its attractive characteristics such as a large superconducting gap corresponding to 1.2 THz, much higher than the niobium gap (750 GHz), and its high critical temperature corresponding to 16 K [76, 77]. These two proprieties have a particular interest in my project because they offer an opportunity to fix the idler mode at high frequencies and then to reduce the ICTA noise. During my thesis, I developed, with my colleagues, a new process of fabrication for ALL niobium nitride circuits able to produce high quality NbN/MgO/NbN junctions.

This process has three niobium nitride layers, in addition to a MgO layer used as a tunnel barrier and a Si_3N_4 insulating layer. The devices are defined after two Electron Beam Lithography (EBL) steps and three Optical Lithography (OL) levels and after using Reactive Ion Etching (RIE) to pattern junctions, electrodes and insulating layers. In this section, the fabrication process of vertical NbN/MgO/NbN junctions with self-aligned spacers is described. Then, the fabrication process of CPW and finally the characteristics of both Josephson junctions and resonators are presented and discussed in the two last subsections.

5.1.1 Fabrication of NbN/MgO/NbN junctions

The fabrication of vertical NbN/MgO/NbN Josephson junctions, combining several steps in sequence, is shown schematically in figure (5.2). After the deposition of the trilayer, an EBL step is used to pattern the alignment Ti/Pt markers in corners of the chip (10x10 mm) using lift-off. Then, a first OL level is performed in order to define the geometry of the lower layer of the junctions from a negative resist and an aluminium hard mask. RIE is used to remove the trilayer not covered by the hard mask on an Oxford ICP Plasmalab100 RIE machine. In the second step, after the deposition of Si_3N_4, another OL level is carried out defining regions where the dielectric will be etched while keeping the insulating layer at borders of basic structures to protect the trilayer. Junctions fabrication is accomplished using a combination of both OL and EBL steps to be able to define, respectively, small junctions ($0.2\,\mu m^2$, $0.5\,\mu m^2$) and big junctions ($1\,\mu m^2$, $2\,\mu m^2$) and a third step of RIE is made. Detailed steps are shown below:

a)

		Thickness(nm)	SF6 (sccm)	CH2F2 (sccm)	Ar (sccm)	Pressure (mtorr)	ICP (W)	Forward(W)	Time (s)
NbNsup	NbN_{etch}	180	5	25	40	5(15)	500	70	156
	NbN_{over}		10	10	40	20	500	20(50)	15
MgO	MgO_{etch}	Repeated 3 times for 5 nm			100	5	500	150	20
	Pump								180
	Vent								90
NbNinf	NbN_{etch}	30	5	25	40	5(15)	500	70	EPD
	NbN_{over}		10	10	40	20	500	20(50)	15

b)

	Thickness (nm)	SF6 (sccm)	CH2F2 (sccm)	Ar (sccm)	Pressure (mtorr)	ICP (W)	Forward(W)	Time (s)
Si_3N_4	300	5	25	10	5(15)	1000,500,250	150,5	EPD

c)

	Thickness(nm)	CH_3COOH (ml)	Time (s)
MgO	10	2 + 200 EDI	20

d)

		Thickness (nm)	SF6 (sccm)	CH2F2 (sccm)	Ar (sccm)	Pressure (mtorr)	ICP (W)	Forward(W)	Time (s)
NbN_{Top}	NbN_{etch}	350	5	25	40	5(15)	500	70	EPD
	NbN_{over}		10	10	40	20	500	20(50)	10

e)

	O_2 (sccm)	Pressure (mtorr)	ICP (W)	Forward(W)	Time (s)
O_2 plasma	45	30	500	0	20

Figure 5.1 **The employed etch recipes: a)** Trilayer NbN/MgO/NbN etch recipe. **b)** Si_3N_4 spacer etch recipe. **c)** MgO wet etching recipe. **d)** $NbN_{Topwiring}$ etch recipe. **e)** Descumming O_2 plasma. Pressures, ICP, flowraters for each gas, time of etching and other basic parameters used in this work are summarized in this table. *EPD: "End point detection".

Deposition of the trilayer

Our devices are built from a NbN(30 nm)/MgO(5 nm)/NbN(180 nm) trilayer on an entire standard 4" Si/SiO_2(500nm) substrate using an Alcatel SCM 600 DC and RF magnetron sputtering machine. We start by depositing a thin MgO (20 nm) under-layer MgO_{Buffer} as etch stop and in order to increase the critical temperature T_c of the trilayer, after cleaning the wafer by back sputtering (10 min, 250 W). A NbN base (NbN_{Bottom}) is DC magnetron sputtered with the substrate holder rotating from a 150 mm niobium (Nb) target in an argon ($P_{Ar} = 150.10^{-4}$mbar) and nitrogen ($P_{N_2} = 20.10^{-4}$ mbar) atmosphere. The deposition rate is 3.8 $nm.s^{-1}$. The MgO barrier layer is deposited by RF magnetron sputtering also with rotating mode from a MgO target using a 125 mm diameter in a pure argon ($P_{Ar} = 130.10^{-4}$mbar) atmosphere. The barrier deposition time is 100 s with a deposition rate of approximately 0.05 $nm.s^{-1}$. The NbN counter electrode(NbN_{Top}) is deposited under the same conditions as the NbN base, but with the substrate fixed on top of the target.

Etching of the trilayer

To process the Josephson junctions, the trilayer is patterned with RIE. First, the wafer is coated with an UV negative photoresist (AZ 5214). After spinning the wafer at (4000 tr/min, 30s) to produce an uniform coating, the resist is baked for 180 s at 90°C. When exposed to UV light, the negative resist becomes polymerized, and more difficult to dissolve in the developer. Therefore, the negative resist remains on the surface of the substrate where it is exposed, and the developer solution (DEV AZ Developer diluted 1:1 in EDI, 30 s) removes only the unexposed areas and the polymerized regions remain. We then deposit an Al hard-mask (150 nm) by evaporation and lift-off in acetone (2.5 h + 10 min with ultrasound (US)) and IPA (2 min with US). This aluminium hard mask remains only in the areas not covered with resist. The major advantage of this step is to obtain a mask able to withstand a dry etch much longer than photoresist, which helps to obtain very vertical walls.

The patterned wafers are exposed to an RF plasma. The NbN is attacked anisotropically both chemically with SF_6 and mechanically with Ar. Addition of a highly polymerizing CH_2F_2 gas generates a fluorocarbon layer on the side walls to prevent under etching. The NbN is etched in two steps, a main step and an overtech step for better homogeneity. This method is called for very directional etching processes. The MgO is etched purely mechanically with a milling step using a strongly biased argon plasma. This step terminated by using a chemical solution (Developer MF26A 5 min + EDI 3 min) to remove the aluminium mask. Figure (6.20), table (a) summarizes the etching parameters such as the pressure and

the inductively plasma ICP for various NbN and MgO layers. A schematic cross-section of the Josephson junctions fabrication before and after trilayer etching are shown, respectively, in figure (5.2.a) and (5.2.b). In the following, we discuss the elaboration of Superconducting Quantum Interference Device (SQUID) as shown on the Scanning Electron Microscope (SEM) image in figure (5.3.a); but the same steps are used to fabricate CPWs (see section (5.1.3)).

Self-aligned spacers

After etching of the trilayer, a thick conformal film of Si_3N_4 (300 nm) is deposited by Chemical Vapor Deposition (CVD) covering the vertical and horizontal surfaces with basically no difference in the film thickness as shown in figure (5.2.c). Then, 10 nm of MgO is deposited on the top of SiN to protect it from overetching during the next steps of the fabrication process. The wafer is coated with a positive UV photosensitive resist (Claraint-AZ-1512-HS) in which a second OL step and a subsequent development define regions where the dielectric will be etched. After that, the MgO is removed from areas not covered by the resist with 1 % acetic acid during 20 s (figure (6.20), table(c)).

For plasma etching of Si_3N_4, we use a mixture of CH_2F_2, SF_6 and Ar. Our objective is to optimize Si_3N_4 etching using an ICP to etch all flat surfaces while leaving self-aligned spacers clinging to the steps in the trilayer (figure (5.2.d)). Figure (5.3.b) shows a SEM micrograph of a Si_3N_4 spacer protecting a step in the trilayer. The optimized pressure, the ICP, flow-rates for each gas, time of etching are presented in figure (6.20), table (b).

Topwiring

NbN top wiring is deposited in the same way as the trilayer after a brief back-sputtering step (10 min at 250W). Device fabrication is completed by combining an EBL step(Ti(10nm)/ Pt(60nm) hard mask deposition defined by PMMA resist and lift-off in acetone) with an OL step (Az-1512-HS). It allows us to define, respectively, small junctions (1 µmx0.2 µm, 1 µmx0.5 µm) and big junctions (1 µmx1 µm, 1 µmx2 µm). Then the NbN topwiring is reactively etched all the way to the MgO tunnelling barrier under the same conditions as the NbN base electrode. That is, the NbN topwiring and the upper layer of the trilayer, not covered by the hard mask or by the optical resist, are completely etched. Despite its very low thickness, the MgO barrier acts as a very effective etch stop. A schematic of the step in the trilayer with self-aligned spacers covered by the NbN counter electrode before and after etching is presented, respectively in figure (5.2.e) and figure (5.2.f). A SEM view of a big Josephson junction 2 μm^2 is shown in figure (5.3.c). Figure (6.20), table(d) list the NbN topwiring

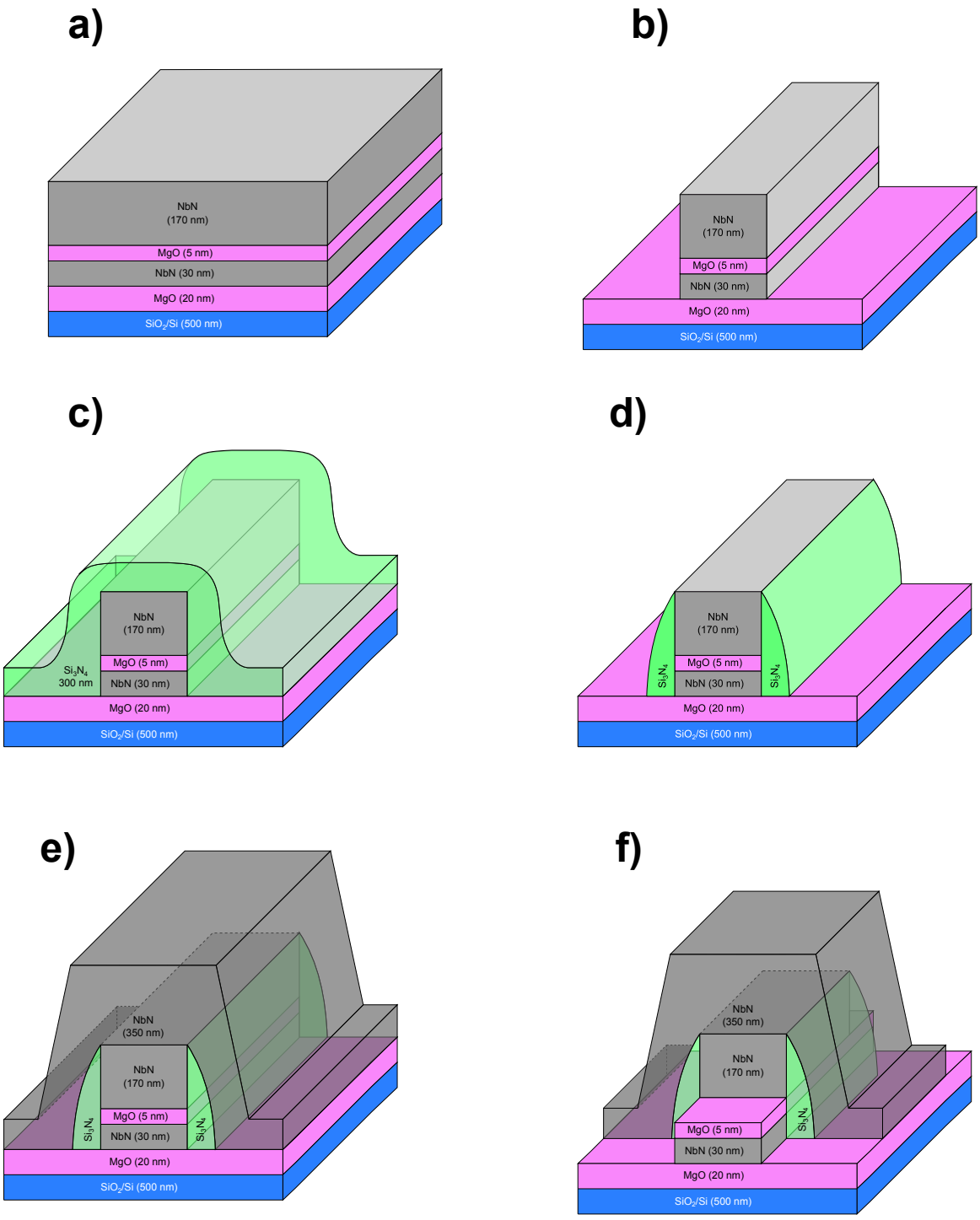

Figure 5.2 **Josephson junction fabrication steps: a)** NbN(30 nm)/MgO(5 nm)/NbN(170 nm) is deposited on top of a thin (20nm) MgO_{Buffer} layer and a hard SiO_2Si substrate before etching **b)** and after etching using an Al hard mask and a negative resist. **c)** The trilayer is conformity covered by 350 nm of Si_3N_4 deposited by CVD **d)** after etching of the Si_3N_4 spacers remain a protect steps in the trilayer. **e)** 350 nm of NbN top-electrode is deposited. **f)** It is etched using a Ti/Pt hard mask.

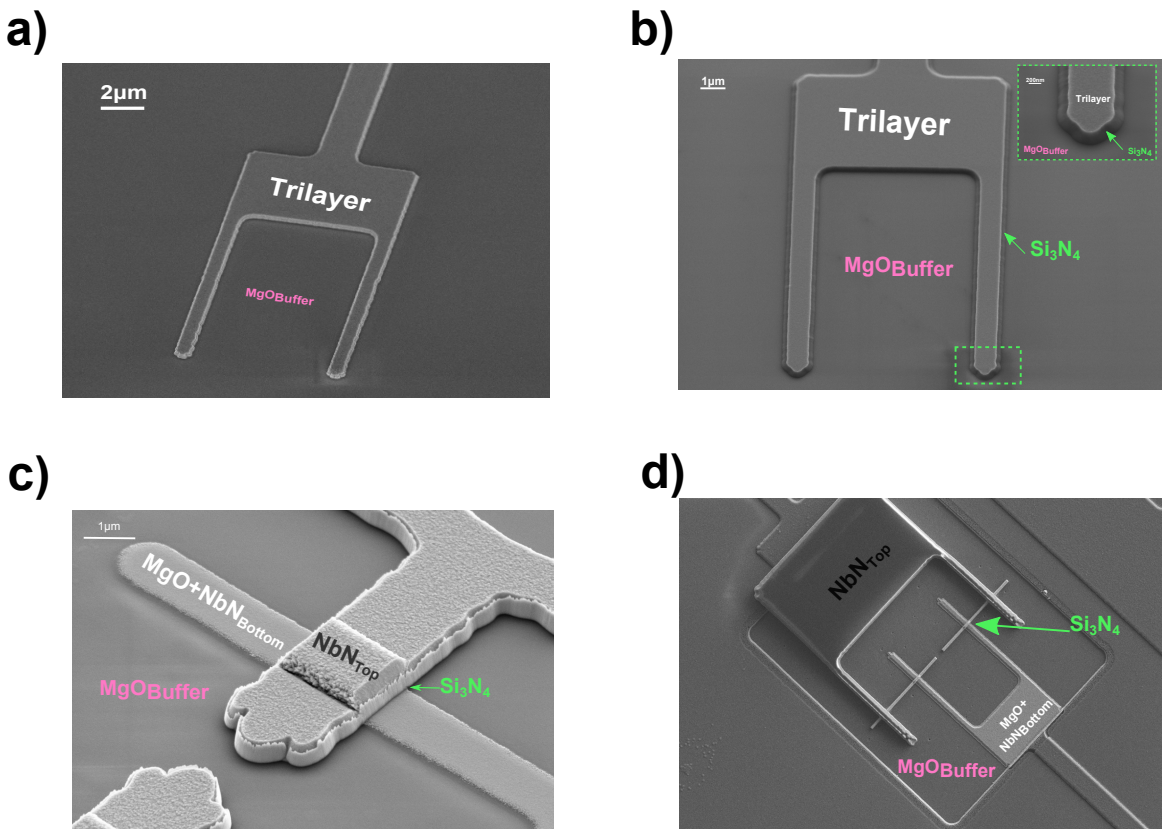

Figure 5.3 **SEM micrographs of several steps of our fabrication process: a)** SEM micrograph of the basic structure of the SQUID after trilayer etching. **b)** SEM micrograph of the basic structure of the SQUID after Si_3N_4 etching. **c)** SEM micrograph of the Josephson junction after top-electrode etching. **d)** SEM micrograph of the SQUID with two small Josephson junctions (0.2 μm^2).

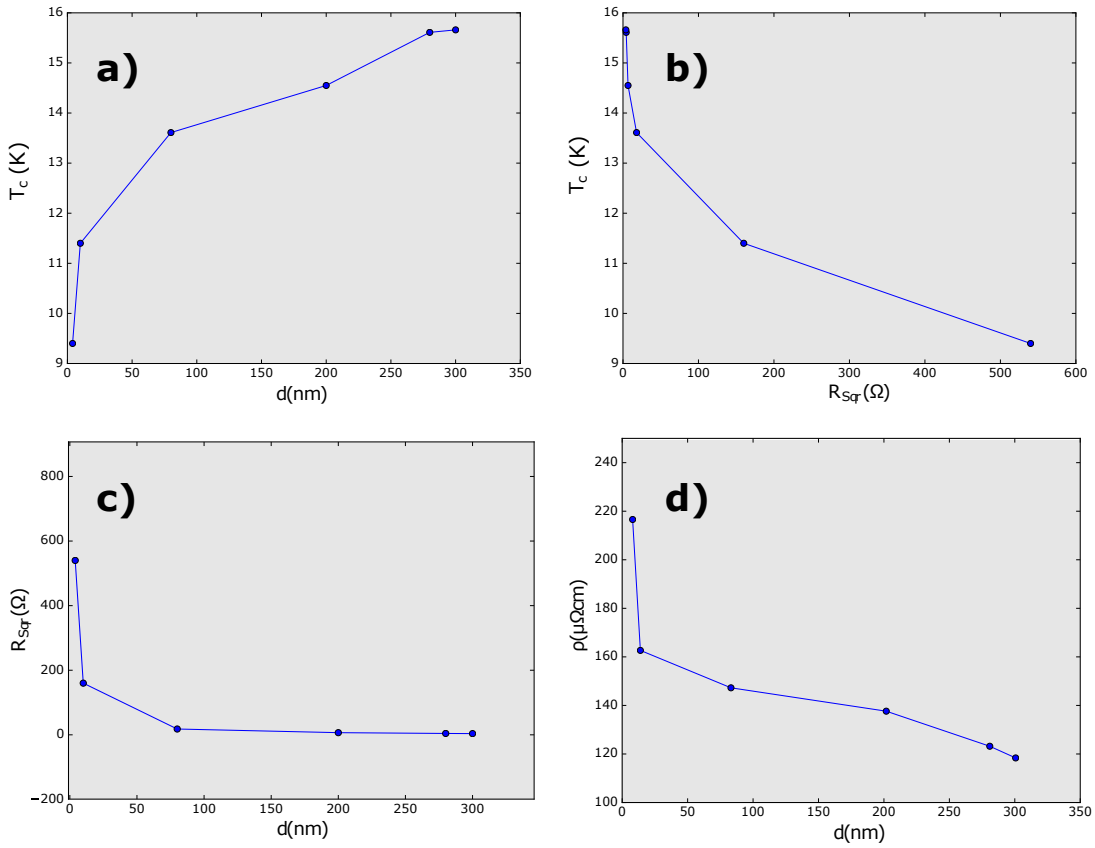

Figure 5.4 **Superconductivity in NbN:** Critical temperature as a function of **(a)** the thickness and **(b)** the resistance per square. **(c)** Resistance as a function of the thickness. **(d)** Normal state resistivity vs T_c.

etching conditions. The finished SQUID is shown in figure (5.3.d).

Before cutting the wafer to measure the samples, a cleaning step is made by using descumming O_2 plasma in order to remove resist residues. This cleaning step is also made after other lithography steps, if necessary. The basic parameters of our plasma recipe are presented in figure (6.20).

5.1.2 Properties of NbN/MgO/NbN Josephson junctions

Properties of NbN thin films

In this paragraph, we present a set of measurements performed in our group on NbN thin films in order to determine their superconducting properties. They exhibit a variety of interesting properties for inelastic Cooper pair tunneling devices such as its high critical

temperature and high kinetic inductance. The films studied in this work are deposited by DC reactive magnetron sputtering with different thicknesses d = 4, 10, 80, 200, 280 and 300 nm. The precision of the thickness is within ± 5 %. Data presented here is collected from these samples measured with a Physical Property Measurement System (PPMS) [78]. In figure (5.4), we plot the critical temperature T_c (a), the resistivity per square $R_\square$ (c) and also the normal state resistivity ρ (d) as a function of the thickness d. Our results show that for the 300 nm NbN film the T_c is 15.66 K. When the thickness d decreases, the T_c of the film decreases to 10 K for 4 nm. It has been shown that there is a direct correlation between the normal-state resistivity ρ and the superconducting T_c [78]; films with lower ρ have higher T_c. On the other hand ρ decreases if the thickness of the NbN film increases. In figure (5.4), we present the critical temperature T_c as a function of the resistivity per square. For 300 nm of NbN, the residual resistivity ratio RRR = R(300K)/ R(20K) $\approx$ 0.7.

Due to its high normal state resistivity, NbN has high kinetic inductance, which is desired for many emerging high frequency micro- and nano-circuit applications especially for the fabrication of superconducting microwave resonators with high characteristic impedances and microwave kinetic inductance detectors. In this work, the kinetic inductance per square value is calculated from λ [79, 75] and the thickness d according to the following formula [80]:

$$L_{kin,\square} = \mu_0 \lambda coth(\frac{d}{\lambda}) \tag{5.1}$$

With μ_0 is the permeability of free space. The penetration depth λ is calculated from the square resistance of the film $R_\square$ and the superconducting gap Δ:

$$\lambda = \sqrt{\frac{\hbar R_\square d}{\mu_0 \pi \Delta}} \tag{5.2}$$

When the penetration depth λ is much higher than the thickness of the film d ($\lambda \gg d$), equation (5.1) can be written as:

$$L_{kin,\square} = \mu_0 \frac{\lambda^2}{d} = \frac{\hbar R_\square}{\pi \Delta} \tag{5.3}$$

In table (5.1), the critical temperature T_c, normal state resistivity ρ, resistivity per square $R_\square$ and the kinetic inductance for all samples are reported. Therefore, NbN has a high normal state resistivity, a large penetration depth ($\lambda \sim 200$ nm) and large kinetic inductance, i.e. for our thinnest films, we do not need to know the thickness in order to evaluate L_{kin}.

Table 5.1 The superconducting properties of NbN thin films.

d(nm)	T_c(K)	$R_\square(\Omega)$	$\rho(\mu\Omega$cm)	$L_{kin,\square}$(pH)
4	9.4	540	216	400
10	11.4	160	160	160
80	13.61	18	144	20
200	14.55	6.7	134	0.8
280	15.61	4.25	119	0.57
300	15.66	3.8	114	0.53

Table 5.2 The superconducting properties of NbN/MgO/NbN Josephson junctions.

$A(\mu m^2)$)	I_c(nA)	J_c) (A cm^{-2}	2Δ (meV)	R_N (KΩ)
0.2	200	0.010	5.10	128
0.5	560	0.0112	5.14	46.4
1	1000	0.010	5.07	25
2	1920	0.0092	5.09	13.2

Properties of Josephson junctions

Figure (5.5) shows the current density-voltage characteristics of four Josephson junctions with several areas 0.2, 0.5, 1 and 2 µm^2 measured at 4.2 K. We define the critical current density $J_c = \frac{I_c}{A}$, with A the surface of the Josephson junction. The junctions have a gap voltage, V_{gap}, defined as the voltage where the differential resistance is maximum, of $\approx$ 5.10 mV which is equivalent to 1.2 THz. Using the I-V data, we can also determine the R_N values for the four samples. The ratio of the subgap resistance (at $V < 2 \triangle /e$) to the normal resistance can be extracted from the same curve at V = 3 mV and V = 10 mV, Rs/Rn is 27.12, 49.9, 44.3 and 45 respectively for junctions sizes 0.2, 0.5, 1 and 2 µm^2 [81, 82, 77]. To extract directly the critical current of the junction, we have to measure the I-V characteristics at lower temperature than 4K. However, we can also calculate the theoretical critical current at zero temperature using both the Ambegaokar-Baratoff formula $I_c R_N = \frac{\pi\Delta(0)}{2e}$ and the relation $2\Delta = eV_g$ (table (5.2)) as :

$$I_c = \frac{\pi V_g}{4R_N} \tag{5.4}$$

The results are shown in table (5.2). The junction parameters obtained for NbN/MgO/NbN junctions show excellent device quality. We choose the area A of junction in logarithmic scale and we find I_c proportional to A as well as a very large superconducting gap (table (5.2)). This propriety has a particular interest to us because it provides a large frequency range.

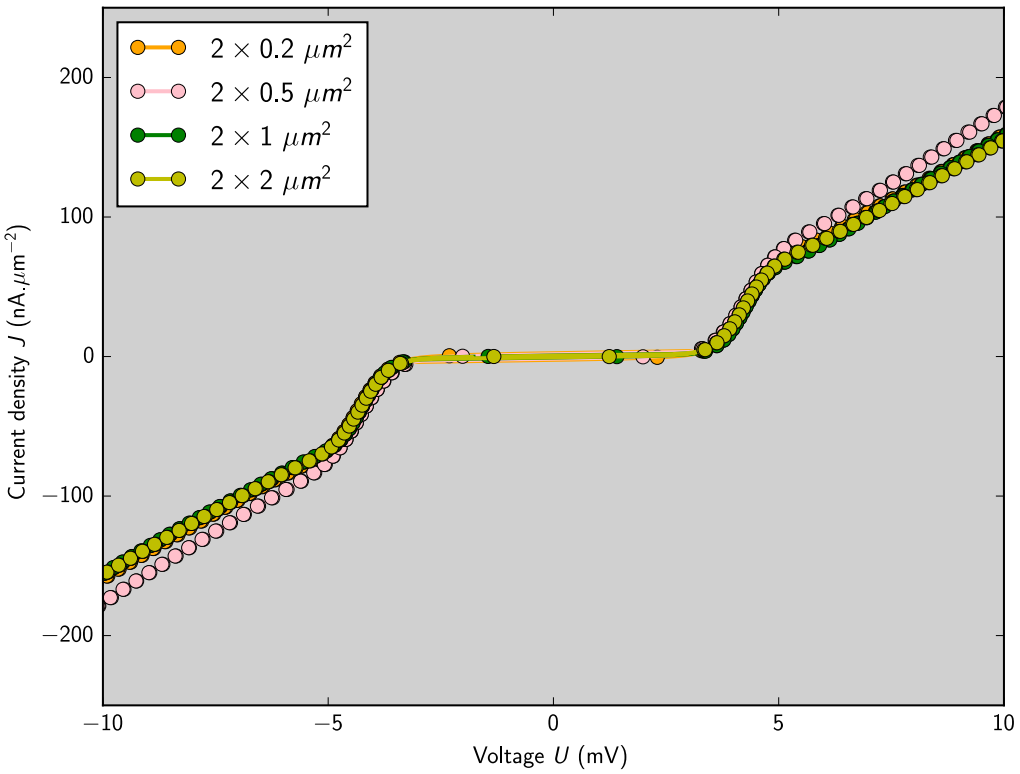

Figure 5.5 **Current density of Josephson junctions:** Current density curves for four SQUID consisting of two Josephson junctions that are connected together in a superconducting loop, with four different sizes 0.2, 0.5, 1 and 2 μm^2.

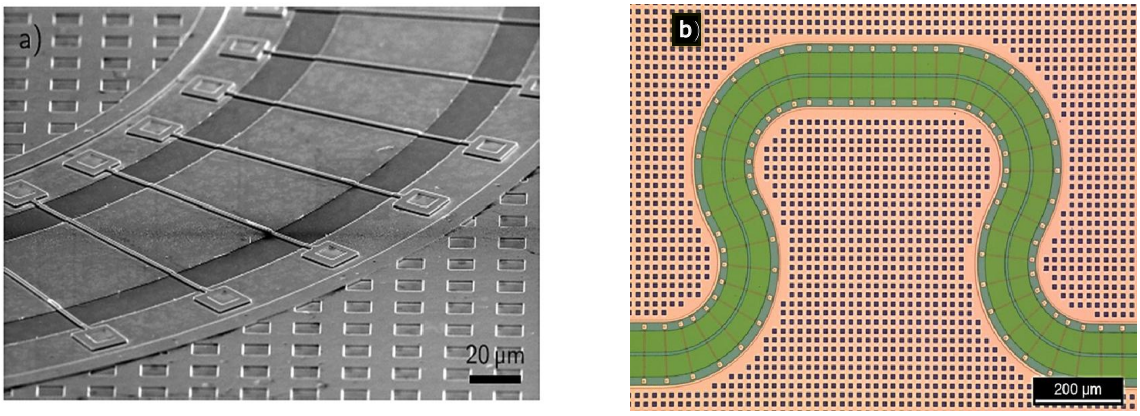

Figure 5.6 **Implementation of a superconducting resonator with a section of CPW: a)** Zoomed SEM micrograph of our CPW. **b)** Optical image of a transmission line, the length is nearly to 8 mm and the width is 100 μm.

5.1.3 Fabrication of CPW resonators

The Inelastic Cooper pair Tunnelling Amplifier mainly consists of Josephson junctions providing strong nonlinear elements coupled to superconducting coplanar wave guides (CPW), with typical operation frequencies in the gigahertz regime (see chapter (4)). Our setup works between 4-8 GHz. In the two previous sections, we discussed respectively the fabrication of Josephson junctions and their proprieties. In this section and in the next one, we discuss the fabrication of our CPW and its proprieties.

A CPW is used to guide radio frequency signals. It consists of a center conductor and two lateral ground planes which are defined, in our fabrication process, in the first OL step and etched into the trilayer (see section (5.1.1)). In order to achieve a resonance frequency around 6 GHz, we design the CPW with length of approximately 10 mm. In order to fit on a chip, the CPW has to be folded. In this case, some problems can be created by the separated ground planes. In fact, when a microwave signal propagates along a bend in the transmission line, it can give rise to a charge imbalance between the ground planes on either side and cause losses due to excitation of ground plane modes. This matter can be easily resolved if we make ground-bridges over our CPWs by opening vias through Si_3N_4 during the second OL and etch steps. Then, we connect these vias with the third OL step using the NbN top wiring. A typical CPW is shown in figure (figure(5.6)). Transmission line parameters used in this work are described in more detail in chapter (4).

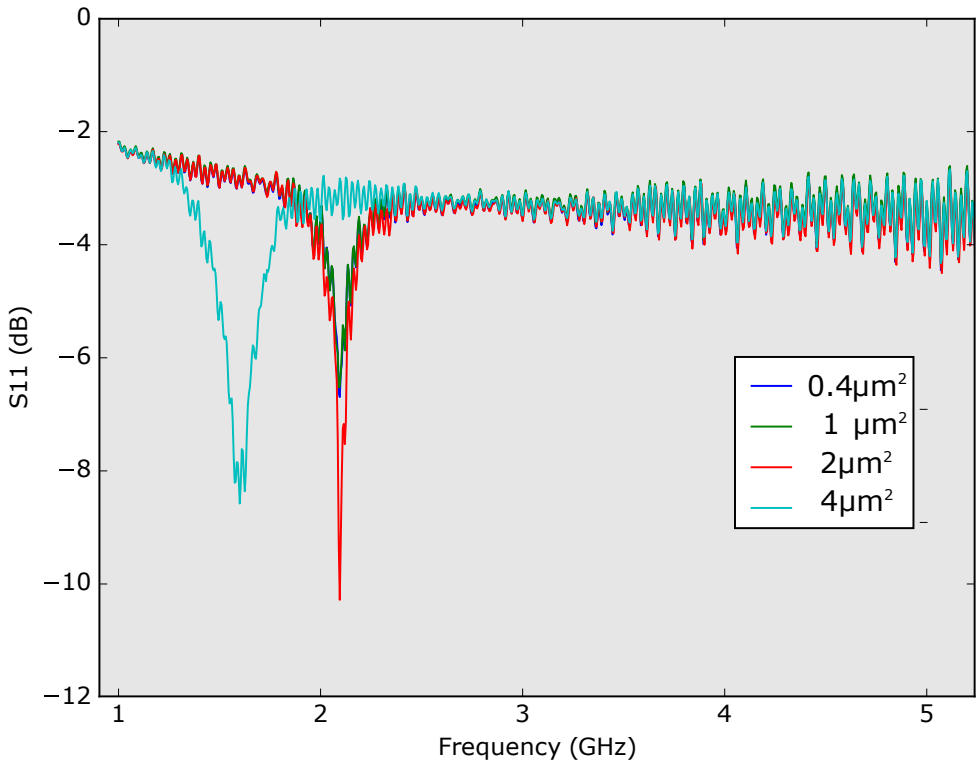

Figure 5.7 **The S_{11} coefficient of the scattering matrix measured at 4 K:** Variation of the resonance frequency f and the quality factor Q for a transmission line coupled to a Josephson junction for four sizes.

5.1.4 Properties of CPW resonators and Josephson junction capacitances

In order to better understand the influence of the capacitance of Josephson junctions on resonance frequencies of CPW, we put, on the same chip, four identical samples which present coplanar transmission lines in series with Josephson junctions to ground with different sizes: 0.2, 0.5, 1 and 2 μm^2. The S_{11} coefficient of the scattering matrix is measured at 4 K as a function of the frequency using a Vector Network Analyzer "VNA". The results for all samples are shown in the same figure (5.7). We see an obvious shift of the resonance frequency of the transmission line coupled to a big Josephson junction (2 μm^2) by 500 MHz (sky blue line). In fact, the CPW can be considered as a LC-resonator and the capacitance of the Josephson junction, if sufficiently big, seen as a capacitance in parallel which may explain this shift. The capacitance extracted from this shift is approximately 3 times larger

than expected. Together with the variation of the kinetic inductance, some devices shift out of our measurement bandwidth (see last chapter). This discrepancy of frequencies has grave consequences for our measurements (see the last chapter).

The thickness of the trilayer, length of CPW, width of the gap, area of vias, and the relative dielectric constants of the substrate material and the dielectric determine the characteristic impedance of the transmission line discussed in chapter (4). Here, we discuss the quality factor of the resonators, defined as the ratio between the average energy stored times the angular frequency ω and the energy loss per second. Q-factor can also be written as:

$$Q = \frac{f_0}{\delta f} \tag{5.5}$$

With f_0 the resonance frequency and δf the full peak width at half maximum. Now, we define the total quality factor Q_L as a function of the internal (Q_{int}) and external (Q_{ext}) quality factors which can be extracted from transmission measurements:

$$\frac{1}{Q} = \frac{1}{Q_{int}} + \frac{1}{Q_{ext}} \tag{5.6}$$

We typically observe internal quality factors > 5000, whereas our designs use $Q_{ext} \approx 10, 50..$ so CPW losses are negligible. The largest quality factors are 35, 34, 41, 8 for respectively samples with junctions sizes 0.2, 0.5, 1 and 2 μm^2. Several CPW, for ICTA samples, have been proposed and studied.

5.1.5 Technical problems and solutions

Our fabrication process has numerous advantages, as presented in the previous sections. However, we had to solve several technical problems in order to stabilise the process. In this paragraph, we choose some difficulties faced which might be useful to others:

Hard mask Our process requires steep edges in the trilayer (see figure (5.3.a)). Resist masks tend to facet and lead to sloped side walls. Therefore we tested several hard masks: Ti, Al, AlO_x, Cr. These hard masks have not be able to resist during trilayer etching and especially during MgO due to the strong argon plasma used. We also tried with 60 nm of Pt hard-mask. This material resists well but it can not be removed after etching except with HF which, in turn, etch the NbN. Therefore we explored a Al/Pt double layer in order to dissolve Al in a wet etch and lift-off Pt. But this also created an issue because aluminium and platinum react exothermically; on top of resist this produces a chain reaction. As a consequence, the

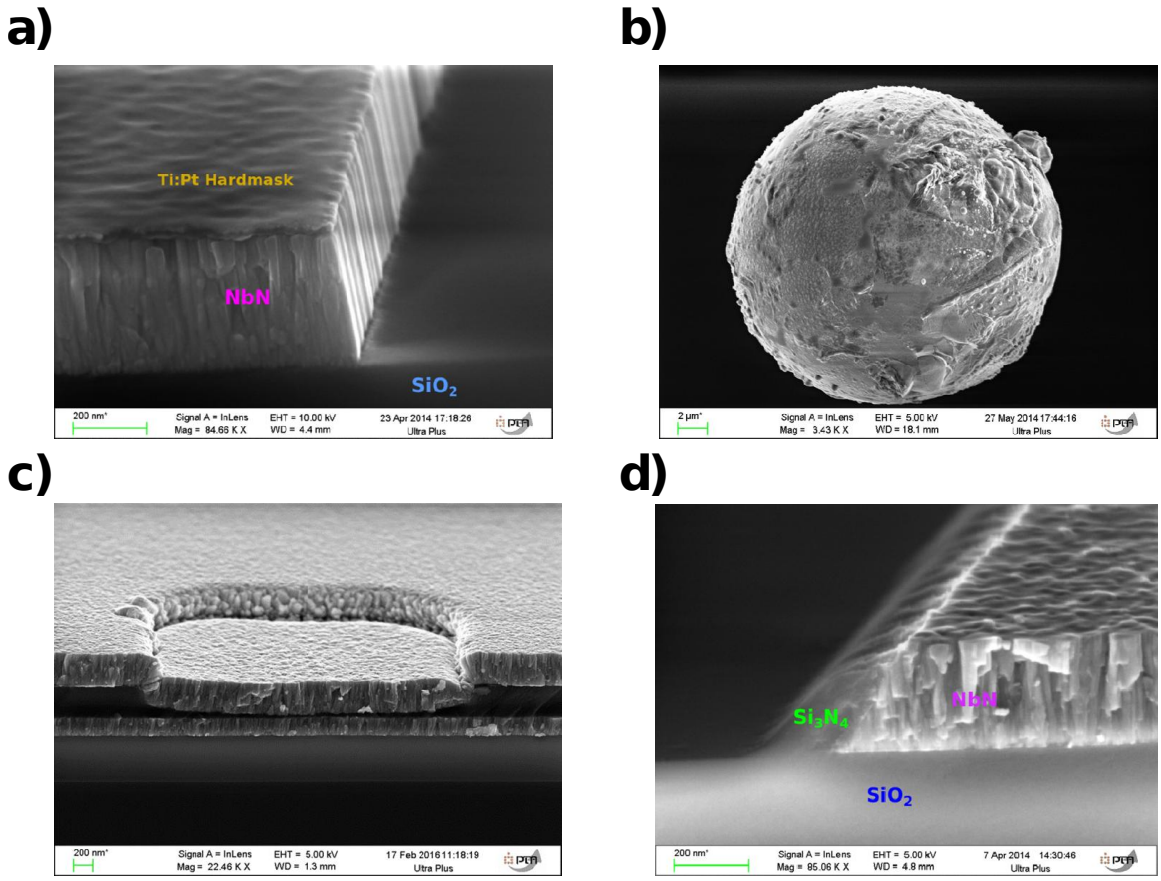

Figure 5.8 **Technical problems and solutions:** **a)** SEM micrograph of the trilayer etching step using a Ti(10 nm)/Pt(60 nm) hard-mask. **(b)** Aluminum-platinum balls. **(c)** SEM micrograph of a via. The gray color indicates the NbN and the black color indicates the Si_3N_4. **(d)** SEM micrograph of the dielectric etching step keeping the spacers.

mask "exploders". However it falls down on the top of the wafer as balls (Figure 5.8.b). On top of NbN, there seems to be sufficient heat conduction to prevent a chain reaction; so that, a standard lift-off (within μs) is effectively produced but the residues of the mask remain on the top of the devices. Finally, we settled for a very thick Al mask (150 nm) accepting some faceting.

Spacer etching During the dielectric Si_3N_4 etching we managed to find a good compromise between, on the one hand, the building of spacers on both sides of Josephson junctions to protect the trilayer from the top-electrode, and on the other hand, the opening of vias in our CPW. To do so, we have to optimize the etching time of the dielectric to keep spacers which resist during the next steps of our fabrication process (see figure (5.3.d)) but we also have to open completely the vias (5.3.c)). For that purpose, we add a second step of etching "overetch" with a soft plasma of mixtures'CH_2F_2, SF_6' during 45 s to clean the bottom of the vias. In addition we etch the dielectric on ground planes to avoid inhomogeneities in the etch rate due to non-uniformities in the design (macro-loading). Note that this point is not completely optimized.

5.2 Method of sample selection

When the fabrication process of our devices is completed, all the chips are electrically probed on the wafer through test structures to determine which chips are functional before measuring them at low temperature. This selection is reached by two steps: the first one is the room temperature measurement using a probe-station and the second one is the 4.2 K measurement using an helium bath cryostat.

5.2.1 Josephson junction test

To simplify the selection of functional samples, we include on the center of each chip several test Josephson junctions, five of them defined by optical lithography with sizes: 1x1, 1x3, 1x10, 3x10 and 10x10 μm^2 as shown in figure (5.9.a). Another reason to include these structures is to check the uniformity of the film deposition over the wafer as well as to check the reproducibility of our fabrication process.

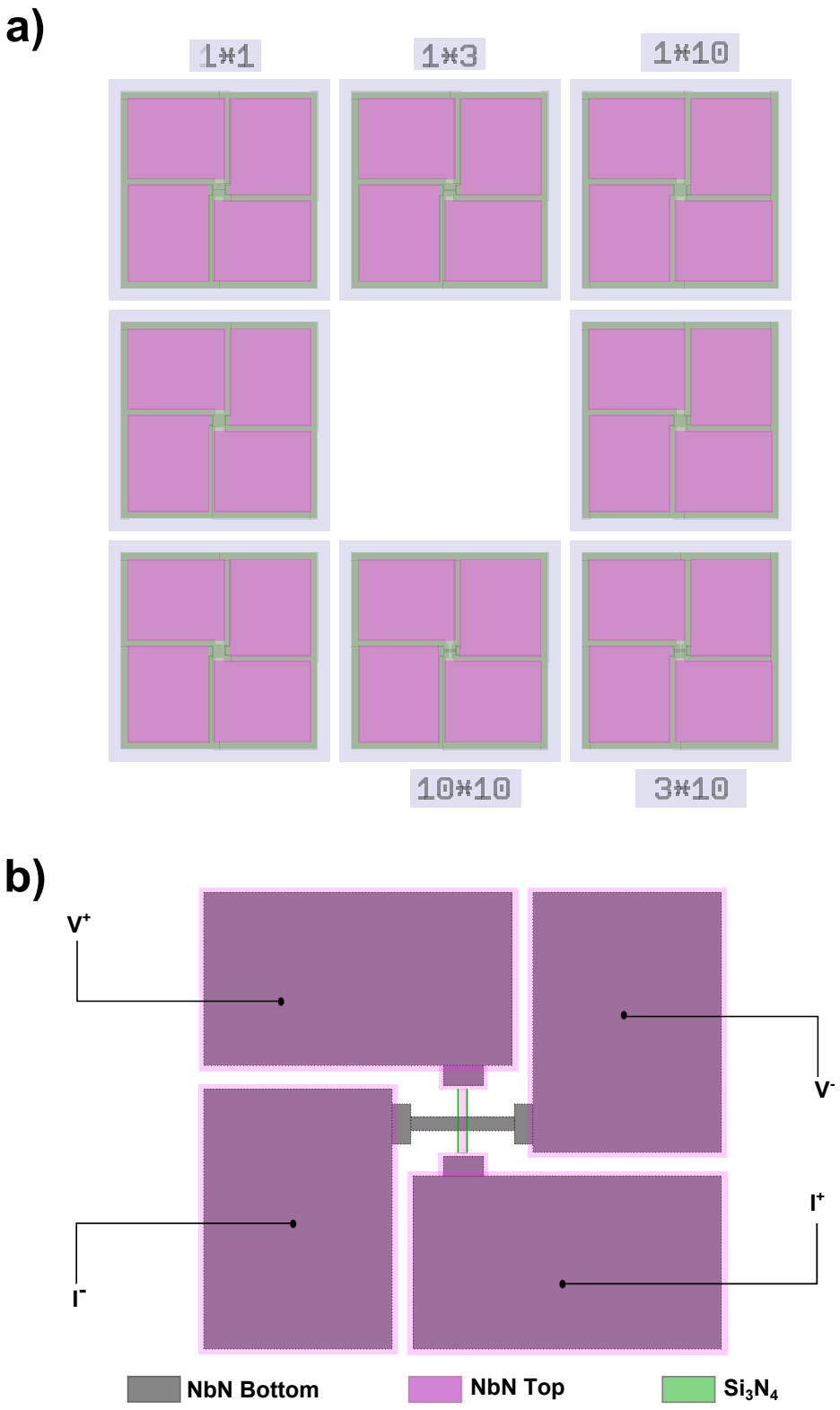

Figure 5.9 **Josephson test junctions: (a)** Layout of eight Josephson test junctions, five of them are made by optical lithography steps (1x1, 1x3, 1x10, 3x10 and 10x10 μm^2) and three of them are made by electron beam lithography setps, their sizes are fixed during the fabrication process according to needs. **(b)** Representation of a Josephson junction; the gray regions represent the trilayer, the pink regions represent the top wiring and the green lines represent spacers. The four-wire measurement method is indicated by arrows.

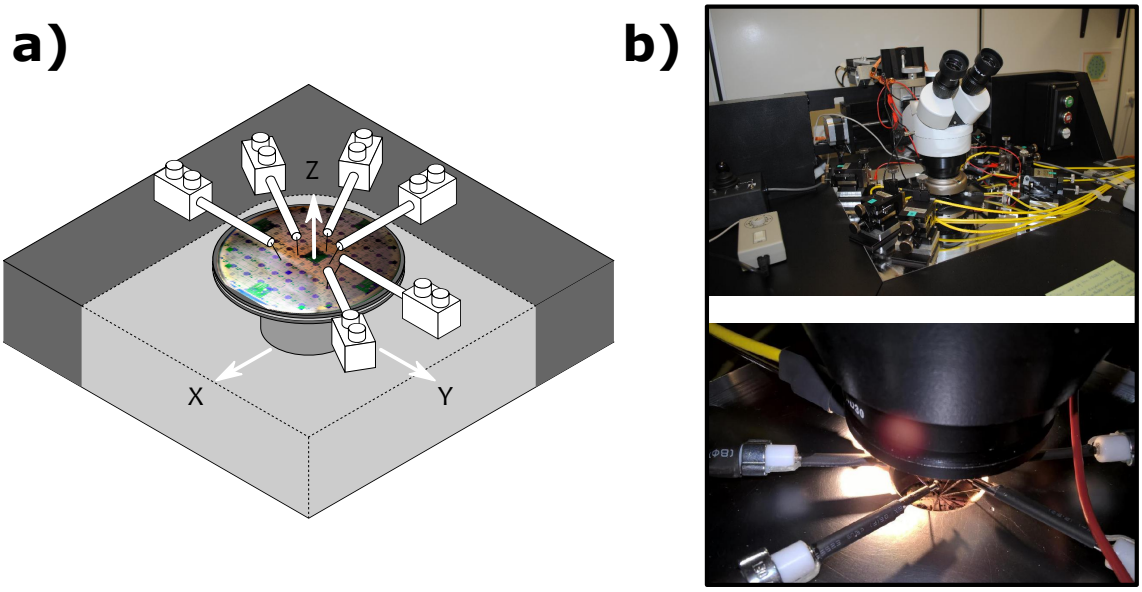

Figure 5.10 **Probe-station: a)** Schematics of the probe-station with a photograph of our wafer on the center. **b)** Photographs of the probe-station

5.2.2 300K measurement: Probe-station

In this section, we introduce the room temperature part of our experimental setup (see figure 5.10). In this stage, the resistivity of junctions is measured using four-wire measurements on test junctions (see figure (5.9.b)). After the data analysis, we draw maps showing the results. Figures (5.11.d), (5.11.e) and (5.11.f) summarize the measured resistances, respectively, for Josephson test junctions with sizes 1x10 μm^2, 3x10 μm^2 and 10x10 μm^2. We clearly see that the resistance on the right side of the wafer is higher than the resistance on the right side. This is because the film deposition is not uniform. In fact, the MgO film on the right side of the wafer is probably thicker than on the left side. We choose the best candidate to measure the I-V characteristic of the junction included in the real sample at 4.2 K.

5.2.3 4K Measurement: Helium bath cryostat

One of many advantages to use niobium nitride as superconductor is its high critical temperature ($\approx$ 16 K) which gives us the opportunity to measure our samples in a helium bath cryostat at 4.2 K using a simple cryogenic setup presented in figure (5.12). The cooling power is provided by evaporation of the liquid helium. Our goal is to test if our junction works and to determine its critical current by measuring its I-V characteristics (see figure (5.5)). We also check if the resonance frequencies of our resonators are correct by measuring

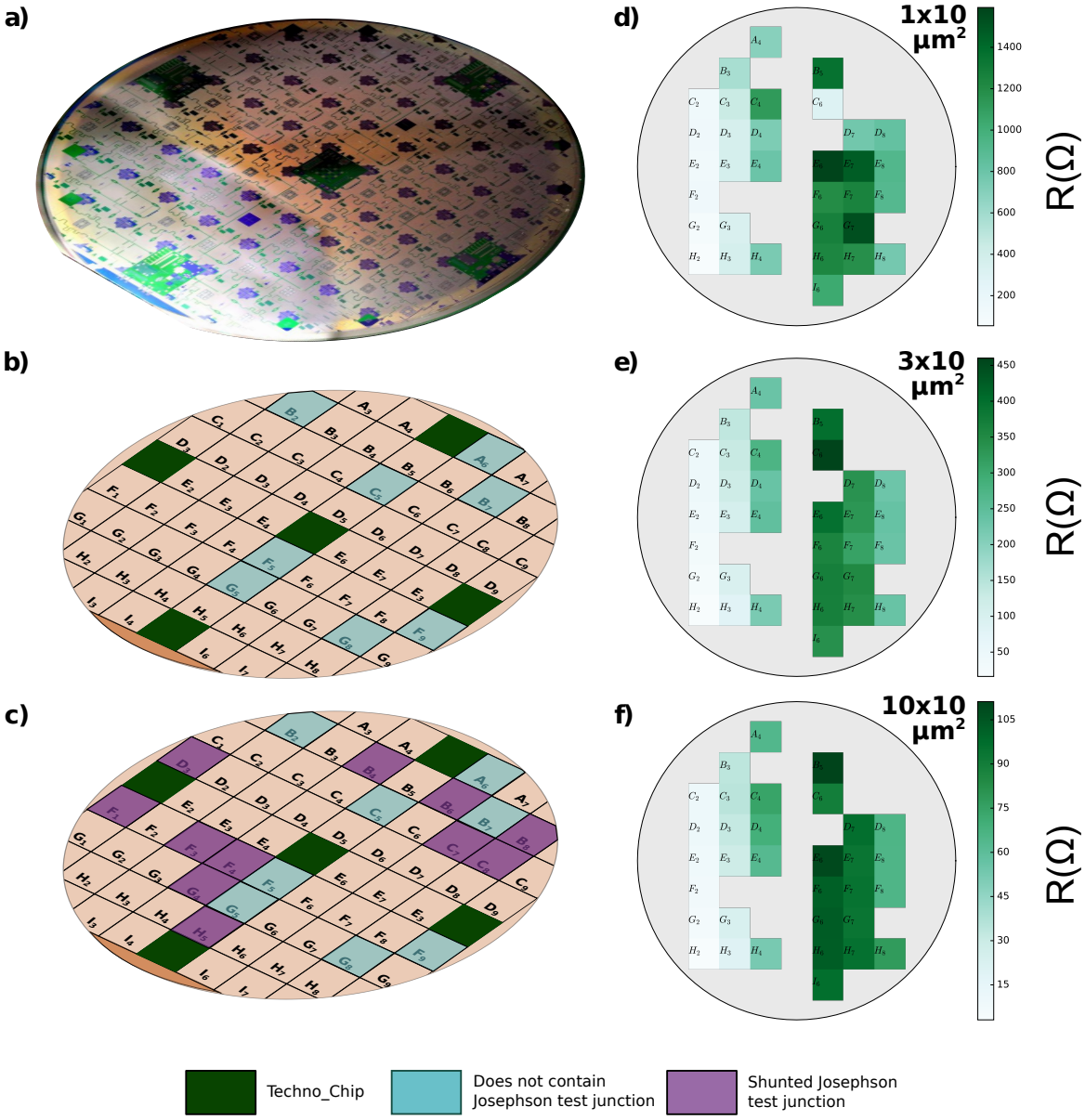

Figure 5.11 **Methode of sample selection: a)** Photograph of the wafer after the fabrication process is completed. **b)** Representation of the wafer indicating the techno-chips (black square) and the chips don't containing test structures (blue square). **c)** Representation of the wafer indicating shunted test junctions (violet square). **d)** Map showing the measured resistances of junctions 1x10 μm^2. **e)** Map showing the measured resistances of junctions 3x10 μm^2. **f)** Map showing the measured resistances of junctions 10x10 μm^2.

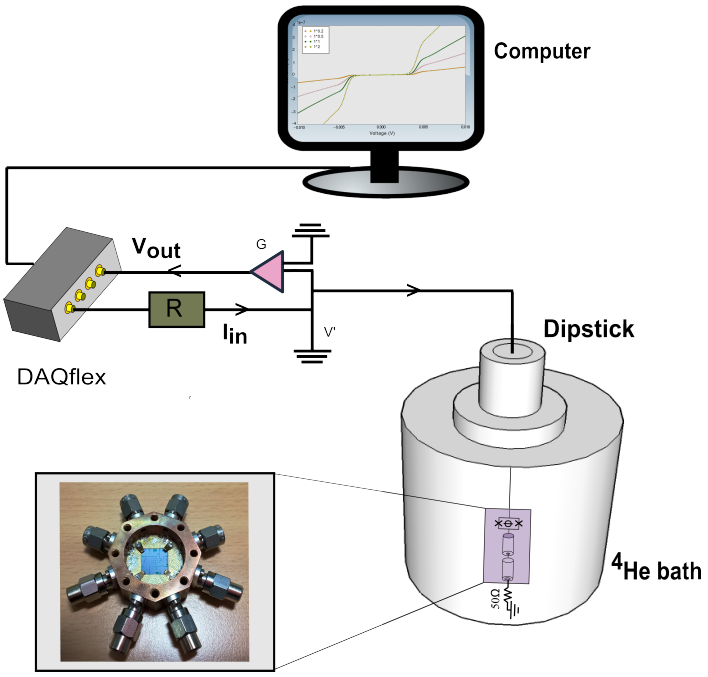

Figure 5.12 **Helium bath cryostat:** Setup for measuring the Josephson junctions and the resonators at 4.2 K. The samples are bonded to a PCB and placed inside a pumped dipstick. The whole is emphasized in a cryostat filled with liquid helium.

the reflection coefficient S_{11} of the scattering matrix using a VNA (see figure (5.7)).

In order to measure the I-V characteristics of our junctions we use a Measurement computing USB-1608GX-2AO analog I-O card. We apply a current using a large resistor R and measure the voltage accross the junction. Finally, we plot the current $I = \frac{V_{in} - V'}{R}$ as a function of the volatge a cross the junction $V' = \frac{V_{out}}{G}$. Where G is the gain of the pre-amplifier.

Conclusion

In this chapter, we have described the fabrication process for vertical Josephson junctions made from niobium nitride and magnesium oxide. Then, we discussed their superconducting properties. We presented also the fabrication of the coplanar wave guides used in this work and their proprieties. We concluded this chapter by presenting how we probe the samples to find the best candidates for measurements at low temperature which we will present in the next chapter.

Chapter 6

Second generation of the ICTA Samples based on NbN superconductor

In this chapter, further experimental results for the ICTA samples based on niobium nitride are presented. Two of the designed devices show how the ICTA gain and noise can be improved:

- The first sample called (S_{2b}) is presented in section (4.3.2). Here, we discuss how the ICTA performance such as the gain and the dynamic range depend on the Josephson energy. We prove that by tuning the E_J parameter, the ICTA gain can be adjusted to a desirable value which is typically 20 dB.
- The second sample called (S_{4b}) is presented in section (4.3.3). Here, we show that by suppressing the down-conversion process and voltage noise, we can reduce the ICTA noise down to the quantum limit.

6.1 Improvement of the ICTA gain

As mentioned above, the design of this sample (S_{2b}) and its impedance seen by the SQUID are presented in section (4.3.2). The devices presented in this chapter are fabricated from niobium nitride. This gives the opportunity to test them at 4.2 K, as explained before in chapter (5). The resonator is designed to have $f_0 \approx 6$ GHz with a full width at half maximum of 1 GHz. Higher modes of the resonator appear at $f_n \approx (2n+1)f_0$ ($n = 1,2,,..$). The S_{11} coefficient measured at 4.2 K shows that the resonance frequency of the resonator is $f_{0,measured} \approx 4.17$ GHz, shifted by 1.83 GHz from the design value. This frequency shift is explained in section (6.3). The normal resistance $R_N \approx 11.3$ kΩ, and the gap voltage $2\Delta/e$

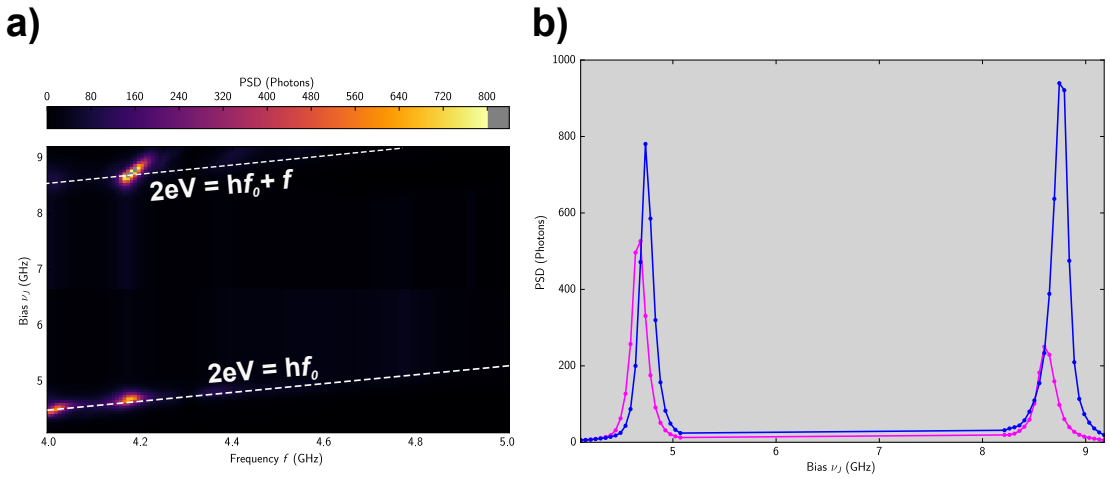

Figure 6.1 **The power spectral density: a)** The PSD as function of the voltage bias ν_J and the frequency f at flux bias Φ = -0.1Φ_0. To facilitate the interpretation of the data, the voltage axis is converted into frequency via the relation $\nu_J = 2eV/h$. The dashed white lines show the one photo and two photon process: **b)** The PSD as function of the voltage bias at signal frequency f= 4.18 GHz for two different values of flux bias Φ = -0.1Φ_0 (blue) and Φ = -0.22Φ_0 (magenta).

$\approx$ 5.02 mV, are determinated through the I-V characteristic of the SQUID measured at 4.2 K and allow us to estimate the critical current at zero temperature, $I_0 \approx 1.4\ \mu$A, via the Ambegaokar-Baratoff formula. This sample is similar to the device studied in chapter (3), but here we increased the bandwidth of the resonators to reduce the voltage noise and the Josephson junction size in the interest to increase the ICTA gain.

6.1.1 Power spectral density

We have measured the power spectral density (PSD) of the emitted radiation as a function of the signal frequency f and the voltage bias ν_J converted into GHz at a fixed E_J corresponding to a flux bias $\Phi = -0.1\Phi_0$. As can be seen in figure (6.1.a), we observe two peaks that correspond to the one and two photon processes respectively at $\nu_J \approx 4.67$ GHz and $\nu_J \approx 8.74$ GHz are observed. A cut of the PSD at signal frequency $f \approx 4.18$ GHz for two values of the Josephson energy is plotted in figure (6.1.b). It can be noticed that when E_J is increasing, the peaks appear at a higher bias voltage: when E_J is increased, a high current flows that causes a voltage drop on the terminal of the junction. The finite width of the peak corresponding to one Cooper pair emitting one photon is approximately 150 MHz for a flux bias Φ = -0.1Φ_0. The finite width of the peak corresponding to one Cooper pair emitting two

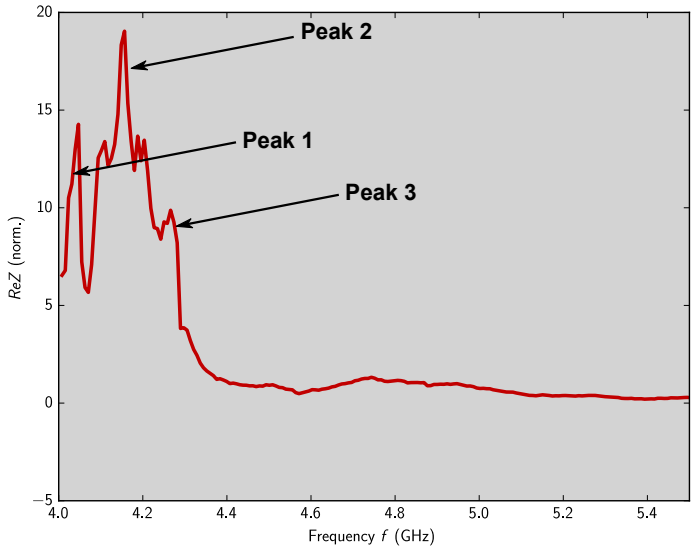

Figure 6.2 **The real part of the impedance seen by the junction:** The Re$Z(f)$ as function of the frequency f extracted from the PSD measurement shown before.

photon is 210 MHz.

At a low Josephson energy and from the one photon peak, we can extract the real part of the impedance seen by the SQUID Re $Z(f)$ as a function of the signal frequency (see section (6.3) as shown in figure (6.2). The Re $Z(f)$ is different than what we designed and presented in section (4.3.2). We observe several peaks: the first one at $f \approx 4.01$GHz, the second one at $f \approx 4.17$ GHz and the third one at $f \approx 4.28$ GHz. This is explained by the reflected standing waves in the RF line connecting the sample holder to the circulators and band pass-filter, which are not well impedance matched at 4 GHz, the lower limit of their pass band.

6.1.2 Flux modulation

By tuning the Josephson energy E_J of the SQUID, the ICTA gain is easily tuned (chapter (1)). Thus, we need to know the value of the flux bias of the SQUID. This can be found directly by measuring the PSD on a given emission peak as a function of the current applied to the flux line. Figure (6.3.a) and figure (6.3.b) show the power spectral density as a function of the signal frequency and the calibrated flux bias in units of the flux quantum Φ_0, respectively for the one photon process ($2eV = hf_0$, ν_J = 4.58 GHz) and the two photons processes ($2eV = hf_0$, ν_J = 8.64 GHz). To better compare the gain versus the noise between the one and the two photons processes, we plotted the flux variation for these two processes in the

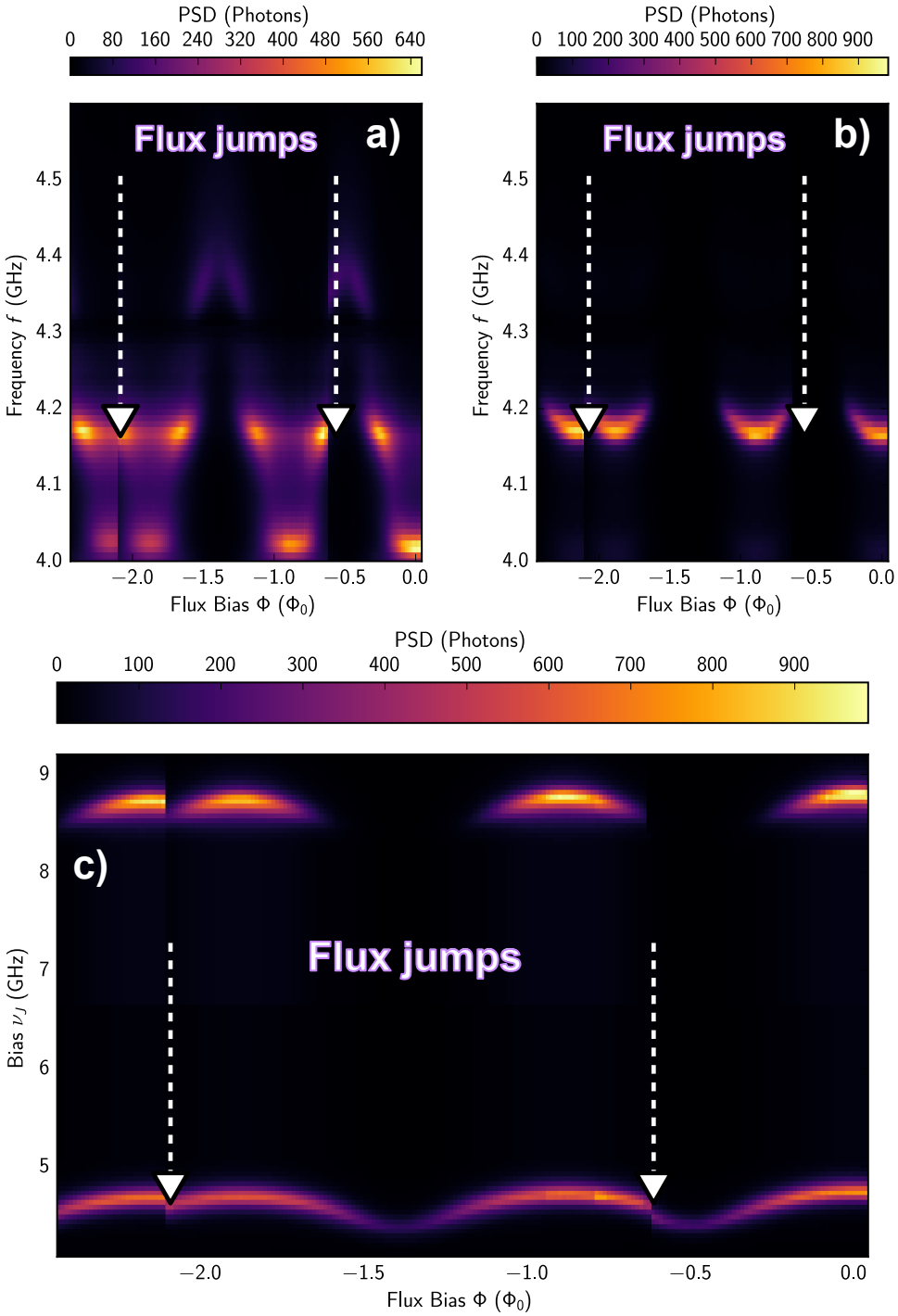

Figure 6.3 **Flux modulation** The power spectral density as a function of the flux bias Φ and the frequency f at voltage biases **a)** $\nu_J = 4.58$ GHz around one photon process **b)** $\nu_J = 8.2$ GHz around two photons process. **c)** The power spectral density as function of the voltage bias ν_J and the flux bias Φ at a frequency $f = 4.18$ GHz. The dashed white lines show where the flux jumped.

same figure. For that, the signal frequency is fixed around the resonance frequency $f \approx$ 4.18 GHz and we measure the PSD as a function of the voltage bias v_J and the flux bias applied to the flux line (figures (6.3.c)). We observe that the flux jumps two times (White dashed lines). These jumps are probably due to the fact that in order to thread several flux quanta through the SQUID loop, higher fields are generated close to the flux loop (see figure 4.1.1) generating vortices, which then change the flux through the SQUID loop. Sudden dramatic reductions of the maximum critical current have even be observed which we were able to reverse by heating up the sample. We attribute them to vortices in one of the junctions. However, note that for typical measurements the flux is limited to $\pm\frac{1}{2}\Phi_0$ where flux jumps are very rare.

6.1.3 ICTA gain

In figure (6.4.a) we plot the ICTA gain as a function of the signal frequency f and the bias voltage v_J at flux bias $\Phi \approx 0.74\Phi_0$. A cut of this data in the one photon ($v_J \approx 4.6$ GHz) and the two photon ($v_J \approx 8.8$ GHz) peaks for different values of the flux threading the SQUID are shown respectively in figure (6.4.b) and figure (6.4.c). By tuning the Josephson energy, the gain G is adjusted to the desired value which is typically about 20 dB. When the gain is increased, the band of amplification becomes narrower. This is quantitatively expressed by the gain-bandwidth relation where G is inversely proportional to the bandwidth of the amplifier. This is a very general relation for parametric amplifiers, which still hold in our case. It should be noted that the gain is higher in the two photon process than in the single photon process, for the same flux bias. The highest measured gain for the single photon process is 15 dB. However, it is more than 20 dB for two-photon process, even though we are not able to reach parametric oscillation. In the next section we compare between these two processes also in terms of added noise.

6.1.4 ICTA noise

When operating the ICTA, we also have to understand its behavior in terms of added noise for both one and two photon processes. In this section, we compare the trade-off between gain and noise for the one and two photon processes at the same frequency. In figure (6.5.a), we plot the ICTA gain for the one photon process ($2eV = hf_0$) as function of the signal frequency f for three different flux biases. The associated noise curves are plotted with the same color in figure (6.5.b). The same quantities for the two photon process at the same frequency ($2eV = 2hf_0$) are shown respectively in figures (6.5.c) and (6.5.d). For the maximum flux bias, 20 dB of gain and 2.5 photon are measured in two photon

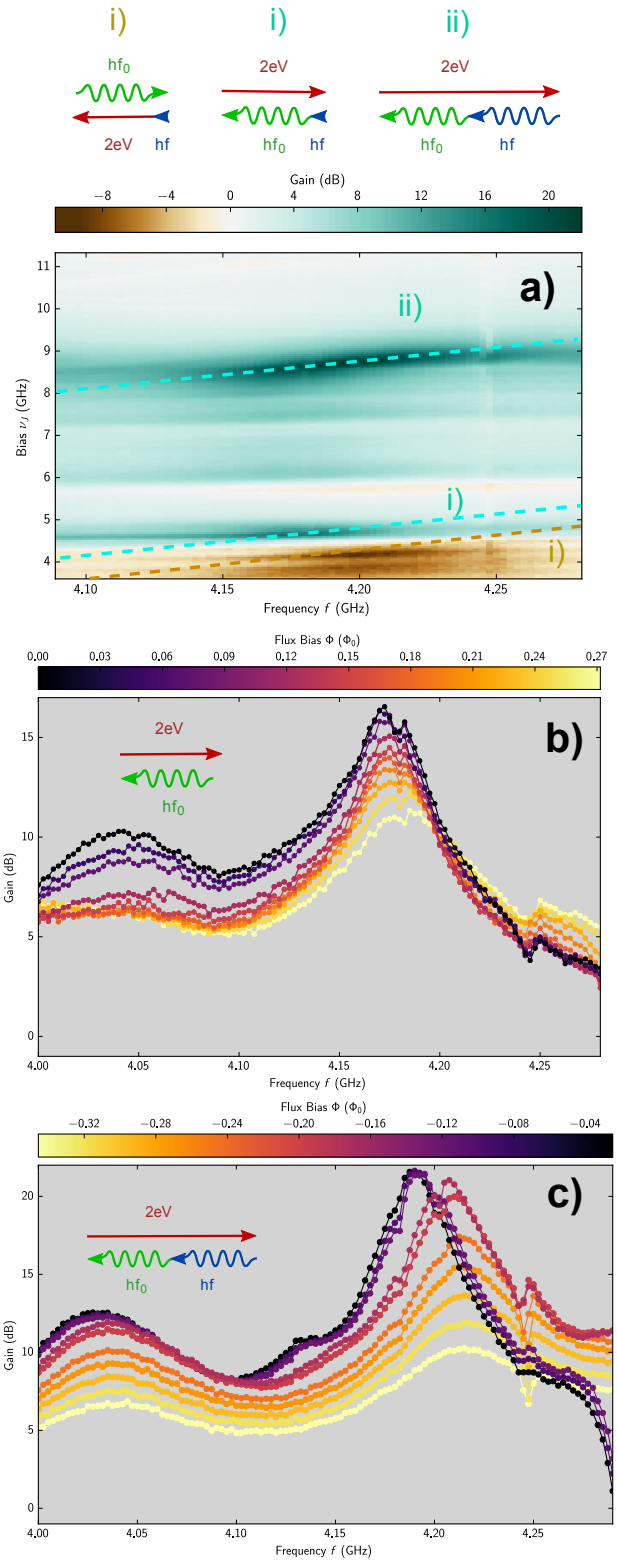

Figure 6.4 **The ICTA gain: a)** The gain as a function of the voltage bias ν_J and the frequency f for a flux bias Φ = -0.04Φ_0. The green lines show the amplification processes. The brown lines show the conversion process **b)** The ICTA gain as a function of the frequency at the resonance condition of the one photon peak at ν_J = 4.6 GHz for various flux biases. **c)** The ICTA gain as function of the frequency at the resonance condition of the two photon peak at ν_J = 8.8 GHz for various flux biases.

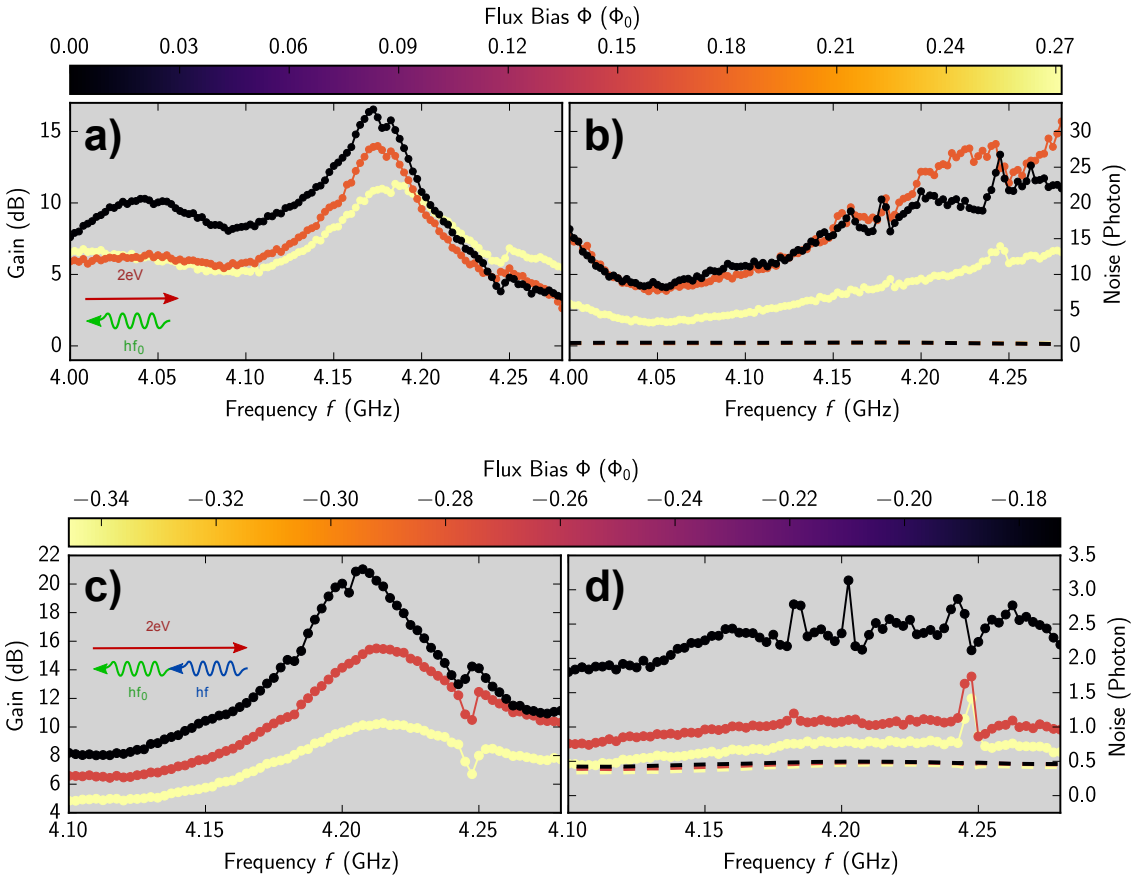

Figure 6.5 **The ICTA noise: a)** The ICTA gain as a function of frequency for different flux biases $\Phi = 0, 0.16\Phi_0, 0.27\Phi_0$ at the one photon process. **b)** The ICTA noise as function of the frequency for the same values of flux bias at the one photon process. **c)** The ICTA gain as a function of the frequency for different flux biases Φ = -0.18Φ_0, -0.27Φ_0, -0.35Φ_0 at the two photon process. **d)** The ICTA noise as a function of the frequency for the same values of flux bias at the two photon process.

process. However, for the single photon process, 16.7 dB of gain and 16.4 photons of noise are measured. These results are perfectly understandable: for the single photon process, the idler mode can be seen at low frequencies as one of the modes of the dissipative shunt of the junction. In contrast, for the two photon process, the idler mode is fixed at a frequency $f \approx 4$ GHz. In this case $\hbar f_i \ll k_B T$, so that the added noise is lower.

6.1.5 Saturation power of ICTA

In figure (6.6), we plot the ICTA dynamic range: the gain versus the input power for different flux biases Φ = -0.24Φ_0, -0.74Φ_0, 0.24Φ_0, 0.74Φ_0 and 0.98Φ_0. The ICTA gain

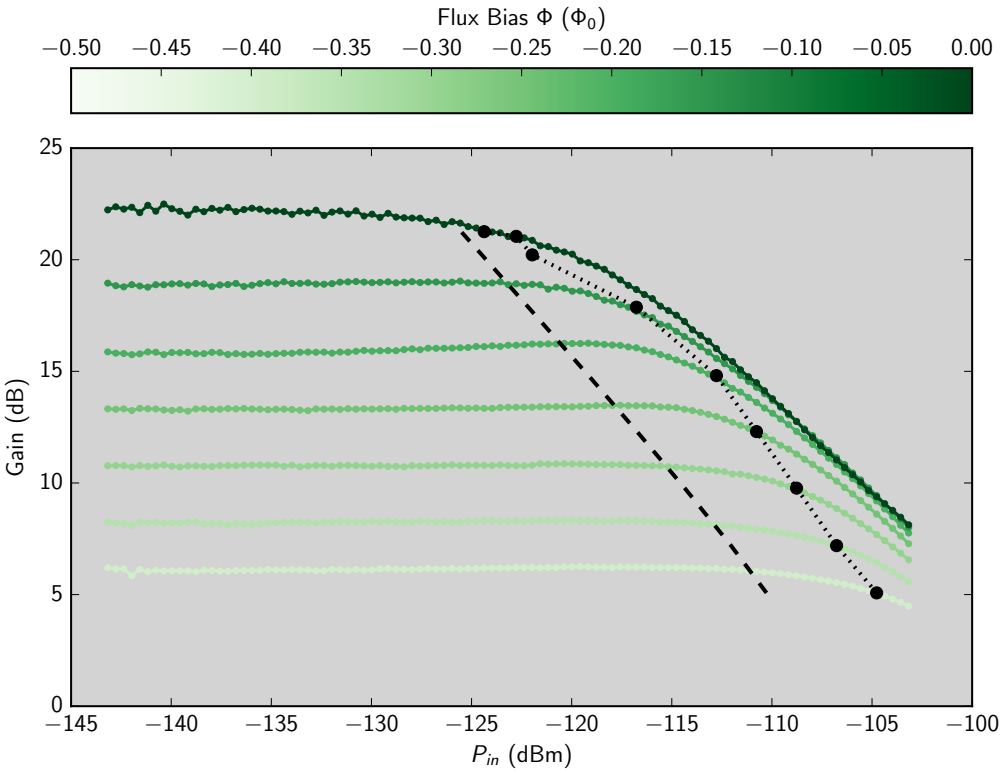

Figure 6.6 **The ICTA dynamic range:** The ICTA gain as function of the input signal power for different flux biases. The dotted line represents the -1 dB compression points, the dashed line the theoretical limit (see text).

is constant for small input powers and drops at larger powers. As becomes evident, the saturation power decreases with increasing gain. A typical value of -118 dBm for 21 dB of gain is found. The reduction in dynamic range is expected: when the Josephson energy is tuned in order to increase the gain, the output signal amplitude increases for fixed input signal amplitude. As in the case of the JPA and JPC [40], the 1dB compression point scales approximately as $1/G$(at least at low gain). The dashed line indicates when $2eV_{in,ac} \approx hf$, the limit at which nonlinearities in the signal amplitude become important (see chapter 1). The right scaling (at least at low powers) is observed but the actual compression points are higher than these values. In figure (6.7), the measured saturation power as a function of the gain for different working points of the ICTA are shown.

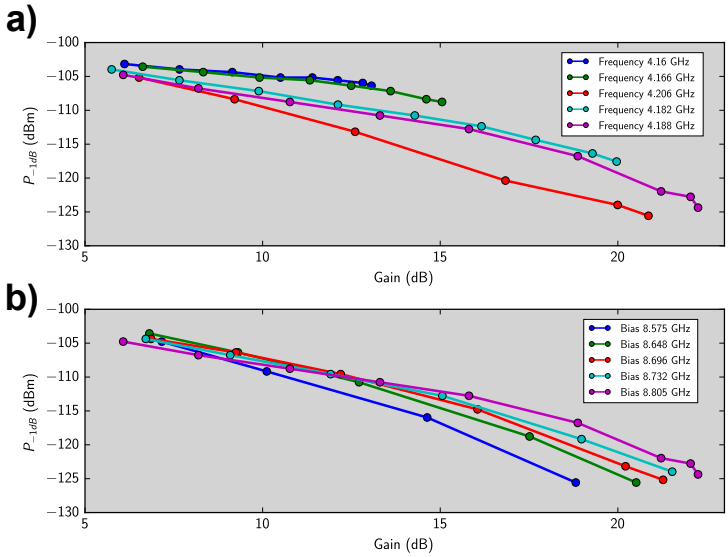

Figure 6.7 **The -1 dB compression point: a)** Measured P_{-1dB} as a function of the gain for different frequency points at $\nu_J = 8.8$ GHz. **b)** Measured P_{-1dB} as a function of the gain for different voltage points at $f = 4.88$ GHz.

6.2 Improvement of the ICTA noise

The design of sample (S_{4b}) studied here is discussed in section (4.3.3). From the I-V characteristics of the SQUID, measured at 4.2 K, we have extracted the theoretical critical current at zero temperature $I_0 \approx 0.97\ \mu$A from the normal resistance $R_N = 12\ k\Omega$ and the gap voltage $2\Delta/e \approx 5.07$ mV. The resonator seen by the junction was designed to have $f_0 \approx 6$ GHz with a full width at half maximum of 1 GHz. From the measured reflection coefficient S_{11} at 4.2 K, we determine the resonance frequency of the resonator around $f_{0,measured} \approx 4.2$ GHz, significantly lower than the design value.

6.2.1 Power spectral density

In this paragraph, first, we examine the power spectral density (PSD) of the emitted photons. The measured PSD in units of photons as a function of the signal frequency and the Josephson frequency ν_J is presented in figure (6.8). At low Josephson energies (figure(6.8.a)), we see a single peak corresponding to the one photon process $2eV = hf_0$. A dataset recorded at a high Josephson energy E_J is presented in figure (6.8.b) in order to observe the higher order processes. The plot shows four emission peaks:

- The first peak at a bias voltage V such that $3 \times 2eV = 1 \times hf_0$ i.e. three Cooper pairs emit one photon at a frequency $f \approx f_0$.

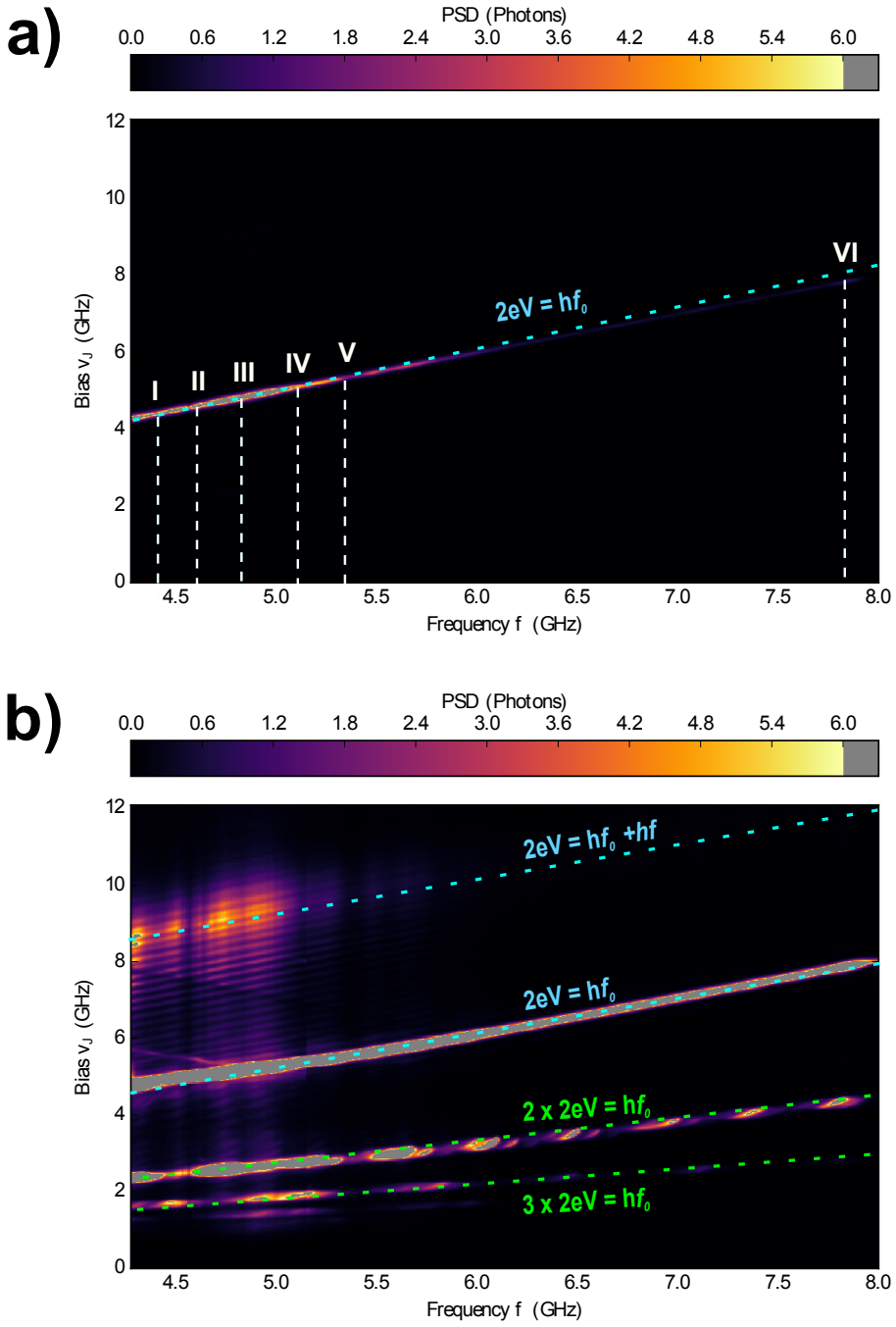

Figure 6.8 **Power spectral density:** The PSD as a function of the signal frequency and voltage bias. **a)** for low Josephson energy. The dashed lines show cuts at different frequencies f used in figure (6.11). **b)** for high Josephson energy. The green lines corresponding to the quartet and the sextet processes have, respectively, slopes of 2 and 3. The blue lines corresponding to the one and two photon processes have slopes of ≈ 1.

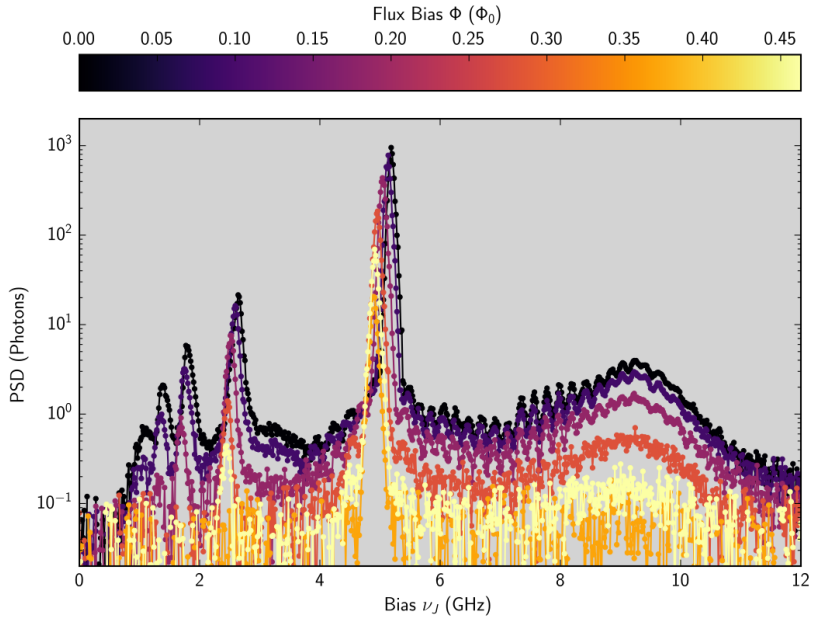

Figure 6.9 **The power spectral density for various E_J:** The PSD as a function of the voltage bias ν_J and the frequency f in logarithmic scale for different E_J.

- The second peak at a bias voltage V such that $2 \times 2eV = 1 \times hf_0$ i.e. two Cooper pairs emit one photon at a frequency $f \approx f_0$.
- The third peak at a bias voltage V such that $1 \times 2eV = 1 \times hf_0$ i.e. one Copper pair emits one photon at a frequency $f \approx f_0$.
- The fourth peak at a bias voltage V such that $1 \times 2eV = 2 \times hf_0$ i.e. one Copper pair emits two photons at a frequency $f \approx f_0$.

Dashed lines on figure (6.8.b) indicate these four processes. The green lines corresponding to the first and the second peaks have, respectively, slopes of 2 and 3. The blue lines corresponding to the third and the fourth peaks and have slopes of ≈ 1. The photon emission measured at a fixed signal frequency f = 4.9 GHz for different flux biases (varying E_J), while the bias voltage is swept, is plotted in figure (6.9). In order to better observe the two photon process, we plot this quantity on a logarithmic scale. When the E_J is increased progressively, the current due to the tunneling Cooper pairs becomes large enough to cause a considerable voltage drop over the bias circuit with a DC impedance of 50 Ω. This explains why the peak is shifted to higher values of the voltage bias. The finite width of the peak corresponding to one Cooper pair emitting one photon is approximately 100 MHz. It is a

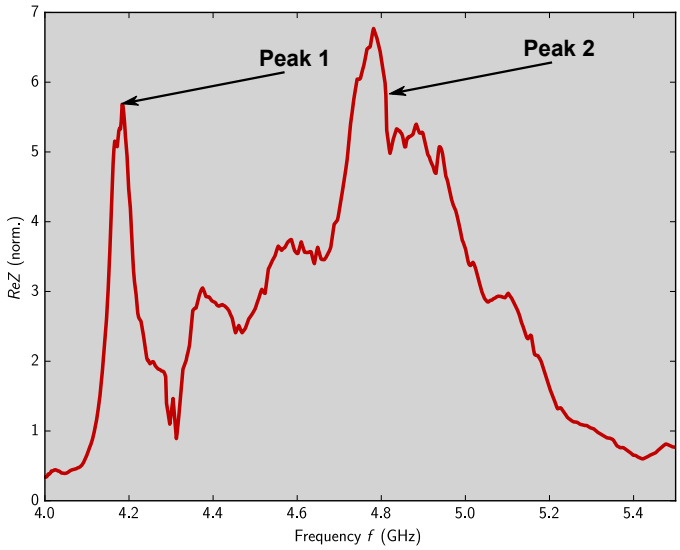

Figure 6.10 **The real part of the impedance seen by the junction:** The Re$Z(f)$ as a function of the frequency f extracted from the PSD measurement shown before.

measurement of the fluctuations of the voltage bias at the sample. The width of two photon peak is approximatively 1.2 GHz corresponding to the resonator bandwidth. This is the case because at a given voltage bias, the two emitted photons can compensate for each other in frequency within the bandwidth of the resonator. In fact, if there was no voltage noise, the only value of the bias voltage giving a signal at the first peak should be exactly at $V = \hbar f_0/2e$. If the width of the first peak was larger than the bandwidth of the resonator, we would obtain high ICTA noise due to the fluctuation of the voltage. This is not the case here because the resonator bandwidth of this sample is around 1 GHz (see section (4.3.3), so that we expect good noise performance. The two-photon process have much lower intensity than the single photon process because of the low resonator impedance.

6.2.2 Extracted sample parameters

In the second step, the flux modulation of the SQUID is investigated. In this part, we are interested in amplification via the two-photon process. However, in order to understand better this physics, some experimental data for the one-photon process are also presented. In figure (6.11), the power spectral density is plotted in units of photons as a function of the signal frequency and the flux bias for several voltage biases around the one photon peak. The white dashed lines in figure (6.8.a) show where the cuts have been made. It is easy to understand that the frequency shift shown in the different plots in the figure (6.11) follows

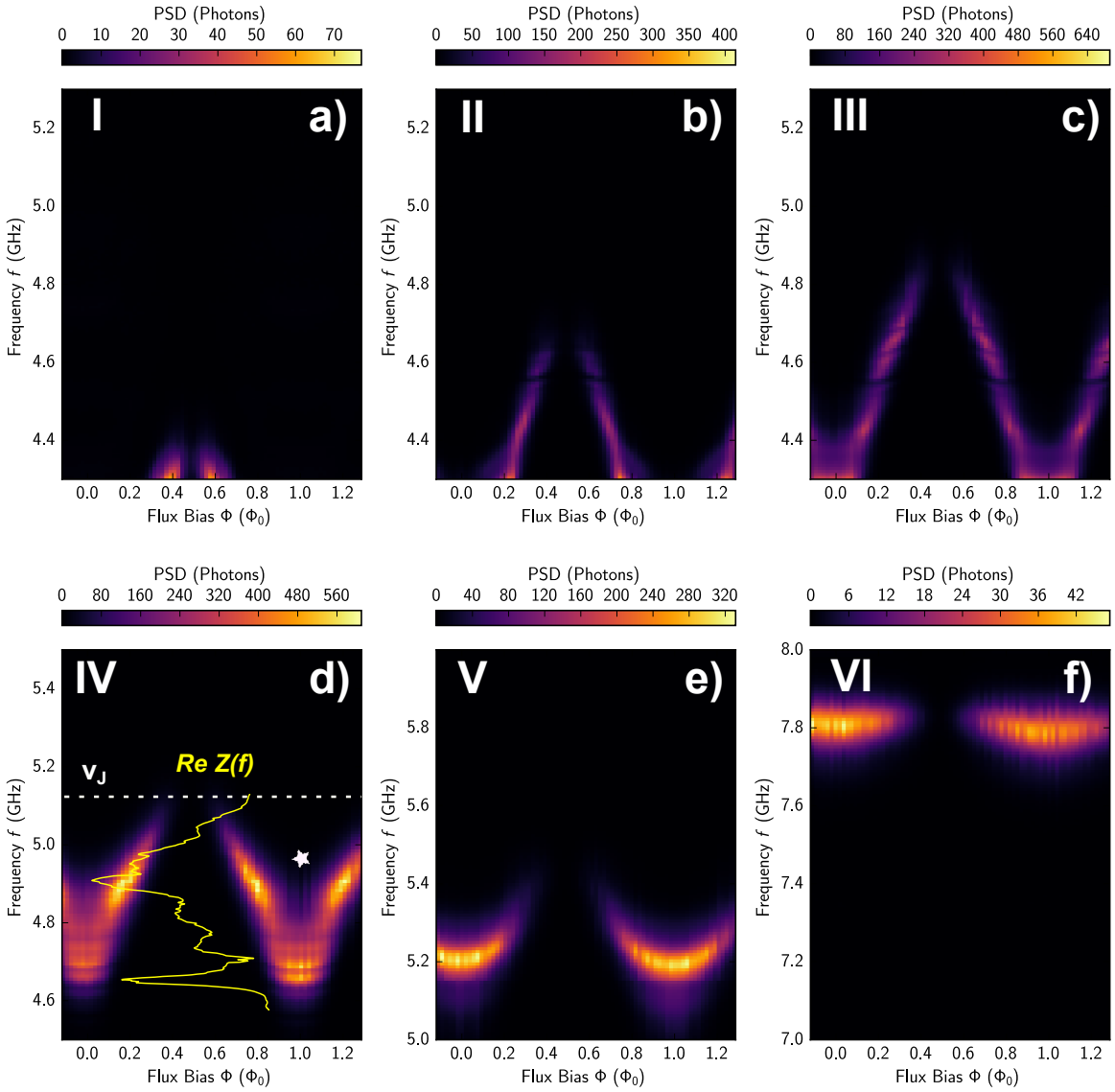

Figure 6.11 **Flux modulation for single photon process:** The power spectral density as a function of the flux bias of the SQUID Φ and the frequency f at different voltage biases **a)** $\nu_J = 4.34$ GHz, **b)** $\nu_J = 4.63$ GHz, **c)** $\nu_J = 4.83$ GHz,**d)** $\nu_J = 5.12$ GHz,**e)** $\nu_J = 5.41$ GHz and **f)** $\nu_J = 7.82$ GHz. In figure (6.8), the dashed white lines show where the cuts are made.

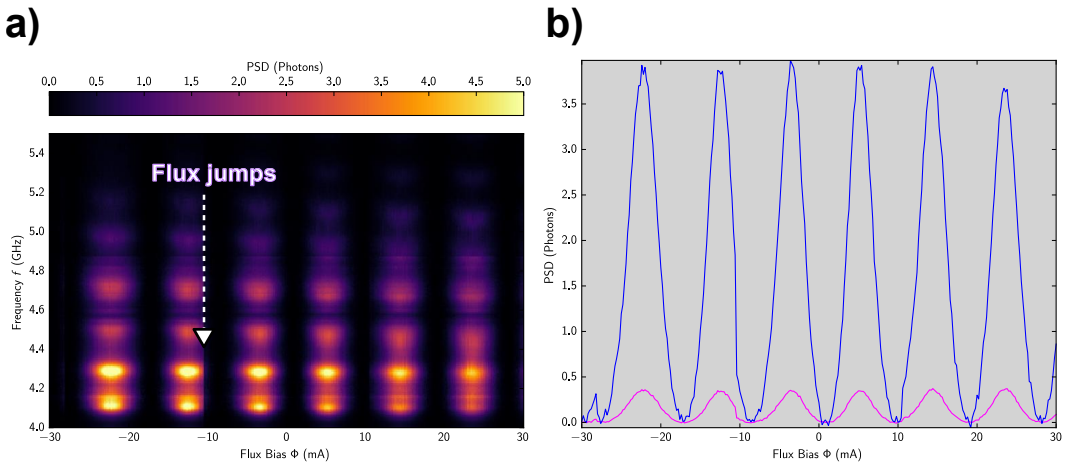

Figure 6.12 **Flux modulation for the two photon process: a)** The power spectral density as a function of the flux bias of the SQUID Φ and the frequency f at a voltage bias $\nu_J = 8.26$ GHz. **b)** Cuts through the power spectral density plots shown in **a)** at two frequencies $f \approx 4.03$ GHz (blue line) and $f \approx 4.25$ GHz (magenta line).

the same slope $2eV{=}hf_0$ of the one photon peak.

It is quite remarkable that the flux modulation at a voltage bias $\nu_J = 5.1$ GHz has a different shape than the flux modulation at a voltage bias $\nu_J = 7.8$ GHz. Here, the shape of the impedance seen by the junction is needed in order to better understand the variation on the flux. For that, the real part of the impedance Re $(Z(f))$ as a function of the frequency is extracted using the method explained below in section (6.3). This is depicted in figure (6.10). We note that the resonance frequency is shifted by 1.75 GHz with respect to the design and that, therefore, we can only measure a small portion of the signal response because of the limitation of our measurement range from 4 GHz to 8 GHz. This plot shows two peaks, the first one at $f = 4.22$ GHz and the second one at $f = 4.79$ GHz, different than what we designed and shown in section (4.3.3). As for the previous sample, we can attribute this to standing waves in the RF line connecting the sample holder to the circulators.

The Re$(Z(f))$ is also shown in figure (6.11.d)(yellow line). We indicate in figure (6.11.d) the Josephson frequency by a dashed white line. It is quite clear that the flux modulation follows the same form as the impedance seen by the SQUID with its two peaks at $f = 4.22$ GHz and $f = 4.79$ GHz. Because the voltage drops over the bias circuit, we observe a dark region, indicated by a white star in figure (6.11.d), when the current is increased.

The PSD as a function of the frequency and the current applied to the flux line for the two-photon process at a fixed voltage $\nu_J \approx 8.26$ GHz is shown over several periods in figure

(6.12). At -11 mA, a flux jump is again observed, probably due to a vortice. The photon emission rate of the two-photon peak as a function of the flux bias at signal frequencies $f \approx 4.03$ GHz and $f \approx 4.25$ GHz is shown in figure (6.12.b). The residual of PSD around maximum frustration is probably due to an imbalance between the two junctions in the SQUID (the SQUID is not perfectly symmetric).

6.2.3 Amplification and conversion processes

The ICTA is operated in reflection mode, as shown in figure (4.4). After the characterisation of the sample through the PSD and the flux modulation measurements, first, the ICTA is operated by applying the RF signal at a frequency f between 4-8 GHz. Then, we measure the reflection coefficient converted to dB at given flux bias (typically zero-current) as a function of the signal frequency and the voltage bias ν_J as shown in figure (6.13.a). Note that this sample is designed to suppress the frequency conversion process and to reduce the voltage noise. As the sample presented in chapter (3), three amplification peaks are observed in figure (6.13.a) in the same regions where we see peaks in the PSD measurement. They correspond to: (i)amplification with one photon process ($\nu_J \approx 4.62$ GHz), (ii)amplification with two photon process at around ($\nu_J \approx 8.43$ GHz) and (iii)amplification in two photon process at two different frequency ($\nu_J \approx 16.43$ GHz). These processes are also marked by green dashed lines. Note that the amplification with the two photon process at the same frequency is much broader than the amplification with the two photon process at different frequencies. This is because in the first case, the two photons are emitted in the same first mode of the impedance seen by the SQUID with large bandwidth. However, in the second case, one photon is confined to the much narrower second mode. This also fixes the frequency of the photon emitted in the first mode. The maximum measured gain for this sample is 15 dB. The conversion process, indicated by a brown dashed line, is quite narrow compared to the sample shown in chapter (3), again because the second mode is narrow. Above this line, the conversion processes is expected to be completely absent because the impedance seen by the junction at $f = 2eV/h + f_0$ is close to zero Ohm.

At the optimal working point ($\nu_J = 8.45$ GHz) we measure the gain for various Josephson energies E_J as a function of the signal frequency as shown in figure (6.13.b). The estimation of the ICTA bandwidth is complicated by two effects: first because of the frequency shift; we can't measure the complete range of the gain. Second because the ICTA gain fluctuates due to the reflected standing waves. If we averge over these oscillations, the ICTA bandwith is more than 500 MHz. But if just one oscillation (between 4.2-4.4 GHz) is considered, the ICTA bandwith is approximately 50 MHz for 9 dB of gain. The explanation for the low value

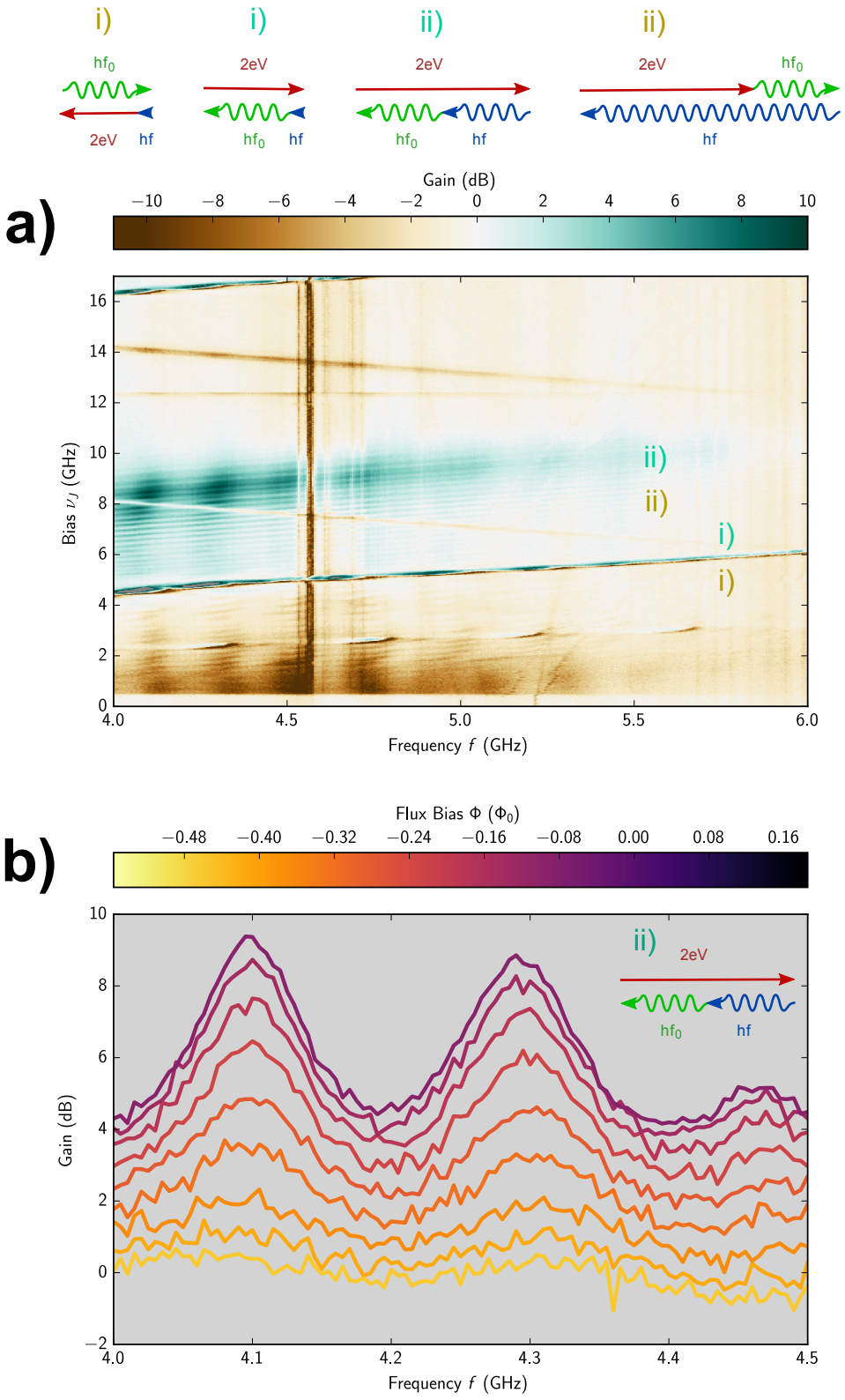

Figure 6.13 **The ICTA gain: a)** Gain as a function of the voltage bias ν_J and the frequency f for a flux bias $\Phi = 0.08\Phi_0$. The green lines show the amplification processes and the brown lines show the conversion processes. **b)** Gain as a function of the frequency f for various flux bias shows the variation of the gain with the Josephson energy E_J.

of the measured gain is that the Josephson energy is not large enough and the real part of the impedance Re $Z(f_s)$ is small. In fact, as we explained in chapter (1), the ICTA gain scales with the Josephson energy but also depends on the characteristic impedance of signal and idler modes as shown in equation (1.34).

6.2.4 ICTA noise

As mentioned in the previous section, we are looking for a two photon process where the idler mode is well defined in order to reduce the noise of this mode associated with thermal photons. In fact, one advantage of our amplifier is that the complementary mode is totally controllable by adjusting the voltage bias. Using the setup shown in figure (2.3) and the calibration method explained in chapter (2), we can measure the input added noise of the amplifier. In figure (6.14.a), the gain is shown as in figure (6.13.a) zoomed on the two photon peak. A cut of this data at a voltage bias ν_J = 8.68 GHz is presented in figure (6.13.c) (blue line). The input added noise (red line) is plotted in the same figure with the quantum limit calculated from the measured gain according to Caves theorem (dashed black line). An added noise less than 1/2 photon is observed. The incertainty in our noise calibration is estimated to be $\pm 10\,\%$ (see chapter (2.3)). The added noise is thus at the quantum limit within measurement accuracy.
This means that three ingredients are united to operate near to the quantum limit:

1. Suppressing the down-conversion process: a parametric amplifier is able to amplify with low noise if it only operates by the amplification term ($a^\dagger b^\dagger c$, in our case $a^\dagger b^\dagger e^{-\omega_J t}$) and oppresses the conversion term ($a^\dagger bc$, in our case $a^\dagger b e^{-\omega_J t}$).

2. Filtering out the voltage noise at low frequencies: the voltage bias plays an import role in our scheme. As explained before, it is the analogue of the microwave pump frequency in PAs physics. Then, in order to reduce the voltage noise, a good filtering at low frequencies is needed. In this sample, a big capacitance (100 pF) is used to cut the impedance seen by the SQUID of 30 MHz. It suppresses thermal noise above this frequency. By comparing the results between the sample presented in chapter (3) and the sample presented here, it can be concluded that the gain must be independent of voltage in the voltage range covered by voltage fluctuations (white bar shown in figure (6.14.b). In other words, the voltage noise must be much smaller than the bandwidth of the gain curve in the sense of the voltage bias. So, in order to reduce the ICTA noise, we have to increase the resonator bandwidth and reduce the voltage fluctuations.

3. Cold idler mode: In order to reduce the thermal noise of the complementary mode, the idler mode is fix at a high frequency. There it is at around 4.5 GHz » $\frac{kT}{h}$. Since niobium nitride superconductor is used and have a very large superconducting gap, the idler mode can in principle be plashed to much higher frequency such that the amplifier can be operated at higher temperatures.

6.2.5 Saturation power of ICTA

In order to determine the dynamic range of the device we plot the gain G as a function of the input signal power P_{input} at frequency f = 4.32 GHz and voltage bias $\nu_J \approx 8.45$ GHz for a flux bias $\Phi \approx \Phi_0$ in figure (6.15). The 1 dB compression point, where the gain is reduced by 1 dB, correspond to -115 dBm.

6.3 Methods and problems encountered

6.3.1 Methods: Extraction of the environment impedance seen by the Josephson junction

In this section, we explain how we extract the real part of the impedance seen by the Josephson junction from the measured power spectral density at a low Josephson energy. The photon emission rate can be written as:

$$PSD(V,f) = \frac{\pi}{\hbar R_Q} E_J^2$$

Re $Z(f)P(2eV - hf)(6.1)P(E_J)$ gives the probability for a Cooper pair to tunnel through the junction, while dissipating its energy E into the environment. This function obeys $\int_{-\infty}^{+\infty}$ P(E)dE = 1, as explained in chapter (1). In this work, we have access to the PSD(V,f) of the photon emission as a function of the applied voltage bias and the frequency f. If, we then integrate over the voltage bias we find:

$$\int_V PSD(f,V)dV = E_J^2 \frac{\pi Z(f)}{\hbar R_Q f} \int_V P(2eV - hf)dV \tag{6.2}$$

The region of the P(E) function around zero dominates. When we measure the 1 photon resonance we have $2eV \approx hf$, so we can approximate the integral over P as 1 and extract the shape of Z(V).

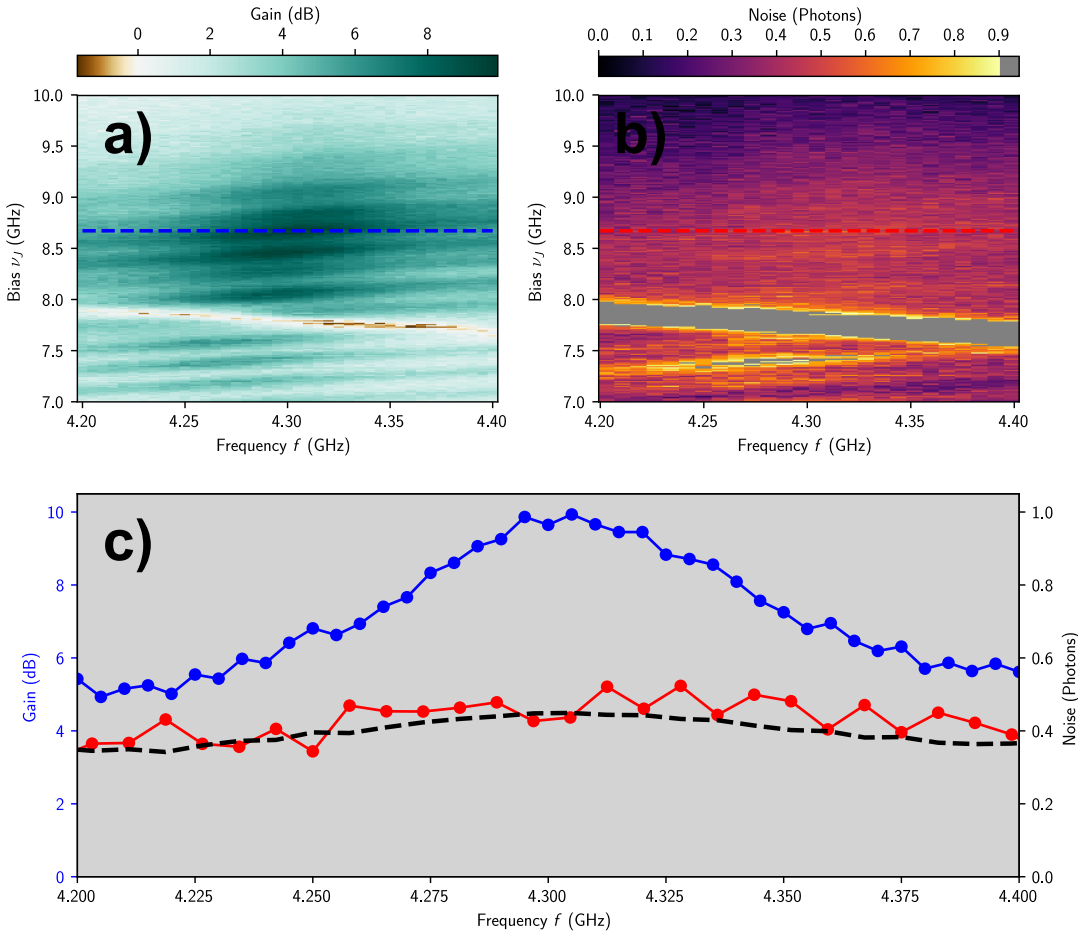

Figure 6.14 **The ICTA noise: a)** The ICTA gain as a function of the voltage bias ν_J and frequency f at a flux bias $\Phi = 0.56\ \Phi_0$, focus on two photon process. **b)** The calibrated ICTA noise as a function of the voltage bias ν_J and the frequency f, focussed on the two photon process. **c)** Cut of **a)** (blue line) and **b)** (red line) at a voltage bias $\nu_J \approx 8.68$ GHz. The quantum limit is calculated from Caves' theorem and plotted as black dashed line.

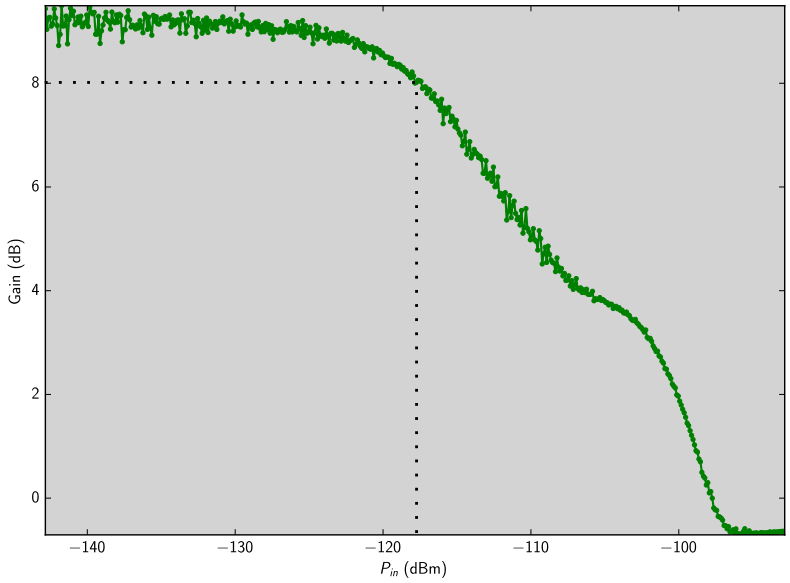

Figure 6.15 **The ICTA saturation power:** The gain as a function of the input signal power P_{in}. The 1 dB compression point, at which the gain drops by 1 dB is a round -118 dBm for 9 dB of gain.

6.3.2 Problems encountered: frequency shift

As mentioned before, the resonance frequencies of our samples are shifted by more than 1 GHz. Due to this shift, all the samples presented in chapter (4) can not be measured because our setup is limited to frequencies between 4-8 GHz. There are two explanations which contribute to the observed shift:

- In sections (6.2) and (6.1), we have shown that the gain of the ICTA scales with the Josephson energy which indicates that a large E_J is desirable for ICTA. However, there is a limitation on the maximal possible value for E_J. In order to increase E_J, the junction surface can be increased, as we did in this work. However this can cause an issue due to the capacitance of the junction which we found to be much larger than anticipated (see the calculation presented in section (5.1.4)). The same simulation presented in chapter (4) has been redone taking in account the capacitance of the SQUID. It shows that a big SQUID composed by the identical junctions (1x2 μm^2) shifts the resonance frequency by 500 MHz.

- Another explanation is the high kinetic inductance of NbN which depends on material quality and thickness of the film. It increases significantly from the center of the wafer to the edges. In addition, during the NbN top wiring etching step, the end point detection is not well controlled. As we use almost the same chemical mixture, to etch

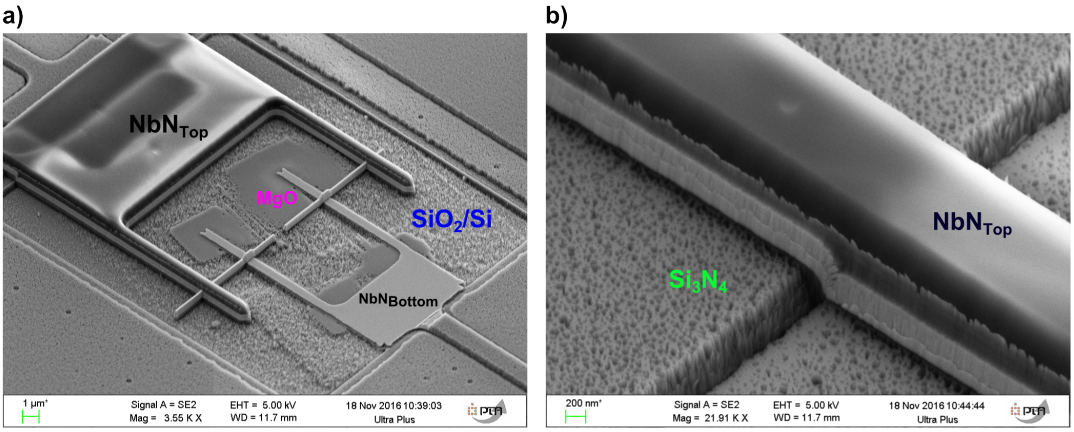

Figure 6.16 **Shift in frequency: a)** SEM image of the entire SQUID. **b)** SEM image around the strap of the transmission line. During the NbN top wiring etching step, the Si_3N_4 not covered by the optical resist is also etched, as well a part of the NbN bottom layer.

both the Si_3N_4 and NbN, we can't selectivly etch these two layers during the final etch of NbN top layer. It can happen that we overetch it, and we remove parts of the dielectric and the bottom layer of NbN. So, the thickness of the transmission lines are slightly modified and the frequencies are shifted due to increased kinetic inductance. In figure (6.16.a) and (6.16.b), we present SEM images after the $NbN_{\text{Top wiring}}$ etching step respectively for the SQUID and close to straps of the transmission line. We can clearly see that parts of the silicon nitride layer Si_3N_4 are also etched. In this case, it is very difficult to control the kinetic inductance of the NbN and so the resonance frequencies of the resonators.

6.4 Other samples

Out of the samples presented in chapter (4), only two have been fully characterised in terms of ICTA performances such as the gain, noise, bandwidth and dynamic range. In this section, we present briefly the results obtained for the other samples.

- **Reflection amplifier with two separated modes** (S_{1b})

  The goal of this sample is to measure the amplification response for both signal and idler modes as well as the standard parametric amplification model. In figure (6.17), we show the power spectral density as a function of the frequency f and the voltage bias v_J. This sample is designed in order to have the signal mode at 5 GHz and the idler mode at 7 GHz. As we explained before, the resonance frequencies of our modes

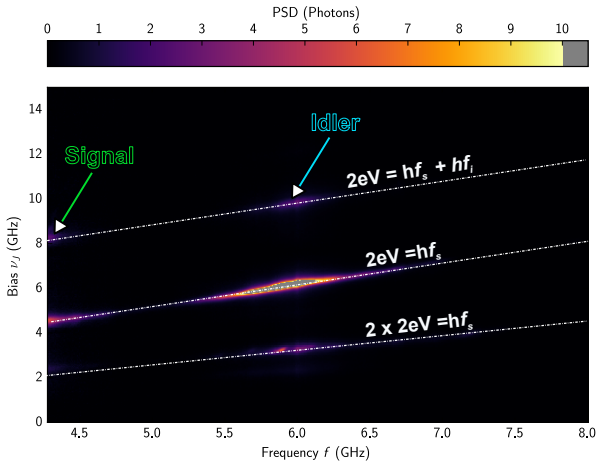

Figure 6.17 **The power spectral density for S_{1b}:** The power spectral density as function of the voltage bias v_J and the frequency f for the reflection amplifier with two separated modes. The signal mode is shifted to less than 4 GHz and the idler mode to 6 GHz.

are shifted by more than 1 GHz. Then, as shown in figure (6.17), the idler mode is shifted to 6 GHz and the signal mode to less than 4 GHz, outside from our setup range. Consequently, it was not possible to measure the amplification for the both modes.

- **Large bandwidth amplifier (S_{3a})**

  In figure (6.18.a), we plot the power spectral density as a function of the voltage bias over 4-8 GHz for this device. Three peaks are present in this plot: The first one corresponds to the tunneling of two Cooper pair jointly, with the emission of one photon ($2x2eV = hf$). The second one corresponds to one Cooper pair tunneling with the emission of one photon ($2e$V =hf). The third one corresponds to one Cooper pair tunneling with the emission of two photon at different frequencies $2eV = h(f_1 + f_2)$: One at the first resonance frequency of the impedance seen by the junction and the other one in the second mode. If the voltage bias is increased, we can also see higher order processes are also seen, as presented in figure (6.18.b). The two photon process at the same frequency is absent. This is because the real part of the impedance Re Z(f) is small around f_0 and the Josephson energy not high enough. We can't measure, therefore, the amplification for this process. However, the maximum measured gain of the single photon process is 10 dB, as shown in figure (6.18.c). In order to measure a higher gain, the Josephson energy needs to be increased by a factor of 5.

- **Transmission amplifier**

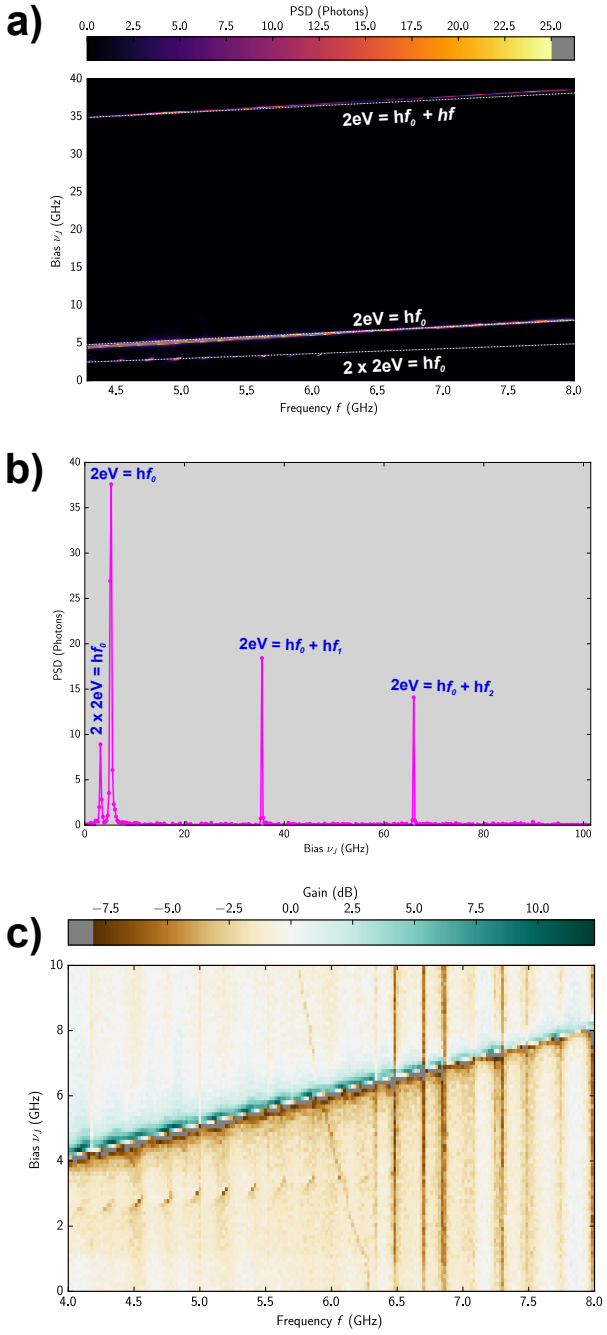

Figure 6.18 **Gain measurement for S_{3b}: a)** The power spectral density as a function of the voltage bias ν_J and the frequency f at a high Josephson energy. **b)** Cut of **a)** at frequency $f = 4.5$ GHz shows the higher order processes for high ν_J. **c)** The gain as a function of the voltage bias ν_J and the frequency f at a high Josephson energy.

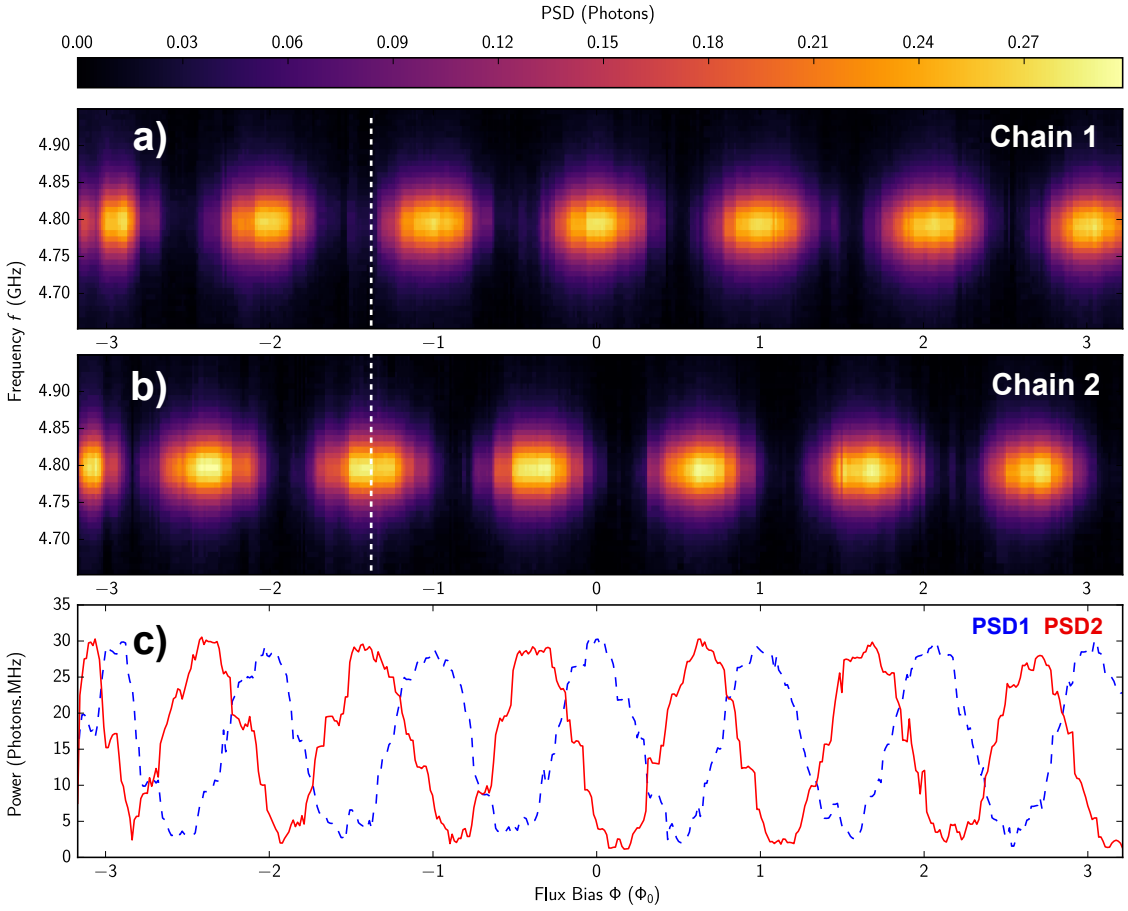

Figure 6.19 **Transmission amplifier: a,b)** The power spectral density as a function of the voltage bias v_J and the frequency f at high Josephson energy, measured on chain 1 and chain 1. **c)** Power as function of the voltage bias, measured on chain 1 and chain 2.

The advantage of the transmission amplifier is that a circulator isn't needed in order to separate the output signal and the input signal. This sample is connected from both terminals to our two chains 1 and 2, as shown in figure (2.3). We then measured the power spectral density in both chains as a function of the frequency f and the voltage bias for the one photon process in both chains. Our results are presented in figure (6.19a) and figure (6.19b). The same data integrated over frequency is shown in figure (6.19c). It's quite clear that the PSD1 is close to be in opposition of phase with PSD2. This is a strong evidence for the directionality of the amplifier. However, the Josephson energy of this device turned out anomalously small, so that the could not be observed.

Final comments

In this chapter, we have presented our experimental results for two reflection amplifiers. Compared with the results obtained from the first generation of ICTA (see chapter (3)), improvement of gain, by increasing the Josephson junction energy as well as noise, by reducing the voltage noise, have been demonstrated. For the first sample, we measured 20 dB of gain with 2.5 photons of noise. For the second sample, we measured 9 dB of gain with 0.4 photons of noise. Based on the experience gained here we expect that the good gain and noise performance can be combined in a new device which an onchip-capacitor acting as a short circuit at the operating frequency is added in order to well filter the voltage fluctuations and increase the SQUID current density in order to increase the gain. In the last section, we showed the first experimental results for the transmission amplifier. This sample exhibit a directional behavior but it was impossible to measure the amplification due to a very low critical current of the SQUID.

Conclusion & Outlooks

This thesis summarizes my work on developing and operating a phase-preserving, quantum limited amplifier based on a voltage biased Josephson junction. Our approach for amplification is based on the stimulated microwave photon emission that accompanies inelastic Cooper pair tunneling in a DC-biased Josephson junction. We call this device Inelastic Cooper pair Tunneling Amplifier (**ICTA**).

The necessary theory to understand the working principle of the ICTA and its behaviour has been developed. Two theoretical descriptions are discussed in this work, the first one is the quantum analogue to the theory of parametric amplifiers. The second one is a semi-classical theory based on P(E)-theory. These theories allow us to derive the different aspects of ICTA performance. We have shown that the ICTA gain increases with the Josephson energy. This is a great advantage over existing Josephson parametric amplifiers.

We have verified this theory has by measuring a sample based on aluminium junctions with an impedance very close to the canonical theoretical model. Here we obtained the first experimental proof that amplification close to the quantum limit is possible in this extremely simple DC-powered scheme. The measured gain for this device is around 10 dB over 280 MHz and the input added noise is approximately 0.9 photons. We have also discussed the limitations imposed on this amplifier such as the parametric oscillation and the voltage noise. We have obtained good qualitative agreement between the obtained data and the theory presented before [32].

Based on these experimental and the theoretical results a second generation of the ICTA with samples based on niobium nitride junctions has been implemented. By designing an appropriate linear matching circuit, characterized by its impedance as seen by the Josephson junction, two types of amplifiers are implemented: reflection and transmission amplifiers. For the reflection amplifier, several designs in order to optimize the ICTA bandwidth and noise, we have proposed, resulting in patent application [33].

In order to fabricate these devices, a nano/micro-fabrication process for vertical NbN/MgO/NbN Josephson junctions using a self-aligned spacer technique has been developed. We fabricated small as well as large Josephson junctions test with large gap voltage ($\cong$ 5 mV), distributed across the wafer. These junctions play an important role in the selection of the working samples and gave us a good idea of the quality of NbN/MgO /NbN films. These films show a

superconducting transition temperature of 15 K.

Finally, we have shown our experimental results obtained from the second generation of samples with focus on two of them. With the first sample we have proven that, only by increasing the Josephson energy, the ICTA gain can exceed 20 dB. In return, the measured noise is also increasing to 2.5 photons. However, for the second sample we measured 10 dB of gain and 0.4 photons of input added noise. We have shown that this measured noise corresponds to the quantum limit calculated from Caves' theorem. In the latter case, we have measured a lower noise because we have succeeded to decrease the voltage fluctuation, thanks to an on-chip-capacitor acting as a short circuit at the operation frequency and the large bandwidth of the signal resonator. We have also briefly discussed first results on other samples such as the transmision amplifier for which we have shown that the direction of noise emission can be tuned via the applied magnetic flux.

Continuation of the ICTA project

In this thesis, we have proposed several devices that were not tested yet. We have proposed in chapter (4) of this thesis a new design in which we fix the idler mode at a high frequency f_i = 290 GHz in order to reduce the thermal noise. We expect such a device to reach near quantum limited noise for signals in the GHz range even at 4K. Another sample discussed in this thesis is the transmission amplifier. This device has shown a directional behaviour but as explained before, we could not measure the gain of this amplifier because of the small critical current of the SQUID. In order to make an ICTA useful, we have to increase the current density of the junctions in order to increase the gain. For reflection amplifiers presented in this work, we have focussed on the improvement of the gain and the noise as well as the dynamic range but it was very hard to estimate the bandwidth of our amplifier because the issue of the frequency shift. It will be interesting to measure these samples when our fabrication process will be more stable. Once these issues will be solved, we expect the ICTA to become a versatile and simple quantum limited amplifier with many applications.

Application for the ICTA

In our group three main projects based on the inelastic Cooper pair tunneling physics are running:

- **Single photon source:** The goal of this project is to control the statistics of photons emitted by inelastic Cooper pair tunneling through a voltage biased Josephson junction [83–85].

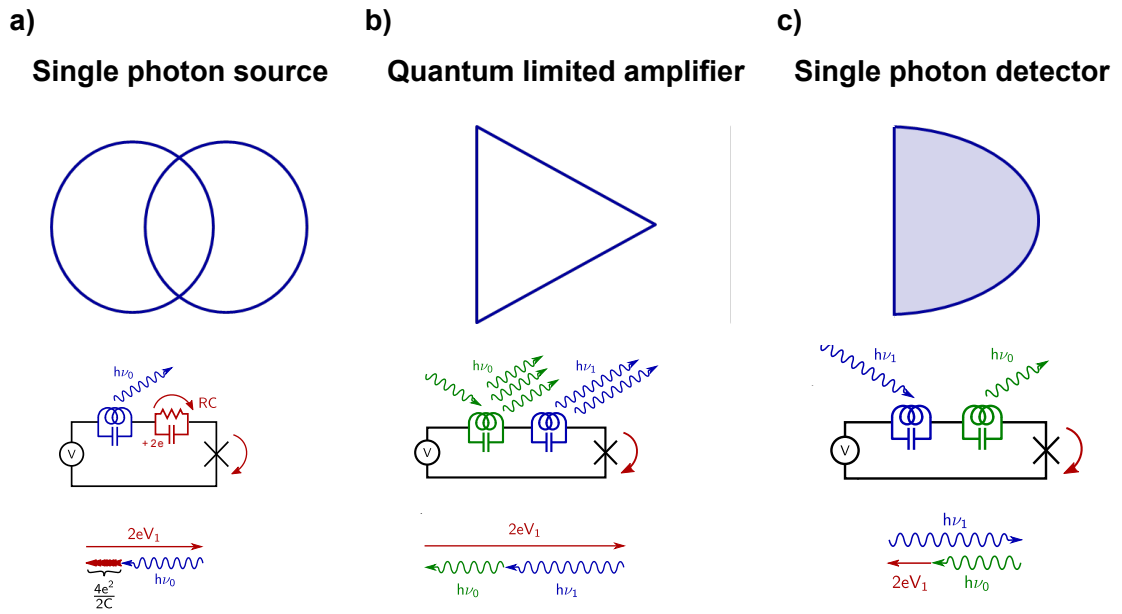

Figure 6.20 **Application for ICTA: a)** Single photon source scheme. **b)** The ICTA scheme. **c)** Single photon detector scheme.

- **Quantum limited amplifier:** The work presented in this thesis, [32] and patent application [33].
- **Single photon detector:** The idea is to use inelastic Cooper-pair tunneling across a voltage-biased Josephson junction to convert an incoming single microwave photon into an outgoing n-photon state in a different mode. The process is similar to the conversion process we have observed but at on higher order [60].

The ICTA can be used in order to accelerate the correlation function measurement between microwave photons which take usually a long time (Single photon source project). The ICTA is also necessary as post-amplification stage for the single photon detector.
It should also be noted that, such an amplifier, powered by a simple DC voltage makes it possible to deploy many amplifiers, in particular our transmission amplifier, on a chip. It could therefore be an important ingredient for qubit readout in large-scale quantum processors. We therefore hope then that some of the work in this thesis can contribute to this and other research efforts in the future.

Bibliography

[1] A. A. Houck, J. Koch, M. H. Devoret, S. M. Girvin, and R. J. Schoelkopf, "Life after charge noise: Recent results with transmon qubits," Quantum Information Processing **8**, 105 (2009).

[2] J. Koch, T. M. Yu, J. Gambetta, A. A. Houck, D. I. Schuster, J. Majer, A. Blais, M. H. Devoret, S. M. Girvin, and R. J. Schoelkopf, "Charge-insensitive qubit design derived from the Cooper pair box," Physical Review A **76** (2007), 10.1103/PhysRevA.76.042319.

[3] C. Monroe and J. Kim, "Scaling the ion trap quantum processor," Science **339**, 1164 (2013).

[4] Y. Nakamura, Y. A. Pashkin, and J. S. Tsai, "Coherent control of macroscopic quantum states in a single-Cooper-pair box," Nature **398**, 786 (1999).

[5] A. D. O'Connell, M. Hofheinz, M. Ansmann, R. C. Bialczak, M. Lenander, E. Lucero, M. Neeley, D. Sank, H. Wang, M. Weides, J. Wenner, J. M. Martinis, and A. N. Cleland, "Quantum ground state and single-phonon control of a mechanical resonator," Nature **464**, 697 (2010).

[6] I. Chiorescu, P. Bertet, K. Semba, Y. Nakamura, C. J. P. M. Harmans, and J. E. Mooij, "Coherent dynamics of a flux qubit coupled to a harmonic oscillator," Nature **431**, 159 (2004).

[7] I. Chiorescu, P. Bertet, K. Semba, Y. Nakamura, C. J. P. M. Harmans, and J. E. Mooij, "Coherent dynamics of a flux qubit coupled to a harmonic oscillator," Nature **431**, 159 (2004).

[8] C. A. Regal and K. W. Lehnert, "From cavity electromechanics to cavity optomechanics," Journal of Physics: Conference Series **264**, 012025 (2011).

[9] H. A. Haus and J. A. Mullen, "Quantum noise in linear amplifiers," Physical Review **128**, 2407 (1962).

[10] C. M. Caves, "Quantum l7imits on noise in linear amplifiers," Physical Review D **26**, 1817 (1982).

[11] B. Yurke, M. L. Roukes, R. Movshovich, and A. N. Pargellis, "A low-noise series-array Josephson junction parametric amplifier," Applied Physics Letters **69**, 3078 (1996).

[12] B. Abdo, A. Kamal, and M. Devoret, "Nondegenerate three-wave mixing with the Josephson ring modulator," Physical Review B **87** (014508 2013), 10.1103/PhysRevB.87.014508.

[13] N. Bergeal, R. Vijay, V. E. Manucharyan, I. Siddiqi, R. J. Schoelkopf, S. M. Girvin, and M. H. Devoret, "Analog information processing at the quantum limit with a Josephson ring modulator," Nature Physics **6**, 296 (2010).

[14] R. Vijay, M. H. Devoret, and I. Siddiqi, "Invited review article: The Josephson bifurcation amplifier," Review of Scientific Instruments **80**, 111101 (2009).

[15] C. Macklin, K. O'Brien, D. Hover, M. E. Schwartz, V. Bolkhovsky, X. Zhang, W. D. Oliver, and I. Siddiqi, "A near–quantum-limited Josephson traveling-wave parametric amplifier," Science **350**, 307 (2015).

[16] G. J. Ribeill, D. Hover, Y.-F. Chen, S. Zhu, and R. McDermott, "Superconducting low-inductance undulatory galvanometer microwave amplifier: Theory," Journal of Applied Physics **110**, 103901 (2011).

[17] D. Hover, Y.-F. Chen, G. J. Ribeill, S. Zhu, S. Sendelbach, and R. McDermott, "Superconducting low-inductance undulatory galvanometer microwave amplifier," Applied Physics Letters **100**, 063503 (2012).

[18] P. Lähteenmäki, V. Vesterinen, J. Hassel, H. Seppä, and P. Hakonen, "Josephson junction microwave amplifier in self-organized noise compression mode," Scientific Reports **2** (276 2012), 10.1038/srep00276.

[19] L. DiCarlo, J. M. Chow, J. M. Gambetta, L. S. Bishop, B. R. Johnson, D. I. Schuster, J. Majer, A. Blais, L. Frunzio, S. M. Girvin, and R. J. Schoelkopf, "Demonstration of two-qubit algorithms with a superconducting quantum processor," Nature **460**, 240 (2009).

[20] I. Siddiqi, "Superconducting qubits: Poised for computing?" Superconductor Science and Technology **24**, 091002 (2011).

[21] R. P. Feynman, "Simulating physics with computers," International Journal of Theoretical Physics **21**, 467 (1982).

[22] S. J. Asztalos, G. Carosi, C. Hagmann, D. Kinion, K. van Bibber, M. Hotz, L. J. Rosenberg, G. Rybka, J. Hoskins, J. Hwang, P. Sikivie, D. B. Tanner, R. Bradley, and J. Clarke, "SQUID-Based Microwave Cavity Search for Dark-Matter Axions," Physical Review Letters **104** (2010), 10.1103/PhysRevLett.104.041301.

[23] J. J. Tiemann, "Shot noise in tunnel diode amplifiers," Proceedings of the IRE **48**, 1418 (1960).

[24] C. A. Neugebauer and M. B. Webb, "Electrical conduction mechanism in ultrathin, evaporated metal films," Journal of Applied Physics **33**, 74 (1962).

[25] P. Delsing, K. K. Likharev, L. S. Kuzmin, and T. Claeson, "Effect of high-frequency electrodynamic environment on the single-electron tunneling in ultrasmall junctions," Physical Review Letters **63**, 1180 (1989).

[26] G.-L. Ingold and H. Grabert, "Finite-temperature current-voltage characteristics of ultrasmall tunnel junctions," (Europhysics Letter) **14**, 371 (1991).

[27] D. V. Averin, Y. V. Nazarov, and A. A. Odintsov, "Incoherent tunneling of the Cooper pairs and magnetic flux quanta in ultrasmall Josephson junctions," Physica B: Condensed Matter **165**, 945 (1990).

[28] S. M. Girvin, L. I. Glazman, M. Jonson, D. R. Penn, and M. D. Stiles, "Quantum fluctuations and the single-junction Coulomb blockade," Physical Review Letters **64**, 3183 (1990).

[29] Y. NAZAROV, "Gert-Ludwig Ingold (Book)," Single Charge Tunneling: Coulomb Blockade Phenomena in Nanostructures **294**, 21 (1992).

[30] T. Holst, D. Esteve, C. Urbina, and M. H. Devoret, "Effect of a transmission line resonator on a small capacitance tunnel junction," Physical Review Letters **73**, 3455 (1994).

[31] M. Hofheinz, F. Portier, Q. Baudouin, P. Joyez, D. Vion, P. Bertet, P. Roche, and D. Esteve, "Bright Side of the Coulomb Blockade," Physical Review Letters **106** (217005 2011), 10.1103/PhysRevLett.106.217005.

[32] S. Jebari, F. Blanchet, A. Grimm, D. Hazra, R. Albert, P. Joyez, D. Vion, D. Esteve, F. Portier, and M. Hofheinz, "Quantum limited amplification from inelastic Cooper pair tunneling," arXiv preprint arXiv:1704.04432 (2017).

[33] S. Jebari and M. Hofheinz, "Circuit d'adaptation pour amplificateur bas bruit et amplificateur bas bruit comprenant un tel circuit," patent application (2016).

[34] A. Blais, R.-S. Huang, A. Wallraff, S. M. Girvin, and R. J. Schoelkopf, "Cavity quantum electrodynamics for superconducting electrical circuits: An architecture for quantum computation," Physical Review A **69** (69.062320 2004), 10.1103/PhysRevA.69.062320.

[35] I. Chiorescu, P. Bertet, K. Semba, Y. Nakamura, C. J. P. M. Harmans, and J. E. Mooij, "Coherent dynamics of a flux qubit coupled to a harmonic oscillator," Nature **431**, 159 (2004).

[36] H. Paik, D. I. Schuster, L. S. Bishop, G. Kirchmair, G. Catelani, A. P. Sears, B. R. Johnson, M. J. Reagor, L. Frunzio, L. I. Glazman, S. M. Girvin, M. H. Devoret, and R. J. Schoelkopf, "Observation of high coherence in Josephson junction qubits measured in a three-dimensional circuit QED architecture," Physical Review Letters **107** (240501 2011), 10.1103/PhysRevLett.107.240501.

[37] N. Bergeal, F. Schackert, M. Metcalfe, R. Vijay, V. E. Manucharyan, L. Frunzio, D. E. Prober, R. J. Schoelkopf, S. M. Girvin, and M. H. Devoret, "Phase-preserving amplification near the quantum limit with a Josephson ring modulator," Nature **465**, 64 (2010).

[38] B. Ho Eom, P. K. Day, H. G. LeDuc, and J. Zmuidzinas, "A wideband, low-noise superconducting amplifier with high dynamic range," Nature Physics **8**, 623 (2012).

[39] K. W. Murch, S. J. Weber, C. Macklin, and I. Siddiqi, "Observing single quantum trajectories of a superconducting quantum bit," Nature **502**, 211 (2013).

[40] F. D. O. Schackert, *A Practical quantum-limited parametric amplifier based on the Josephson ring modulator* (Yale University, 2013).

[41] P. Campagne-Ibarcq, *Measurement Back Action and Feedback in Superconducting Circuits*, Ph.D. thesis, Ecole Normale Supérieure (ENS) (2015).

[42] S.-K. Choi, R.-D. Li, C. Kim, and P. Kumar, "Traveling-wave optical parametric amplifier: Investigation of its phase-sensitive and phase-insensitive gain response," Journal of the Optical Society of America B **14**, 1564 (1997).

[43] J. Kakande, C. Lundström, P. A. Andrekson, Z. Tong, M. Karlsson, P. Petropoulos, F. Parmigiani, and D. J. Richardson, "Detailed characterization of a fiber-optic parametric amplifier in phase-sensitive and phase-insensitive operation," Optics Express **18**, 4130 (2010).

[44] S. Longhi, "Time-reversed optical parametric Oscillation," Physical Review Letters **107** (2011), 10.1103/PhysRevLett.107.033901.

[45] B. Huard, *Quantum Information with Superconducting Circuits*, Ph.D. thesis, Ecole Normale Supérieure de Paris-ENS Paris (2014).

[46] R. Movshovich, B. Yurke, P. G. Kaminsky, A. D. Smith, A. H. Silver, R. W. Simon, and M. V. Schneider, "Observation of zero-point noise squeezing via a Josephson-parametric amplifier," Physical Review Letters **65**, 1419 (1990).

[47] R. Slusher, L. W. Hollberg, B. Yurke, J. C. Mertz, and J. F. Valley, "Observation of squeezed states generated by four-wave mixing in an optical cavity," Physical Review Letters **55**, 2409 (1985).

[48] B. Yurke, P. G. Kaminsky, R. E. Miller, E. A. Whittaker, A. D. Smith, A. H. Silver, and R. W. Simon, "Observation of 4.2-K equilibrium-noise squeezing via a Josephson-parametric amplifier," Physical Review Letters **60**, 764 (1988).

[49] B. Yurke, M. L. Roukes, R. Movshovich, and A. N. Pargellis, "A low-noise series-array Josephson junction parametric amplifier," Applied physics letters **69**, 3078 (1996).

[50] B. Abdo, K. Sliwa, L. Frunzio, and M. Devoret, "Directional Amplification with a Josephson Circuit," Physical Review X **3** (2013), 10.1103/PhysRevX.3.031001.

[51] K. Sliwa, M. Hatridge, A. Narla, S. Shankar, L. Frunzio, R. Schoelkopf, and M. Devoret, "Reconfigurable Josephson circulator/directional amplifier," Physical Review X **5** (5.041020 2015), 10.1103/PhysRevX.5.041020.

[52] X. Zhou, V. Schmitt, P. Bertet, D. Vion, W. Wustmann, V. Shumeiko, and D. Esteve, "High-gain weakly nonlinear flux-modulated Josephson parametric amplifier using a SQUID array," Physical Review B **89** (2014), 10.1103/PhysRevB.89.214517.

[53] K. O'Brien, C. Macklin, I. Siddiqi, and X. Zhang, "Resonant Phase Matching of Josephson junction traveling wave parametric amplifiers," Physical Review Letters **113** (157001 2014), 10.1103/PhysRevLett.113.157001.

[54] A. Ergül, *Fabrication and Characterization of Superconductive Coplanar Waveguide Resonators* (Skolan för teknikvetenskap, Kungliga Tekniska högskolan, 2009).

[55] H. Seppa, M. Kiviranta, and L. Gronberg, "Dc SQUID based on unshunted Josephson junctions: Experimental results," IEEE Transactions on Applied Superconductivity **5**, 3248 (1995).

[56] N. Bergeal, F. Schackert, L. Frunzio, and M. H. Devoret, "Two-mode correlation of microwave quantum noise generated by parametric down-conversion," Physical Review Letters **108**, 123902 (2012).

[57] M. A. Castellanos-Beltran, K. D. Irwin, G. C. Hilton, L. R. Vale, and K. W. Lehnert, "Amplification and squeezing of quantum noise with a tunable Josephson metamaterial," Nature Physics **4**, 929 (2008).

[58] M. A. Castellanos-Beltran and K. W. Lehnert, "Widely tunable parametric amplifier based on a superconducting quantum interference device array resonator," Applied Physics Letters **91**, 083509 (2007).

[59] H. Zimmer, "Parametric amplification of microwaves in superconducting Josephson tunnel junctions," Applied Physics Letters **10**, 193 (1967).

[60] J. Leppäkangas, M. Marthaler, D. Hazra, S. Jebari, G. Johansson, and M. Hofheinz, "Multiplying microwave photons by inelastic Cooper-pair tunneling," arXiv preprint arXiv:1612.07098 (2016).

[61] I. Safi, "Time-dependent Transport in arbitrary extended driven tunnel junctions," arXiv preprint arXiv:1401.5950 (2014).

[62] P. J. Safi, D. Vion, P. Roche, D. Esteve, and F. Portier, "Fluctuation-dissipation relations of a tunnel junction driven by a quantum circuit," .

[63] P.-M. Billangeon, F. Pierre, H. Bouchiat, and R. Deblock, "Emission and Absorption Asymmetry in the Quantum Noise of a Josephson Junction," Physical Review Letters **96** (2006), 10.1103/PhysRevLett.96.136804.

[64] P. K. Tien and J. P. Gordon, "Multiphoton process observed in the interaction of microwave fields with the tunneling between superconductor films," Physical Review **129**, 647 (1963).

[65] G. B. Lesovik and L. S. Levitov, "Noise in an ac biased junction: Nonstationary Aharonov-Bohm effect," Physical Review Letters **72**, 538 (1994).

[66] N. Bergeal, F. Schackert, L. Frunzio, D. E. Prober, and M. H. Devoret, "Mesoscopic resistor as a self-calibrating quantum noise source," Applied Physics Letters **100**, 203507 (2012).

[67] P. Lähteenmäki, V. Vesterinen, J. Hassel, H. Seppä, and P. Hakonen, "Josephson junction microwave amplifier in self-organized noise compression mode," Scientific Reports **2** (2012), 10.1038/srep00276.

[68] R. Vijay, M. H. Devoret, and I. Siddiqi, "Invited Review Article: The Josephson bifurcation amplifier," Review of Scientific Instruments **80**, 111101 (2009).

[69] J. Gao, "The physics of superconducting microwave resonators"." (2008).

[70] D. Pozar, "Microwave engineering, 4th edition," (2011).

[71] P. Lähteenmäki, V. Vesterinen, J. Hassel, G. S. Paraoanu, H. Seppä, and P. Hakonen, "Advanced concepts in Josephson junction reflection amplifiers," Journal of Low Temperature Physics **175**, 868 (2014).

[72] Y. Levinson, "Quantum noise in a current-biased Josephson junction," Physical Review B **67** (2003), 10.1103/PhysRevB.67.184504.

[73] T. Roy, S. Kundu, M. Chand, A. M. Vadiraj, A. Ranadive, N. Nehra, M. P. Patankar, J. Aumentado, A. A. Clerk, and R. Vijay, "Broadband parametric amplification with impedance engineering: Beyond the gain-bandwidth product," Applied Physics Letters **107**, 262601 (2015).

[74] F. Lecocq, C. Naud, I. M. Pop, Z.-H. Peng, I. Matei, T. Crozes, T. Fournier, W. Guichard, and O. Buisson, "Novel E-beam lithography technique for in-situ junction fabrication: The controlled undercut," arXiv preprint arXiv:1101.4576 (2011).

[75] G. J. Dolan, "Offset masks for lift-off photoprocessing," Applied Physics Letters **31**, 337 (1977).

[76] T. Yamashita, S. Kitahara, Y. Onodera, Y. Goto, and T. Aso, "Upper critical field of superconducting NbN films," Journal of Applied Physics **43**, 4749 (1972).

[77] A. Shoji, F. Shinoki, S. Kosaka, M. Aoyagi, and H. Hayakawa, "New fabrication process for Josephson tunnel junctions with (niobium nitride, niobium) double-layered electrodes," Applied Physics Letters **41**, 1097 (1982).

[78] D. Hazra, N. Tsavdaris, S. Jebari, A. Grimm, F. Blanchet, F. Mercier, E. Blanquet, C. Chapelier, and M. Hofheinz, "Superconducting properties of very high quality NbN thin films grown by high temperature chemical vapor deposition," Superconductor Science and Technology **29**, 105011 (2016).

[79] T. Van Duzer, "Principles of superconductive devices and circuits," (1978).

[80] M. Tinkham, "Introduction to superconductivity, 2nd edition. Dover Books on Physics. Dover Publications," (2004).

[81] A. Kawakami, Z. Wang, and S. Miki, "Fabrication and characterization of epitaxial NbN/MgO/NbN Josephson tunnel junctions," Journal of Applied Physics **90**, 4796 (2001).

[82] A. Shoji, M. Aoyagi, S. Kosaka, F. Shinoki, and H. Hayakawa, "Niobium nitride Josephson tunnel junctions with magnesium oxide barriers," Applied Physics Letters **46**, 1098 (1985).

[83] J. Leppäkangas, M. Fogelström, A. Grimm, M. Hofheinz, M. Marthaler, and G. Johansson, "Antibunched Photons from Inelastic Cooper-Pair Tunneling," Physical Review Letters **115** (2015), 10.1103/PhysRevLett.115.027004.

[84] R. Albert, "Time resolved correlation of microwave photons produced by inelastic tunneling of Copper pairs (master's thesis)," (2016).

[85] M. Wouters and V. Savona, "Stochastic classical field model for polariton condensates," Physical Review B **79**, 165302 (2009).